UNIVERSIDADE D
COIMBRA

Slava Luzmila Lola Bourgeois

Development of Mathematical Morphology and Pattern Recognition Algorithms to Characterize Solar Activity

Tese no âmbito do doutoramento em Física ramo de Astrofísica, orientada pelo Professor Doutor Orlando Olavo Aragão Aleixo e Neves de Oliveira, Doutora Maria Teresa de Abrunhosa Barata e Professor Doutor Robertus von Fay-Siebenburgen, e apresentada ao Departamento de Física da Faculdade da Faculdade de Ciências e Tecnologia da Universidade de Coimbra.

Fevereiro de 2025

Development of Mathematical Morphology and Pattern Recognition Algorithms to Characterize Solar Activity

Slava Luzmila Lola Bourgeois

Submitted for the degree of Doctor of Philosophy in Mathematics branch Applied Mathematics

School of Mathematical and Physical Sciences

February 2025

Supervisors: Dr. Maria Teresa de Abrunhosa Barata, Prof. Orlando Olavo Aragão Aleixo e Neves de Oliveira, and Prof. Robertus von Fay-Siebenburgen

University of Sheffield

Abstract

Solar activity acts as the primary driver of space weather, encompassing phenomena such as flares, coronal mass ejections, and solar energetic particles, which originate from distinct regions like sunspots, faculae, and granules. Predicting space weather is essential due to its significant impact on planetary atmospheres and human activities both in space and on Earth, including communication and navigation systems, power grids, spacecraft operations, astronaut safety, and aviation at high altitudes and latitudes. Sunspots, in particular, harbour intense magnetic fields that can trigger powerful solar eruptions and therefore require continuous monitoring. In recent years, automated identification methods have become increasingly common as the vast amounts of data from both ground- and space-based observatories can no longer be handled manually.

In this thesis, we developed mathematical morphology algorithms for automatic sunspot detection. Our results, compared with those obtained through manual methods, demonstrate comparable accuracy, enabling the extension of this approach to other solar features and image datasets. For instance, we applied a modified version of these algorithms to simulation-generated maps to identify magnetic flux rope structures in two active regions, capturing their distinct dynamics and, in one case, an eruption corroborated by Solar Dynamics Observatory (SDO) observations.

Mathematical morphology was further applied to extensive datasets to identify all coronal off-limb structures visible in SDO/Atmospheric Imaging Assembly (AIA) 304 Å images throughout nearly the entire Solar Cycle 24 (June 2010–December 2021). Statistical analysis of the properties of these features revealed significant trends, including distinct behaviours between high- and low-intensity coronal structures in terms of latitudinal distribution. Additionally, evidence was found for the existence of active longitudes, with

coronal off-limb structures exhibiting a preferred longitudinal distribution pattern. These findings deepen our understanding of coronal activity and open new avenues for improving space weather forecasting.

Keywords: Sun; Solar activity; Mathematical morphology; Sunspots; Coronal off-limb structures; Magnetic flux ropes; Active longitudes

Resumo

A atividade solar, manifesta-se de variadas formas – manchas solares, fáculas, fulgurações, ejeções de massa coronal, dinâmicas do vento solar e mais – sendo o principal condutor dos fenómenos da meteorologia espacial. Prever a meteorologia espacial é essencial devido ao seu significativo impacto nas atmosferas planetárias e nas atividades humanas e económicas tanto no espaço quanto na Terra. Tal inclui sistemas de comunicação e navegação, satélites, aviação, redes elétricas, entre outros. As manchas solares, em particular, abrigam campos magnéticos intensos que podem desencadear erupções solares poderosas, sendo necessário monitorizá-las continuamente. Nos últimos anos, a enorme quantidade de dados provenientes de observatórios terrestres e espaciais dificulta a sua manipulação visualmente, pelo que os métodos automáticos de identificação tornaram-se ferramentas cruciais para processar esta valiosa informação.

Nesta tese, foram desenvolvidos algoritmos de morfologia matemática para a deteção automática de manchas solares. Comparámos os resultados obtidos com resultados obtidos por métodos manuais tendo sido encontrada uma precisão comparável, que permitiu extrapolar esta abordagem a outras características solares. Por exemplo, foi aplicada uma versão alterada desses algoritmos a mapas criados por simulação para identificar estruturas de cordas de fluxo magnético em duas regiões ativas. Esta abordagem permitiu capturar dinâmicas distintas e, num caso de estudo, identificar uma erupção que também foi visível nas observações do SDO.

A morfologia matemática encontra aplicações a conjuntos de dados mais vastos. Assim, esta teoria foi utilizada para identificar todas as estruturas coronais visíveis em imagens SDO/AIA 304 Å ao longo de quase todo o Ciclo Solar 24, desde junho de 2010 a dezembro de 2021. Realizou-se uma análise estatística das propriedades dessas características, como sendo área, intensidade e distribuição espacial. Este estudo revelou tendências interessantes, tais como

comportamentos distintos entre estruturas coronais de alta e baixa intensidade, relativamente à sua distribuição latitudinal, bem como evidências da existência de longitudes ativas, sugerindo um padrão preferencial na distribuição longitudinal das estruturas coronais.

Palavras-chave: Sol; Atividade solar; Morfologia matemática; Manchas solares; Estruturas coronais; Cordas de fluxo magnético; Longitudes ativas

Acknowledgements

I extend my heartfelt gratitude to everyone who has supported and guided me throughout my PhD journey.

First and foremost, I am grateful to my supervisors for their guidance and mentorship. Thank you, Ricardo, for your motivation and support throughout every stage of my PhD, especially during the challenging early days.

Jean, thank you for your initial guidance, continuous support, remarkable kindness, and for introducing me to the world of research and the beauty of auroras.

To my family, thank you for your steadfast emotional support and unwavering encouragement. Your presence has been a constant source of strength, particularly during moments of doubt and difficulty.

To my friends, thank you for your boundless motivation, uplifting words, and shared laughter, which brought so much joy to this journey. Mathias, your understanding of the unique challenges of PhD life and your unwavering support made this path significantly easier. Your help has been truly invaluable. Louise, thank you for our long and meaningful conversations about life.

To Suzanne, Robin, and Guilliam, whom I first met during my master's thesis — thank you for your inspiration and encouragement along the way. Suzanne and Robin, your visits to Portugal and the U.K. were magical and reignited my enthusiasm at pivotal moments.

Natacha, I am profoundly thankful for your exceptional kindness and support. You introduced me to the wonders of Portugal in such unique ways, helping me feel at home in this beautiful country. Thank you, Joana, for our runs along the Mondego and in the magical Choupal.

Shifana, I am grateful for the enriching experience we shared during our industrial training at IPN — a time that was both memorable and rewarding. Thank you, Joana, for welcoming us so warmly and for introducing us to the

startup incubator, giving us insight into a whole new world.

Andreas, I owe special thanks to you for your mentorship during our observational training in Hungary. Your organisational skills and coding expertise were truly inspiring and foundational to this thesis. Without your initial guidance, ideas, and encouragement, this work might not have been possible.

I am deeply appreciative of my collaborators — Andreas, Simone, Szabolcs, Marianna, and Jiajia — for their invaluable contributions and dedication to our research projects. Simone, your good humour and productivity made our collaboration a true pleasure. Szabolcs, thank you for your help with both the project and at the Gyula Observatory. Marianna, Robertus, and Balazs, I am grateful for the fantastic experience at the Gyula Observatory.

I also extend my gratitude to all my SWATNet peers and collaborators for fostering such a supportive and collaborative environment. Thank you, Lidiya, for the shared moments we enjoyed together in various countries during our PhDs.

Special thanks also go to Luigi and Edoardo for the memorable and unique moments we shared during the first year, to Sho and Amy for our motivational evenings, and to Matthew for his incredible support and inspirational mindset.

Finally, I am grateful to all the students and staff I met along the way, whether at the Universities of Coimbra and Sheffield, in the office, or at the Observatory of Coimbra. Your contributions, friendship, and encouragement have enriched this journey in countless ways.

Contents

List of Figures

List of Tables

List of Publications

1. S. Bourgeois, T. Barata, R. Erdélyi, R. Gafeira, and O. Oliveira, "Sunspots Identification Through Mathematical Morphology", *Sol Phys* **299**, 10, 2024, DOI: 10.1007/s11207-023-02243-1

2. S. Bourgeois, S. Chierichini, Sz. Soós, R. Erdélyi, J. Liu, M.B. Korsós, R. Gafeira, and T. Barata, "Long-term properties of coronal off-limb structures", *A&A*, 2024, DOI: 10.1051/0004-6361/202451257

3. A. Wagner, S. Bourgeois, E.K.J. Kilpua, R. Sarkar, D. J. Price, A. Kumari, J. Pomoell, S. Poedts, T. Barata, R. Erdélyi, O. Oliveira, and R. Gafeira, "The Automatic Identification and Tracking of Coronal Flux Ropes — Part II: New Mathematical Morphology-based Flux Rope Extraction Method and Deflection Analysis", *A&A*, 2024, DOI: 10.1051/0004-6361/202348113

4. A. Wagner, D. J. Price, S. Bourgeois, F. Daei, J. Pomoell, S. Poedts, A. Kumari, T. Barata, R. Erdélyi, E. K. J. Kilpua, "The effect of data-driving and relaxation model on magnetic flux rope evolution and stability", *A&A*, 2024, DOI: 10.1051/0004-6361/202450577

5. A. Wagner, D. J. Price, S. Bourgeois, J. Pomoell, S. Poedts, and E. K. J. Kilpua, "Solar magnetic flux rope identification with GUITAR: GUI for Tracking and Analysing flux Ropes", *Frontiers in Astronomy and Space Sciences*, 2024, DOI: 10.3389/fspas.2024.1383072

6. S. Chierichini, S. Bourgeois, Sz. Soós, J. Liu, M.B. Korsós, D. Del Moro, and R. Erdélyi, "Coronal jet Identification with Machine Learning", *A&A*, 2024 (submitted).

List of Acronyms

AI Artificial Intelligence

ML Machine Learning

DL Deep Learning

NNs Neural Networks

MNN Morphological Neural Network

CNN Convolutional Neural Network

GPUs Graphics Processing Units

IT Information Technology

FLARECAST Flare Likelihood and Region Eruption Forecasting

SDO Solar Dynamics Observatory

AIA Atmospheric Imaging Assembly

SW Space Weather

GNSS Global Navigation Satellite System

GICs Geomagneticallly Induced Currents

SIRs Stream Interaction Regions

CIRs Co-rotating Interaction Regions

CMEs Coronal Mass Ejections

SEPs Solar Energetic Particles

ICMEs Interplanetary Coronal Mass Ejections

NASA National Aeronautics and Space Administration

ACE Advanced Composition Explorer

UV ultraviolet

EUV extreme ultraviolet

TSI total solar irradiance

MHD magnetohydrodynamic

EUI Extreme Ultraviolet Imager

SolO Solar Orbiter

HF high-frequency

AWS Air Weather Service

TDRS Tracking and Data Relay Satellite

ADEOS Advanced Earth Observing Satellite

GPS Global Positioning System

MM Mathematical morphology

SE structuring element

OGAUC Geophysical and Astrophysical Observatory of the University of Coimbra

CAO Astrophysical Observatory of Catania

HMI Helioseismic and Magnetic Imager

SSIM Structural Similarity Index Measure

PSNR Peak Signal-to-Noise Ratio

STFT Short-Time Fourier Transform

VHR very high-resolution

CT Computed Tomography

MRI Magnetic Resonance Imaging

BBSO Big Bear Solar Observatory

EIT Extreme ultraviolet Imaging Telescope

SoHO Solar and Heliospheric Observatory

MDI Michelson Doppler Imager

GOES Geostationary Operational Environmental Satellite

DHO Debrecen Heliophysical Observatory

HMIDD HMI Debrecen sunspot Data

DPD Debrecen Photoheliographic Data

GPR Greenwich Photoheliographic Results

RGO Royal Greenwich Observatory

SDD SoHO/MDI Debrecen Data

SOON Solar Optical Observing Network

MH millionths of the solar hemisphere

EVE Extreme ultraviolet Variability Experiment

MFRs magnetic flux ropes

LASCO Large Angle and Spectrometric Coronagraph

ARs active regions

TMFM time-dependent data-driven magnetofrictional model

PIL polarity inversion line

SAJIA Semiautomated Jet Identification Algorithm

AJIA Automated Jet Identification Algorithm

CCD charge-coupled device

PA position angle

ORDA Online Research Data

SC Solar Cycle

PDF probability density function

N-S North-South

KDE kernel density estimation

E-W East-West

EC European Commission

SWATNet Space Weather Awareness Training Network

Chapter 1

Introduction

1.1 What is space weather?

Space Weather (SW) refers to the solar-driven conditions in space that affect not only Earth but also the atmospheres and magnetospheres of other planets. SW has significant impacts on various aspects of Earth, particularly through the initiation of geomagnetic storms, which cause fluctuations in Earth's magnetic field. These storms induce electric currents in the ionosphere that can propagate along power transmission lines, potentially leading to damage to power grids. SW also produces radiation storms, characterised by heightened fluxes of energetic particles, which pose risks to satellite electronics, astronauts, and passengers and crew on high-altitude and -latitude flights (Jones et al. 2005; Iucci et al. 2005; Eastwood et al. 2017; Bain et al. 2023). Additionally, SW creates ionospheric disturbances that alter electron density, thereby impacting radio wave propagation, satellite communication, and Global Navigation Satellite System (GNSS) signals, along with other satellite-based navigation systems. Satellites orbiting Earth are also affected by charging from low-energy particles, outages, orbital decay, and increased drag due to atmospheric density changes from incoming solar particles. Terrestrial conductors are impacted by electromagnetic induction from SW events, which can generate large electric currents known as Geomagneticallly Induced Currents (GICs). These GICs can cause various issues at ground level, such as the saturation of power transformers and corrosion in pipelines.

The Sun is dynamic, continuously emitting particles into interplanetary space in an ongoing flow known as the solar wind, initially inferred from

observations of comet tails (Biermann 1951; Biermann et al. 1967). Parker 1958 was the first to theoretically describe the expansion of the solar corona as the solar wind. The solar wind is generally categorised into two types: slow and fast. The slow solar wind moves along magnetic field lines extending from the Sun's equatorial regions, travelling at speeds equal to or less than 500 km/s and at relatively lower temperatures and densities compared to the fast solar wind. The fast solar wind, on the other hand, originates from open magnetic field lines in the solar corona, such as coronal holes. When it catches up with and compresses the slower solar wind, it creates regions of enhanced density and magnetic field strength known as Stream Interaction Regions (SIRs). If these SIRs persist over at least one solar cycle following the Sun's rotation, they form Co-rotating Interaction Regions (CIRs). Slow and fast solar winds, and especially SIRs and CIRs, significantly impact SW by causing recurrent high-speed streams in the solar wind that can interact with Earth's magnetosphere.

In addition to this continuous background of solar wind, the Sun also sporadically ejects transients, including solar flares, Coronal Mass Ejections (CMEs), and Solar Energetic Particles (SEPs). Predicting these stochastic events — their onset, duration, intensity, and arrival time at Earth — is crucial for effective SW monitoring, and each will be detailed in the following section.

These solar phenomena originate in different layers of the highly stratified solar atmosphere, where physical parameters such as temperature and density vary significantly over relatively short distances. The first layer is the photosphere, the visible surface of the Sun, extending approximately 600 km in height. It has a temperature of around 5000–6000 K and a high density of 10^{23} m^{-3}, which allows for direct observations of the magnetic field. Above the photosphere lies the chromosphere, extending from 600 km to around 2000 km in height. This layer has a lower density of 10^{19} m^{-3}, and temperatures increase sharply, reaching about $10,000$ K at the top. At approximately 2 Mm ($2,000$ km) in height is the transition region, where temperatures rise from $50,000$ to $100,000$ K, and the density decreases to 10^{16} m^{-3}. The outermost layer of the solar atmosphere, the corona, extends from the transition region outward into space. The corona has a very low density, compared to the photosphere, around 10^{15} m^{-3}, while temperatures soar to over $1,000,000$ K.

The coronal heating paradox, which also reflects a chromospheric heating problem, exemplifies this stratification. While the temperature in the pho-

tosphere is around 6000 K, it increases drastically and unexpectedly in the chromosphere and transition region, reaching temperatures of 1–3 million K in the corona (Aschwanden 2004; Aschwanden et al. 2007). The solar atmosphere is also highly complex and dynamic, displaying a wide variety of features that evolve over different timescales, from seconds to days or even months, each requiring different physical models for accurate description.

A key parameter used to evaluate whether plasma or magnetic field dominates in the solar atmosphere is the plasma-beta, defined as the ratio of gas to magnetic pressure. The plasma-beta is high in the lower atmosphere, such as at the photospheric level in granules, where gas pressure dominates due to higher plasma density. In contrast, in sunspots or in the solar corona, the plasma beta is very low, indicating that the magnetic field dominates. In this case, magnetic pressure confines plasma along magnetic field lines, while magnetic tension stabilises magnetic structures against disturbances, resisting bending. During eruptive events, however, these magnetic forces are overcome, leading to the release of stored energy.

1.2 Main precursors of space weather

The Sun hosts a wide range of features and phenomena that contribute to SW. This section highlights the most significant features, focusing particularly on those relevant to the different projects discussed in this PhD thesis, as detailed in Chapters 3, 4, and 5.

1.2.1 Coronal mass ejections

CMEs are massive eruptions of magnetised plasma expelled from the Sun, consisting of electrons, protons, and heavier ions, all carrying embedded complex magnetic field structures. These events can release up to $10^{15} - 10^{16}$ grams of plasma into interplanetary space, with speeds ranging from tens of km/s to over $3,000$ km/s (Green et al. 2018). Webb et al. 2012 reported an average CME speed of approximately 490 km/s. CMEs usually originate from active regions with intense, complex magnetic fields and are often associated with prominence eruptions (Subramanian et al. 2001).

The origin of CMEs is closely linked to magnetic reconnection, a phenomenon in which oppositely directed magnetic fields realign, changing the

magnetic field topology from a high-energy to a lower-energy configuration. This process rapidly releases stored magnetic energy, triggering various eruptive solar events (Priest et al. 2000; Srivastava et al. 2019). Historically, CMEs were observable only during solar eclipses, but significant advancements in CME study followed Bernard Lyot's invention of the coronagraph in 1929 (Lyot 1939; Koutchmy 1988). This instrument blocks out the bright light of the Sun's photosphere, enabling observation of the fainter corona and its dynamic phenomena. CMEs frequently exhibit a three-part structure consisting of a bright core within a dark cavity beneath a bright frontal loop (Illing et al. 1985; see Figure 4.1), though not all CMEs display such a clear flux rope expansion. The most geoeffective CMEs are halo CMEs, which propagate in all directions, including toward Earth (Howard et al. 1982).

CMEs that travel faster than the ambient solar wind can generate interplanetary shocks at their leading edges, which may trigger gradual SEP events (see Subsection 1.2.3). As they propagate through the heliosphere and interact with the background solar wind, CMEs evolve into Interplanetary Coronal Mass Ejections (ICMEs), with changes in shape, speed, and internal structure. ICMEs are detectable through in-situ measurements from spacecraft such as National Aeronautics and Space Administration (NASA)'s Advanced Composition Explorer (ACE). These structures display identifiable characteristics, including enhanced magnetic field strength and a low plasma beta indicating that the ICME plasma is tightly confined by the magnetic field.

1.2.2 Solar flares

Solar flares are sudden bursts of electromagnetic radiation spanning the entire spectrum, including gamma rays, X-rays, ultraviolet (UV) light, visible light, and radio waves, with the strongest emissions typically observed in X-ray, UV, and extreme ultraviolet (EUV) wavelengths. Flares are classified based on their peak X-ray flux into A, B, C, M, and X classes, with X-class flares being the most intense. Flares not accompanied by CMEs are termed confined flares, while those accompanied by CMEs are known as eruptive flares and can be highly geoeffective. Indeed, flares associated with CMEs are often observed to be longer-lasting or more intense (Green et al. 2002). Youssef 2012 found a strong correlation between flare flux and the energy of associated CMEs, particularly during periods of heightened solar activity. During a flare, the

released energy can accelerate particles to nearly the speed of light, contributing to impulsive SEP events (see Subsection 1.2.3).

Unlike CMEs, which can originate from both active regions and the quiet Sun, major solar flares originate exclusively in active regions (Campi et al. 2019). They result from the rapid release of stored magnetic energy, heating the surrounding plasma and unleashing up to $10^{32} - 10^{33}$ erg, as seen in the Carrington event of 1859 (see Section 1.4). The most powerful flares, known as superflares, have been observed on nearby Sun-like stars, releasing up to 1000 times more energy than the Carrington event (Schaefer 2012; Maehara et al. 2012). Maehara et al. 2017 demonstrated that the mechanisms of magnetic activity underlying superflares on solar-type stars are similar to those occurring on the Sun. According to Shibata et al. 2013, superflares with an energy of 10^{34} erg could occur on the Sun approximately once every 800 years, while those reaching 10^{35} erg might take place roughly once every 5000 years. If such superflares were to materialise on the Sun, their effects could jeopardise not only technological systems but also Earth's environment.

1.2.3 Solar energetic particles

SEPs are high-energy particles ejected by the Sun, consisting of protons, electrons, and heavier ions. Their energies span a wide range, from the order of keV to GeV, with many accelerated to near-relativistic speeds (Whitman et al. 2023). SEPs are typically categorised into two types based on their origin: impulsive and gradual SEP events (Reames 2013).

Impulsive SEP events are associated with solar flares and occur near the flare sites, where magnetic field lines reconnect (Shea et al. 1990). These events have smaller spatial extent and are characterised by a rapid onset and decay, closely coinciding with the timing of the associated flare. Impulsive SEP events are dominated by lower-energy electrons and ions, and they are relatively short-lived, lasting from a few minutes to several hours.

Gradual SEP events, by contrast, are accelerated by CME-driven shock waves (Reames 2004). These events are long-lasting, with durations ranging from several hours to days, and are distinguished by a prolonged decline due to the passage of the CME shock front. While gradual SEP events also accelerate electrons and ions, they are predominantly dominated by high-energy protons, often with energies in the MeV to GeV range. This gives rise to their nickname

"big proton events" (Reames 2021). These high-energy proton events are a primary concern for radiation hazards to astronauts, satellites, and high-altitude flights, particularly in polar regions.

1.2.4 Sunspots

The photosphere displays a granulation pattern formed by large convection cells, called granules, which are in perpetual motion. Within the narrow, dark lanes between granules lie magnetic bright points — small-scale, dynamic features of concentrated magnetic fields with strengths in the kilogauss range (Keys et al. 2020). Plasma rises through the centres of granules and descends back into the solar interior at their edges, creating a dynamic behaviour that characterises the quiet Sun.

In contrast, the Sun also hosts active regions with stronger and more complex magnetic fields, particularly in sunspots, where magnetic fields strengths can reach several thousand Gauss. Most clearly seen in the photosphere, sunspots appear as dark, Earth-sized patches in continuum images. They are cooler than their neighbouring regions due to the intense magnetic fields hampering convection, thereby lowering the local temperature. Typically, sunspots have lifetimes of several days, diameters exceeding 20 Mm, and magnetic field strengths above 2000 G. Sunspots are composed of a dark central region, the umbra, and a brighter surrounding area, the penumbra (Rempel et al. 2009). Smaller sunspots consisting only of an umbra are referred to as pores. Studying sunspots is essential, as they are primary sources of solar eruptions, such as flares and CMEs, which have substantial impacts on SW.

1.2.5 Facular regions

In active regions surrounding sunspots, large bright areas often appear in white-light images. These regions exhibit enhanced magnetic fields, although less intense than those found within sunspots, and thus they typically develop both before and after sunspot formation. The concentrated magnetic fields in faculae generate heat, causing these areas to appear brighter. In the photosphere, these bright features are referred to as faculae, while in the chromosphere, they are known as solar plages. Faculae and plages are key indicators of solar cycle activity, playing a significant role in locating active regions and tracking sunspot evolution. Although faculae and plages account for only a small fraction

of the observed photospheric luminosity, they contribute to the total solar irradiance (TSI) — the total energy per square meter received on Earth from the Sun across all wavelengths (from X-rays to radio waves). During periods of heightened solar activity, the increased luminosity from faculae and plages offsets the reduction caused by sunspots, raising the TSI by approximately 0.1% compared to periods of lower solar activity (Solov'ev et al. 2018).

1.2.6 Filaments and prominences

Solar filaments are dense plasma structures suspended in the Sun's atmosphere by magnetic fields. These formations are composed of relatively cool plasma, with temperatures ranging between 10^4 and 10^5 K, which contrasts sharply with the much hotter surrounding corona (Parenti 2014; Jenkins et al. 2022). Filaments appear as dark, elongated structures when viewed against the bright solar disk (e.g., in H-alpha observations) as a result of their lower temperatures and higher densities compared to the ambient plasma. They serve as valuable tracers of magnetic field lines in the solar atmosphere, providing insights into the Sun's magnetic topology.

At the solar limb, these structures are referred to as prominences and appear as bright, arch-like features set against the dark background of space. Despite their visual brightness, prominences remain cooler and denser than the surrounding coronal plasma. Quiescent filaments and prominences are generally stable, persisting for days to months, and are often associated with regions of relatively weak magnetic fields. In contrast, eruptive filaments and prominences are highly dynamic and unstable, typically forming in areas with more complex and stronger magnetic field configurations. These eruptive events are key drivers of CMEs and are therefore crucial for understanding solar activity and its impacts on SW.

1.2.7 Solar jets

Solar jets are long, thin, beam-like plasma structures that rise and fall back onto the Sun, though some may escape into the solar wind, carrying strong magnetic fields along. Coronal jets, as their name suggests, are observable in the corona, where they reach high temperatures on the order of a million K, which makes them visible in X-ray and EUV wavelength observations (Shibata et al. 1992; Innes et al. 2016; Raouafi et al. 2016). They are commonly observed

in active regions and exhibit velocities between 30–300 km/s, corresponding to kinetic energies ranging from 10^{25} to 10^{28} erg (Shibata et al. 1992). Coronal jets typically have sizes between 1–100 Mm, though some may extend over 100 Mm, and they last for several minutes to hours.

In contrast, spicules are jets that occur in the chromosphere (Secchi 1878; Roberts 1945; Beckers 1972). They are smaller structures, reaching heights of up to 10–20 Mm with widths under 1 Mm, and have shorter lifespans, often lasting less than 10 minutes. Due to their chromospheric origin, spicules are cooler, with typical temperatures around 10,000 K and generally below 50,000 K, making them observable in chromospheric spectral lines such as H-alpha and Ca II. Numerical modelling, particularly magnetohydrodynamic (MHD) simulations, is widely used to reproduce and better understand the propagation of spicules through the lower solar atmosphere (Martínez-Sykora et al. 2017; Mackenzie Dover et al. 2021).

Both spicules and coronal jets are classified into various types based on their characteristics and origin mechanisms. Solar jets can be triggered by processes such as magnetic reconnection (Innes et al. 2016; Skirvin et al. 2023), wave-driven mechanisms like slow and fast magnetoacoustic waves or Alfvén waves (De Pontieu et al. 2004; Liu et al. 2019; Stangalini et al. 2021), magnetic tension release combined with ambipolar diffusion (which induces a drift motion between the neutral and ionised components of a partially-ionised plasma, such as the chromosphere, e.g., see Martínez-Sykora et al. 2017; Martínez-Sykora et al. 2018), and granular buffeting.

For example, Roberts 1979 proposed that spicules result from resonance-induced, high-speed flow buildup within a magnetic flux tube, which is continually buffeted by granular motions in the photosphere. When this buffeting reaches a resonant frequency, it drives a strong axial plasma flow along the magnetic field lines, producing a visible spicule as the plasma rises into the chromosphere. This theory underscores the critical role of photospheric turbulence and resonance in the development of spicules. As pointed out by Liu et al. 2023, although solar jets are small-scale, localised events, they are governed by the solar cycle, which influences not only their latitudinal but also longitudinal behaviour (see Chapter 5). The interplay between local dynamo processes (which influence jet formation) and the global solar dynamo in the emergence and evolution of solar jets, including spicules, remains an open question.

1.2.8 Coronal loops

Coronal loops are prominent arch-like structures in the solar corona, often expanding over 100 Mm in length, with temperatures that can exceed 600,000 K and lifetimes lasting several hours. They consist of relatively dense plasma confined by magnetic fields (Reale 2010). The footpoints of coronal loops are anchored in the photosphere, where they connect regions of opposite magnetic polarity, creating a bridge that reveals the structure of the magnetic field extending into the corona. Coronal loops are of particular importance for tracking and studying magnetic field dynamics, as well as for understanding energy transport and heating mechanisms in the corona.

1.3 Observations and Sun monitoring

Monitoring and predicting SW events is essential to protect both space-based and terrestrial systems; however, forecasting remains challenging due to the wide range of temporal and spatial scales involved. For instance, photons reach Earth in about 8 minutes, SEPs can take from 10 minutes to several days, and CMEs typically arrive within 1 to 6 days. Each layer of the solar atmosphere provides unique insights into eruptive solar features, though each presents its own challenges. For example, the corona's magnetic field cannot be directly measured due to its low density, necessitating extrapolations from the photospheric magnetic field, e.g., as applied by Korsós et al. 2020 for solar flare forecasting. Another major challenge is determining the geoeffectiveness of SW events, which depends on factors such as the type of solar structures impacting Earth and, critically, the strength and direction of the magnetic field embedded in these structures. A powerful eruptive event might have limited geoeffectiveness, whereas a smaller-scale event with a dominant southward magnetic field component could cause severe damage on Earth.

Accurate forecasting of SW events requires continuous monitoring of solar activity through both ground-based and space-borne observatories, as each provides unique data that, when combined, enable a more comprehensive analysis. Ground-based observatories cannot detect EUV wavelengths, which are absorbed by Earth's atmosphere; thus, satellite observations are indispensable for studying the Sun's hottest atmospheric regions. Besides, newly developed instruments on space observatories now offer significantly higher spatial and

temporal resolutions. For instance, since its launch in 2018, the Parker Solar Probe has captured the closest images of the Sun to date, while the Solar Orbiter provides an unprecedented viewing angle of the Sun, particularly around the solar poles.

1.4 Notable space weather episodes

Many significant space weather events have been documented through visual observations or direct measurements, with the most famous being the Carrington Event of 1859. Carrington 1859 and Hodgson 1859 made one of the earliest recorded observations of an exceptionally intense solar flare, estimated to be around X45 in terms of X-ray intensity, corresponding to an energy release of approximately 5×10^{32} erg (Cliver et al. 2013). This flare was accompanied by a CME that travelled rapidly, reaching Earth in just 17.6 hours. The resulting geomagnetic storm produced auroras visible at very low latitudes, extending as far south as Panama. At the same time, GICs from the solar magnetic field embedded in the CME disrupted telegraph systems, with some even catching fire. Remarkably, a telegraph conversation was sustained for two hours without any battery power, relying solely on GICs. The Carrington Event marks the first clear recognition of the solar-terrestrial connection, when Carrington linked the solar flare effect, observed in a magnetometer at the Kew Observatory, to the geomagnetic storm that followed the next day. Notably, other significant space weather events were recorded prior to the Carrington Event, such as the one in February 1730, documented through historical aurora records in East Asia (Hayakawa et al. 2018). Similarly, East Asian records from March 1582 describe powerful auroras lasting for at least three days (Hattori et al. 2019), which were even observed in the skies of Portugal despite the full moon (Carrasco et al. 2020), underscoring the exceptional brightness of the auroras produced by the geomagnetic storm at that time.

In September 1770, bright red auroras were recorded in Japan and China, with additional observations in South-East Asia by Captain James Cook's expedition en route to Australia. This marks the first documented instance of simultaneous auroral sightings in both hemispheres (Willis et al. 1996). These auroras were visible in low-latitude areas for nine days, suggesting that the geomagnetic storm lasted even longer (Hayakawa et al. 2017). The storm was particularly intense; the recorded sunspot group associated with the geoeffective

eruption covered an area approximately twice the size of that linked to the Carrington Event. In 1872, another significant space weather event, known as the Chapman-Silverman Event, was documented in East Asia. This event disrupted telegraph systems, causing widespread communication failures across long distances, including the interruption of the British-Indian submarine cable in the Indian Ocean for several hours (Uberoi 2011). Comparable to the Carrington Event in terms of magnetic intensity, the Chapman-Silverman Event similarly highlights the vulnerability of contemporary technology to solar activity. It is particularly notable for its strong geoeffectiveness, despite being linked to a medium-sized, but highly complex active region with strong magnetic flux (Hayakawa et al. 2023).

In November 1882, a large sunspot group triggered another space weather event that disrupted telephone and telegraph systems (Love 2018). In October 1903, a fast CME, travelling at roughly 1500 km/s, instigated a strong geomagnetic storm. Uncommonly, this occurred during a solar minimum, demonstrating that intense space weather events can arise even during periods of low solar activity (Hayakawa et al. 2020). Later, in May 1921, the so-called New York Railroad Storm, caused by a series of ICMEs (Love et al. 2019), became notorious for the damage it inflicted on technological infrastructure. The storm led to fires in several facilities worldwide, including a control tower near New York's Grand Central Terminal and a telephone exchange in Sweden (Odenwald 2007). Additionally, the event produced powerful ionospheric disturbances that interfered with radio communication, causing either disruptions or, in some cases, unexpectedly enhancing long-distance radio propagation.

A few months before the outbreak of World War II, in January 1938, the Fátima storm occurred, marked by large auroral displays visible at low latitudes, including Fátima, Portugal. The event was named for its coincidence with the Fátima prophecy, which foretold that God would send a great sign in the sky as a warning of the impending war. The Fátima storm caused widespread electrical outages and disruptions, with some train lines in England becoming inoperable. Radio interference also disrupted communications, even affecting airline operations. The storm was triggered by several rapidly launched CMEs erupting from a large and complex active region, a characteristic often associated with the most powerful space weather events ever recorded (Hayakawa et al. 2021).

In September 1941, the so-called Geomagnetic Blitz struck, wreaking havoc

on the new technologies developed during the war. The nighttime auroral glow exposed an Allied convoy, leaving it vulnerable to German assaults (Love et al. 2016). Similarly, in May 1967, a powerful solar flare erupted during the Cold War, emitting electromagnetic radiation across a wide spectrum, from radio waves to X-rays, and was accompanied by solar radio bursts that caused significant ionospheric disturbances (Knipp et al. 2016). This event nearly led to a nuclear attack by the U.S. government on the Soviet Union, as the disruption of military high-frequency (HF) radio communications and polar surveillance radar was mistakenly attributed to Soviet interference. Fortunately, space weather forecasters from the Air Weather Service (AWS) issued a timely warning that the disturbances were due to solar activity. This was incredibly fortunate, given that space weather forecasting operations had only begun in the late 1950s, with the terminology itself being coined in 1957 (Cade III et al. 2015). The 1967 storm holds particular significance in the field of heliophysics, as it underscored the critical importance of understanding and monitoring solar activity, spurring the rapid development of space weather forecasting capabilities.

In August 1972, another solar storm caused significant technological disturbances in North America, marked by long-duration and intense solar flares. One of these flares was estimated to be an X20-class event, with emissions persisting for more than 16 hours above background levels (Knipp et al. 2018). This storm also produced extremely hazardous SEP events, which could have posed fatal risks to astronauts had they been on the Moon at the time. Additionally, it recorded the fastest CME transit time to date: only 14.6 hours, with the CME travelling at an extraordinary velocity of 2850 km/s (Vaisberg et al. 1976). In the context of the Vietnam War, this event reportedly caused the premature detonation of U.S. magnetic-influence sea mines, an outcome attributed by the U.S. Navy to the storm's effects, inadvertently saving Vietnamese vessels. One of the most extreme storms of the Space Age occurred in March 1989, plunging Quebec, Canada, into darkness. The storm also impacted satellites in space, with anomalies reported in NASA's Tracking and Data Relay Satellite (TDRS)-1 and a sensor aboard Space Shuttle Discovery due to high-energy particles infiltrating their electronics. A few months later, in August 1989, another geomagnetic storm, accompanied by a powerful X20-class solar flare, disrupted microchips and halted trading on Toronto's stock market (Talib et al. 2011).

Between 2000 and 2003, during the peak of Solar Cycle 23, several intense geomagnetic storms were recorded. Notable events include the storms in April 2000 and April 2001 (Huttunen et al. 2002; Sun et al. 2002), the latter being associated with a strong X20-class solar flare and marking the first storm of the Space Age to saturate space-borne observatories. In between, the Bastille Day solar storm of July 2000 (Andrews 2001) caused disturbances to power systems and spacecraft, while the November 2001 storm (Mishin et al. 2007) produced auroras visible in the southernmost regions of the U.S. This period culminated in the infamous Halloween solar storms of October 2003 (Dryer et al. 2004). A powerful solar flare, directed away from Earth, was estimated to be X45-class, making it one of the most intense ever recorded. Approximately half of the Earth-orbiting spacecraft experienced varying levels of disruption, affecting satellite radio communications and television broadcasts. The Advanced Earth Observing Satellite (ADEOS)-II was lost, while deep-space missions, including the Martian Radiation Environment Experiment aboard NASA's Mars Odyssey, were severely impacted. Other missions were forced into safe mode. These storms disrupted diverse sectors, including communications for airline flights and Antarctic science missions, as well as Global Positioning System (GPS) technologies used for land drilling, monitoring, and other applications.

During Solar Cycle 24, the strongest geomagnetic storm was the Saint Patrick's Day solar storm of 2015 (Jacobsen et al. 2016; Wu et al. 2016). However, a significant near-miss occurred in July 2012, when a powerful CME travelling at a speed of $3,050 \pm 260$ km/s near the Sun narrowly avoided Earth (Baker et al. 2013). Had it struck, it could have triggered a geomagnetic storm even more intense than the Carrington Event, with potentially catastrophic consequences for modern technology. This event underscores that even relatively mild solar cycles, such as Solar Cycle 24, can still produce exceptionally strong solar storms. In September 2017, another notable solar storm coincided with Hurricane Irma, compounding challenges for emergency response efforts. The storm disrupted high-frequency radio communications critical to aviation, maritime operations, and emergency services (Redmon et al. 2018). In February 2022, although the geomagnetic storm was relatively minor, it led to the unexpected failure of 38 Starlink satellites in low Earth orbit — i.e., at lower altitudes than geosynchronous satellites — due to increased atmospheric drag. The CME responsible for this event was relatively minor but inadequately predicted due to its poorly understood structure, highlighting the need to

study weaker CME structures in greater detail for improving space weather forecasting (Kataoka et al. 2022).

All these events demonstrate that strong solar storms are more likely during periods of heightened solar activity. However, such storms can also occur during solar minima or cycles of moderate activity. Weaker solar storms, too, have the potential to cause significant damage, especially if their structures are complex or predictions are untimely. A recurring pattern observed in many strong solar storms is the successive occurrence of CMEs (Liu et al. 2014). The passage of an initial CME often paves the way for a subsequent one to surge through rapidly, leading to CME-CME interactions. These interactions are a key characteristic of many intense solar storms, though they do not account for all such events. Further research is essential to uncover why some storms are more geoeffective than others, particularly as modern society becomes increasingly reliant on vulnerable technologies.

1.5 Thesis structure

This thesis is organised as follows. Chapter 2 explains the mathematical morphology methodology applied across the different projects in this thesis, with a particular focus on the operations used, its application to diverse fields — particularly space weather —, and its comparison with other image processing methods.

Chapter 3 evaluates the performance of this methodology in detecting sunspots from satellite data, specifically comparing the resulting sunspot area measurements with those from established sunspot databases and validating the findings.

Chapter 4 explores another application of mathematical morphology: the extraction of magnetic flux ropes from simulation data. This demonstrates the method's versatility, as it can be applied not only to solar observations but also to modelling data. The results show improvements over a previous method used in the literature, providing a more robust flux rope extraction scheme. This is crucial for accurately analysing the morphological properties of magnetic flux rope structures, as well as their propagation and orientation.

Finally, Chapter 5 describes the compilation of an extensive dataset of coronal off-limb structures observed during Solar Cycle 24 using mathematical morphology. This dataset enables statistical studies of the properties of these

features, such as their intensity and spatial behaviour, revealing notable trends like active latitudes and North-South asymmetry. It also provides further evidence for the existence of active longitude belts on the Sun, highlighting longitudinal preferences in coronal activity and suggesting new approaches to understanding and forecasting solar phenomena.

Chapter 2

Methodology and applications of mathematical morphology

2.1 Roots and definition

Mathematical morphology (MM) is a theory for image processing and analysis, developed in the early 1960s by French mathematicians Matheron 1967 and Serra et al. 1969. The primary motivation behind MM is to deliberately deform an image and, through these deformations, quantify the properties of the objects within it. Its theoretical foundation draws from topology, geometry, set theory, and lattice theory, which makes it highly effective for describing the structural shapes of objects in images (Haas et al. 1967; Serra 1982; Jeulin 1989; Heijmans 1995; Matheron et al. 2001; Serra 2020). Initially applied to the study and characterisation of porous media, MM has become a powerful tool in various fields that require image processing, including segmentation, feature extraction, noise removal, and other filtering processes (see Subsection 2.5). Although its application to space weather research is relatively recent (see Subsection 2.6), it has already proven valuable in this domain as well.

2.2 The role of the structuring element

Mathematical morphology relies on a fundamental component known as the structuring element (SE) to perform operations on images. The SE defines the local environment around each pixel during MM operations. Typically, it consists of a small binary shape selected to be simpler and smaller than

the features of interest in the image. The simplicity of the SE allows for easy interpretation of how morphological operations affect the image. Users can customise the shape of the SE based on the specific application and type of MM transformation being applied. Options range from basic shapes like squares, circles, lines, and crosses to any custom shape tailored for specialised operations. Additionally, users can specify the directionality of the SE, which aids in identifying features with preferred orientations (e.g., vertical, horizontal, diagonal, etc.) The careful selection of the SE — its size, shape, and orientation — is crucial as it directly impacts the image processing outcomes. This choice is influenced by the specific requirements of the desired application (for example, noise reduction versus feature detection, which necessitates different SE configurations), as well as by the characteristics of the objects under study in the image (i.e., sunspots, facular regions, solar jets, and filaments, among other features of interest in solar images).

Serra 1982 introduced the concepts of convexity and isotropy in SEs. Convexity pertains to the shape of the SE and whether it includes all line segments between any two points within it. For example, circular and square SEs are convex and generally produce more stable and predictable results, while non-convex SEs can lead to more complex and irregular changes in an image. Isotropy, on the other hand, refers to the uniformity of the SE in all directions, implying rotational symmetry and resulting in consistent effects across orientations. Circular and square SEs are both isotropic (in addition to being convex), whereas anisotropic SEs, such as linear or rectangular shapes, emphasise specific orientations. In the applications discussed in this PhD thesis — sunspot identification in Chapter 3, flux rope extraction in Chapter 4, and coronal off-limb structure detection in Chapter 5 — the SEs are selected to be both isotropic and convex, specifically with a circular shape.

2.3 Key operations

This section introduces two fundamental morphological operations: erosion and dilation (Matheron 1967). These operations are based on standard set operations such as intersection, union, and complementation. For grayscale images, the concepts of infimum and supremum are used instead. Additionally, the section explores advanced transformations that build upon erosion and dilation, including opening, closing, morphological gradient, and top-hat.

2.3.1 Erosion

Erosion can be defined in multiple contexts, including 3D images using graph theory. In this work, we focus on two specific definitions: the first in set theory, which also applies to binary images, and the second in grayscale image processing. In set theory, erosion represents the set of points where the structuring element is fully contained within the original set. Specifically, it includes all vector points $\mathbf{x}$ such that, when the SE is centered at $\mathbf{x}$, the entire SE belongs to the original set (see Equation 2.1, Soille 1999). This is also often denoted as $X \ominus S$, where X is the original set and S is the structuring element. In other words, erosion is the set of all points $\mathbf{x}$ for which the structuring element S translated by $\mathbf{x}$ (denoted $S_{\mathbf{x}}$ in Equation 2.1) fits entirely within X.

$$\epsilon_S(X) = \bigcap_{\mathbf{s} \in S} X_{-\mathbf{s}} = \{\mathbf{x} | S_{\mathbf{x}} \subseteq X\}. \tag{2.1}$$

$$\epsilon_S(f) = \bigwedge_{\mathbf{s} \in S} f_{-\mathbf{s}} \Longrightarrow \forall \mathbf{x}, [\epsilon_S(f)](\mathbf{x}) = \min_{\mathbf{s} \in S} f(\mathbf{x} + \mathbf{s}). \tag{2.2}$$

For grayscale images, erosion operates on pixel intensity, recognising that a grayscale image can be represented as a function mapping each pixel coordinate to its intensity value. The erosion of a grayscale image f by a structuring element S generates a new image where each pixel's intensity is determined by the minimum value within the neighbourhood defined by the SE centered at that pixel. This process reduces pixel intensities using a minimum operator, darkening regions where the SE overlaps with higher-intensity values (see Equation 2.2, Soille 1999). Thus, the erosion transform is a valuable tool in morphological image processing for enhancing the darkest regions, known as valleys, and reducing the intensity of the brightest regions, known as peaks, in an image.

2.3.2 Dilation

In addition to erosion, the dilation operation is another essential transformation underpinning mathematical morphology. In set theory, dilation refers to the set of points where the structuring element overlaps with at least one point of the original set. As described in Equation 2.3 (Soille 1999), and often denoted as $X \oplus S$ (where X is the original set and S is the structuring element), it

consists of all points $\mathbf{x}$ such that the intersection $S_{\mathbf{x}}$ of S translated by $\mathbf{x}$ with X is non-empty. Dilation thus increases the foreground of the original set while decreasing its background.

$$\delta_S(X) = \bigcup_{\mathbf{s}\in S} X_{-\mathbf{s}} = \{\mathbf{x} | S_{\mathbf{x}} \cap X \neq \emptyset\} \tag{2.3}$$

$$\delta_S(f) = \bigvee_{\mathbf{s}\in S} f_{-\mathbf{s}} \Longrightarrow \forall \mathbf{x}, [\delta_S(f)](\mathbf{x}) = \max_{\mathbf{s}\in S} f(\mathbf{x}+\mathbf{s}) \tag{2.4}$$

In grayscale images, dilation, akin to erosion, modifies the intensity of each pixel by sliding the SE across the image. However, in this case, the pixel's intensity is replaced by the maximum value within a defined neighborhood (i.e., the SE centered at that pixel), as shown in Equation 2.4 (Soille 1999). This results in brightening regions where the SE overlaps with lower-intensity areas. Therefore, the dilation operator is used to widen peaks and reduce valleys in images.

In summary, erosion and dilation are fundamental morphological transforms. Dilation is both commutative and associative, and it can be considered as an extensive filter if and only if the structuring element contains its origin. This implies that the dilated image will not be smaller than the original, provided that the origin is within the structuring element. Conversely, erosion acts as an anti-extensive filter, if and only if the origin is included in the structuring element, ensuring that the eroded image cannot be larger than the original. These properties are detailed in Equation 2.5, where $\mathbf{0}$ represents the origin vector of the structuring element S, and Id denotes the identity function.

$$\mathbf{0} \in S \iff \epsilon_S \leq \mathrm{Id} \leq \delta_S \tag{2.5}$$

Both operations exhibit translation invariance and increasingness. Increasingness maintains the ordering relation during the operation, whether it be the inclusion relation in sets or binary images, or the $\leq$ relation in grayscale images (refer below to Equations 2.6 and 2.7, respectively).

$$A \subseteq B \implies \epsilon_S(A) \subseteq \epsilon_S(B) \quad \text{and} \quad \delta_S(A) \subseteq \delta_S(B) \tag{2.6}$$

$$f \leq g \implies \epsilon_S(f) \leq \epsilon_S(g) \quad \text{and} \quad \delta_S(f) \leq \delta_S(g) \tag{2.7}$$

We recall in Equations 2.8–2.11 the characteristics of an ordering relation for two sets, A and B (left side), and two images, f and g (right side). Equations 2.8–2.10 describe the properties of a partial ordering relation: reflexivity (Equation 2.8), anti-symmetry (Equation 2.9), and transitivity (Equation 2.10). A total ordering relation additionally satisfies the trichotomy property, as shown in Equation 2.11. Erosion and dilation both preserve partial order for sets and binary images, and total order for grayscale images through the operations of infimum and supremum, respectively (thus ensuring that the minimum and maximum grayscale values used in these transformations are defined in a unique way, Soille 1999). However, they preserve this order differently, with erosion being anti-extensive and dilation being extensive (contingent upon whether the structuring element includes its origin, see Equation 2.5).

$$A \subseteq A \qquad f \leq f \tag{2.8}$$

$$A \subseteq B \text{ and } B \subseteq A \iff A = B \qquad f \leq g \text{ and } g \leq f \iff f = g \tag{2.9}$$

$$A \subseteq B \text{ and } B \subseteq C \implies A \subseteq C \qquad f \leq g \text{ and } g \leq h \implies f \leq h \tag{2.10}$$

$$A \subset B \text{ or } B \subset A \text{ or } A \cap B = \emptyset \qquad f < g \text{ or } g < f \text{ or } f = g \tag{2.11}$$

Erosion and dilation are not inverse transformations but are duals with respect to complementation. Each can be derived by taking the complement of the other. Specifically, the complement of the dilation of an image f equals the erosion of the complement of this image by the same structuring element S (Equation 2.12), and vice versa (Equation 2.13).

$$[\delta_S(f)]^{\mathsf{c}} = \epsilon_S(f^{\mathsf{c}}) \tag{2.12}$$

$$[\epsilon_S(f)]^{\mathsf{c}} = \delta_S(f^{\mathsf{c}}) \tag{2.13}$$

These two primary operations, erosion and dilation, are then combined to develop more complex operators, such as opening, closing, morphological

gradient, and top-hat transforms, which are presented in the next subsections.

2.3.3 Opening

The opening of a set X using a structuring element S is defined in Equation 2.14 (Soille 1999), and often denoted as $X \circ S = (X \ominus S) \oplus S$. This operation is achieved by eroding the original set X using each possible translation $S_{\mathbf{x}}$ of the structuring element S by $\mathbf{x}$, where $S_{\mathbf{x}}$ fits entirely within X. The union of all these eroded sets contained within X forms the final outcome of the opening operation.

$$\gamma_S(X) = \bigcup_{\mathbf{x}} \{S_{\mathbf{x}} | S_{\mathbf{x}} \subseteq X\} \tag{2.14}$$

$$\gamma_S(f) = \delta_{\check{S}}(\epsilon_S(f)) \quad \text{where} \quad \check{S} = \{-\mathbf{s} | \mathbf{s} \in S\} \tag{2.15}$$

In simpler terms, opening consists of an erosion operation with a structuring element S, followed by a dilation performed on the resulting eroded image using the reflected structuring element $\check{S}$ (Soille 1999, see Equation 2.15, where f represents the original image). The reflected structuring element $\check{S}$ is used during the dilation operation as it allows translations in the opposite direction of those applied with S in the erosion operation, thereby aiding in the recovery of the image. However, due to the irreversible nature of erosion, the original fine details of the image cannot be fully restored. This makes opening effective for smoothing object boundaries and removing protrusions or noise from foreground regions smaller than the structuring element — which reaffirms the critical importance of selecting the SE and its size appropriately. As depicted in Figure 2.1, the opening operation maintains the general shape of objects in images due to the subsequent dilation step. In grayscale images, opening reduces the intensity of smaller peaks or isolated noisy regions while preserving the overall intensity distribution of larger structures. It can also help separate connected objects with narrow connections between them. Moreover, employing opening as a pre-processing step can simplify the image and improve the efficiency of subsequent processing stages.

$$\gamma_R^{(S)}(f) = R_f^{\delta}[\epsilon^{(S)}(f)] \tag{2.16}$$

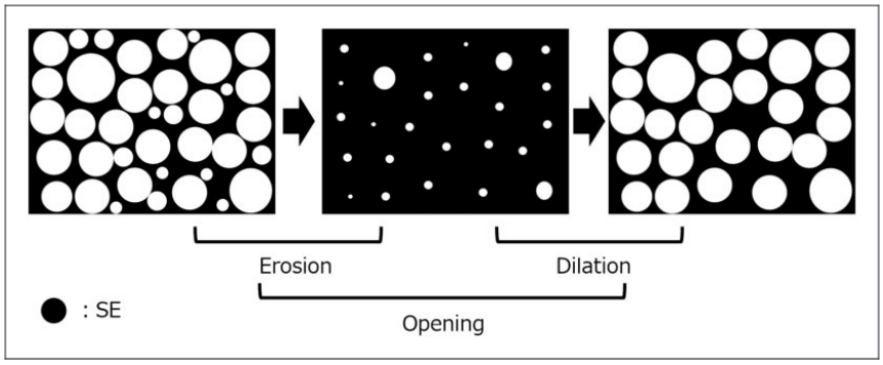

Figure 2.1: Two-step opening operation (erosion followed by dilation) on a binary image. The original image is processed, eliminating small white noise using erosion with a disk-shaped structuring element that is smaller than the structures of interest (large white circles) but larger than the noise (small white dots). The main structures are then restored through subsequent dilation using the same disk-shaped and similarly sized but reflected structuring element. Source: Matsumoto et al. 2017.

For a more refined approach with minimal impact on the overall image structures, one might consider applying an opening by reconstruction operation, as defined in Equation 2.16 (Soille 1999). This transform, as its name implies, integrates a reconstruction step into the dilation process. Initially, the original image is eroded using a carefully chosen structuring element to create a marker image. This marker image forms the seeds for reconstruction by highlighting the structures to be preserved (i.e., those containing the structuring element) while removing other elements. In contrast to standard opening, the subsequent dilation in the opening by reconstruction operation respects the connectivity of the marker image. This means that dilation only occurs in areas where the marker image was originally eroded by the SE, without altering other regions left untouched by the erosion. The image is then reconstructed by iteratively dilating it and intersecting the result with the original image, used as a reconstruction mask, until convergence is reached. By enforcing a connectivity constraint not present in standard opening, the opening by reconstruction operation allows for more precise and targeted processing, effectively reconstructing important features based on the marker image.

2.3.4 Closing

Closing is defined in Equation 2.17 as the complement of the union of all structuring elements fitting within the complement of the set or binary image (Soille 1999). It is often denoted as $X \bullet S = (X \oplus S) \ominus S$. Contrary to opening, the morphological closing first involves dilating the foreground objects in the original image using an SE, then eroding the resulting image with the reflected SE (see Equation 2.18). This process helps the dilated structures regain their original shapes while filling in gaps and holes. Closing can serve a similar purpose to opening in terms of removing noise — black background noise in binary images, as opposed to white foreground noise eliminated by opening — and smoothing contours. Additionally, closing can connect disjointed structures by filling gaps between them. In grayscale images, closing brightens dark areas, contributing to a general enhancement of the image, although this effect is less pronounced compared to the enhancement achieved through dilation alone with a similar SE.

$$\phi_S(X) = [\bigcup_{\mathbf{x}} \{S_{\mathbf{x}} | S_{\mathbf{x}} \subseteq X^{\mathsf{c}}\}]^{\mathsf{c}} \tag{2.17}$$

$$\phi_S(f) = \epsilon_{\check{S}}(\delta_S(f)) \tag{2.18}$$

Similar to the opening by reconstruction operation, a closing by reconstruction can also be performed using an iterative process. In this case, the marker image (the dilated image) is iteratively reconstructed through erosion, constrained by a mask (the original image) to preserve the connectivity of the structures within the mask. The iterations continue until stabilisation is achieved — that is, when the output image remains unchanged with further iterations (see Equation 2.19, Soille 1999).

$$\phi_R^{(S)}(f) = R_f^{\epsilon}[\delta^{(S)}(f)] \tag{2.19}$$

Closing and opening, like dilation and erosion, are increasing and dual operations with respect to complementation, as illustrated in Equations 2.20 and 2.21, respectively (with f and g representing images). Closing is an extensive morphological filter, so that the foreground in the dilated image is equal to or

greater than that in the original image, whereas opening is anti-extensive (see Equation 2.22). Both operations are idempotent transformations, which means stability is achieved after a single iteration: performing the same operation again (either opening on an opened image or closing on a closed image) will not further alter the result. Thus, applying opening (or closing) to an image that has already been opened (or closed) with the same structuring element returns the original opened (or closed) image, as shown in Equation 2.23.

$$f \leq g \implies \phi_S(f) \leq \phi_S(g) \quad \text{and} \quad \gamma_S(f) \leq \gamma_S(g) \tag{2.20}$$

$$[\phi_S(f)]^{\mathsf{c}} = \gamma_S(f^{\mathsf{c}}) \quad \text{and} \quad [\gamma_S(f)]^{\mathsf{c}} = \phi_S(f^{\mathsf{c}}) \tag{2.21}$$

$$\gamma_S(f) \leq f \quad \text{and} \quad f \leq \phi_S(f) \tag{2.22}$$

$$\gamma_S[\gamma_S(f)] = \gamma_S(f) \quad \text{and} \quad \phi_S[\phi_S(f)] = \phi_S(f) \tag{2.23}$$

2.3.5 Morphological gradient

The morphological gradient is another valuable operator derived from the fundamental operations of erosion and dilation. Defined by Beucher 1990, it is calculated as the difference between dilation and erosion (see Equation 2.24), and is thus also known as the Beucher gradient. This operator is particularly effective at highlighting object boundaries in images by identifying regions with significant variations in grey levels (or transitions between black and white areas in binary images). However, because the gradient can also emphasise noise, it is advisable to clean and filter the image before applying it in order to reduce unwanted artifacts. Typically, the morphological gradient is two pixels wide, though it can be larger. In such cases, it is referred to as a thick gradient when the SE exceeds a size of one pixel. Alternatively, half-gradients can be used to achieve a contour width of one pixel. The half-gradient by erosion is an internal gradient that detects the inner borders of an object (Equation 2.25), while the half-gradient by dilation enhances the external edges (Equation 2.26). These two half-gradients are complements, and their sum produces the Beucher

gradient (see Equation 2.27).

$$\rho_S = \delta_S - \epsilon_S \tag{2.24}$$

$$\rho_S^- = \mathrm{Id} - \epsilon_S \tag{2.25}$$

$$\rho_S^+ = \delta_S - \mathrm{Id} \tag{2.26}$$

$$\rho_S^- = (\rho_S^+)^{\mathsf{c}}, \;\; \rho_S^+ = (\rho_S^-)^{\mathsf{c}} \quad \text{and} \quad \rho_S^+ + \rho_S^- = \rho_S. \tag{2.27}$$

In this thesis, significant use is made of the morphological gradient, especially its external variation. For the extraction of magnetic flux ropes (see Chapter 4), a multi-scale gradient was also applied. The concept of a multi-scale gradient involves computing gradients at different scales to effectively capture the variations in object edges within an image. By using SEs of varying sizes, the multi-scale gradient can detect both fine details and larger structures.

In Chapter 4, we employed this approach to capture the boundaries of magnetic flux ropes across multiple scales using different SE sizes. Specifically, we utilised a two-scale morphological gradient, incorporating both a small and a larger SE, which enhances features that might otherwise be missed with a single-scale gradient. The gradient is computed at each scale (in this case, two), and the combination of these gradients — using the union for sets and binary images, and the maximum function for grayscale images — results in the output of the multi-scale gradient. Thus, the multi-scale gradient is powerful for enhancing edge detection by capturing object boundaries at different levels of detail, providing a more comprehensive extraction of the features of interest.

2.3.6 Top-hat

The top-hat transform, introduced by Meyer 1979, is a useful operator for isolating small peaks and valleys in an image. It works metaphorically like a top-hat (upright and inverted), retaining only the features that protrude through the hat (peaks and valleys) while erasing the background corresponding to the brim. Specifically, the white top-hat (or top-hat by opening) is calculated by subtracting the opened image from the original image (see Equation 2.28). The opening operation removes small bright features from the input image, while the white top-hat recovers and enhances these features by taking the difference between the original and opened images, effectively isolating them from the larger background structures.

$$WTH(f) = f - \gamma(f) \tag{2.28}$$

$$BTH(f) = \phi(f) - f \tag{2.29}$$

An application of the white top-hat transformation is demonstrated below in Figure 2.2, with three images taken on the same date, July 21, 2015. These images were processed using the same algorithms, including the white top-hat, though with slightly different SE values, to construct the contours of solar plages in these chromospheric images. Two of the images were captured by ground-based observatories: one from the Geophysical and Astrophysical Observatory of the University of Coimbra (OGAUC) in Figure 2.2(a) and another from the Astrophysical Observatory of Catania (CAO) in Figure 2.2(b)), both with similar pixel resolutions of 1–2 arcseconds per pixel. In contrast, Figure 2.2(c) presents a higher-resolution image from the AIA instrument aboard the SDO in the 1600 Å channel, with a resolution of 0.6 arcseconds per pixel. Given that solar plages appear bright against a darker background in these images, the white top-hat operation is particularly well-suited for their identification. It demonstrates its effectiveness across different image types, from high-resolution satellite images to less sharp ground-based observations, even when the spectroheliogram from OGAUC appears blurred on this date, underscoring the robustness of the white top-hat operation.

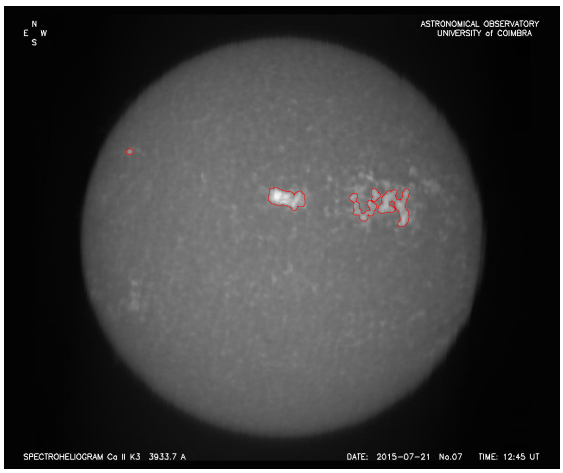

(a) Ca II K3 image from the OGAUC showing the chromospheric region of the Sun on 21/07/2015. Although the spectroheliogram is blurred on this date, chromospheric features such as solar plages are clearly visible and identified using the white top-hat transform.

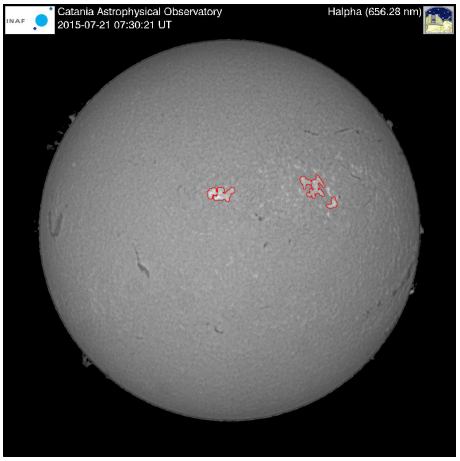

(b) Hα image from the CAO on 21/07/2015, where solar plages are identified using the white top-hat. Elongated filaments, appearing dark, are also visible and could be identified using the black top-hat operation.

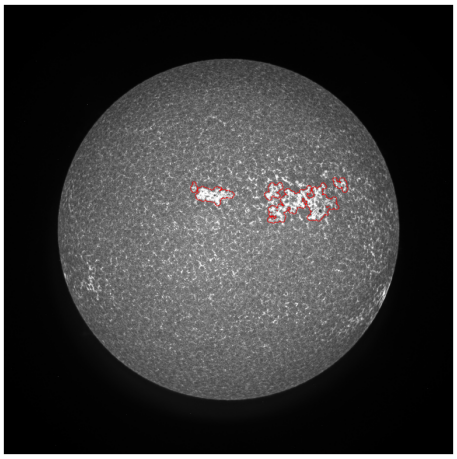

(c) SDO/ AIA 1600 Å (far ultraviolet) image from 21/07/2015, showing active regions, ultraviolet bright points, and sunspots. Solar plages are identified using the white top-hat transform.

Figure 2.2: Detection of solar plages using MM algorithms, including the white top-hat transform, across different types and resolutions of solar images: ground-based images in panels 2.2(a) and 2.2(b) and space-borne observations in panel 2.2(c). Solar plages are outlined in red on the original images.

Similarly, the black top-hat (or bottom-hat or top-hat by closing) is defined as the difference between the closed and original images, as shown in Equation 2.29. This operator first eliminates small dark features smaller than the SE through the closing operation, then recovers these features by subtracting the original image. For example, it could be used to highlight the darker borders between bright granules on the photospheric surface of the Sun. Figure 2.3 illustrates the application of the black top-hat transform for sunspot identification across three images: Figures 2.3(a) and 2.3(b) are H-alpha continuum images from the OGAUC and the CAO, respectively, whereas Figure 2.3(c) is an intensity image from the HMI instrument aboard the SDO spacecraft. Figures 2.3(a) and 2.3(c) were captured on the same date (June 21, 2015), while Figure 2.3(b) was taken the following day due to a lack of observations from the CAO on June 21. Since sunspots are very dark and sharply contrasted against the background in these images, the black top-hat operation effectively delineates the sunspot boundaries across all three images. However, slight variations in the identification of sunspot groups, particularly those located on the right-hand side of each image, are observed. In the high-resolution SDO image (Figure 2.3(c)), the black top-hat transform captures the sunspot boundaries with a high level of detail.

Black and white top-hats are complementary, and their sum $\phi - \gamma$ highlights both peaks and valleys simultaneously. However, in practice, as with the morphological gradient, noise in the image can compromise the top-hat transform's effectiveness if the image is not pre-filtered. Typically, one may use a closing operation to remove small valleys and smooth out the background before applying a white top-hat, while conversely, an opening operation can be used to remove small peaks before applying a black top-hat to the image. These both transformations are widely used, particularly for contrast enhancement and correction of uneven illumination, as they can smooth and fade the image background while enhancing structures of interest.

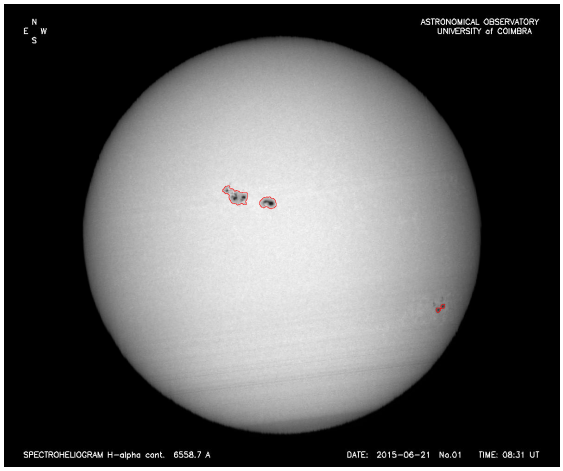

(a) H-alpha continuum image from the OGAUC showing the photospheric region of the Sun on 21/06/2015. Sunspots are identified using the black top-hat transform. Although two small sunspots on the right-hand side of the image are missed, the detection is effective despite suboptimal meteorological conditions, as indicated by the long stripes suggesting the presence of clouds.

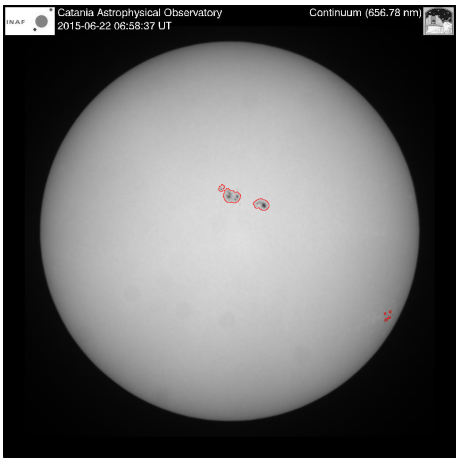

(b) Continuum image from the CAO on 22/06/2015.

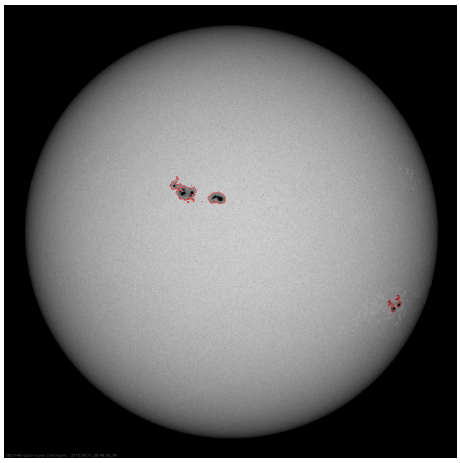

(c) SDO/HMI intensity image on 21/06/2015.

Figure 2.3: Sunspot identification using the black top-hat transform. Sunspot regions are outlined in red in ground-based observatory images from the OGAUC (panel 2.3(a)) on 21/06/2015 and the CAO (panel 2.3(b)) on 22/06/2015, as well as in a high-resolution image from the SDO satellite on 21/06/2015 (panel 2.3(c)).

2.4 Comparing MM with other image processing techniques

We will now discuss the strengths (Subsection 2.4.1) and limitations (Subsection 2.4.2) of the MM method, particularly in comparison to other techniques. Special emphasis will be placed on comparing MM with machine learning methods in Subsection 2.4.3.

2.4.1 Strengths of MM

The foundational concepts and operators of MM, discussed in previous sections, reveal numerous advantages of this theory. MM is versatile and can be applied to both binary and grayscale images (Matheron 1967; Serra et al. 1969; Iwanowski et al. 1997). Unlike linear image processing methods that primarily focus on intensity, MM is shape-oriented and excels in extracting geometric and topological information from complex structures using structuring elements. SEs can be tailored to different image types, geometric features, and applications, providing MM with great adaptability.

MM also demonstrates strong robustness, particularly in maintaining connectivity (Soille 1999). For example, opening and closing operations can remove noise while preserving connectivity, whereas other filtering techniques might distort structures of interest. Gaussian filters, for instance, can blur edges and essential details during noise reduction. This robustness is evident in morphological reconstruction operations, like opening or closing by reconstruction, which keep key features intact, making MM highly effective for noise reduction tasks (Wang et al. 2014). Additionally, MM is precise in edge extraction, focusing on the shape of object boundaries rather than merely on intensity gradients, unlike methods such as the Canny edge detector (Zhang et al. 2010; Xu et al. 2019). Moreover, MM supports multi-scale analysis using different SEs in multi-scale gradient operations, effectively handling images with features of varying sizes (Lirui et al. 1991).

MM is not constrained by linearity, which gives it several advantages over traditional linear image processing techniques such as Gaussian filtering, the Fourier transform, or convolutions. These linear methods are often simpler to use and understand because their output is a direct consequence of the input through the principles of superposition and homogeneity. However, they do not

account for the shapes and geometry in images. Linear techniques typically rely on pixel intensity values, providing uniform noise reduction, which can make it challenging to preserve shapes and edges that are at the same intensity level as the noise. Linear operators that are proficient at enhancing edges, like the Laplacian of Gaussian, risk amplifying noise. In contrast, MM is powerful because it operates locally and considers the spatial relationship between pixels in addition to their intensity. For example, the top-hat transform highlights peaks or valleys in an image based on their relative intensity value, rather than their absolute value, by considering the surrounding neighbourhood defined by the SE (Meyer 1979; Bright et al. 1987). This local approach explains why MM outperforms traditional thresholding techniques, which are more susceptible to intensity variations and can yield poor results in cases of uneven brightness.

Finally, MM is non-parametric, requiring no predefined parameters to describe the data distribution. Although MM does involve empirical tuning of the structuring elements to match image features, it applies transformations directly to the image without the need for model fitting. Consequently, MM sidesteps the complex mathematical assumptions inherent in parametric methods, such as polynomial fitting, which often rely on optimisation techniques. This non-parametric nature allows MM to be versatile across various contexts, whereas parametric methods may struggle with unpredictable data or diverse image types and conditions. While parametric techniques can be highly effective when solid model assumptions are met, they are typically confined to specific data and applications.

MM thus combines the benefits of non-parametric and nonlinear methods while offering greater flexibility and/or accessibility compared to many other nonlinear techniques, such as median, min, max, and bilateral filters. For instance, median filtering is fast and straightforward but less versatile in handling different sizes and shapes of noise. In contrast, bilateral filtering effectively reduces noise and preserves edges but is computationally demanding and requires careful parameter tuning. MM, however, provides intuitive and direct control over image structure geometry and adapts well to various applications. The selection of the appropriate method, therefore, depends on the specific needs and tasks at hand, requiring a compromise between the model-based advantages of parametric techniques, the predictability and global perspective of linear methods, and the unique qualities of MM mentioned above. The MM approach is particularly well-suited for this PhD research and is specifically

employed due to its exceptional capability in extracting features of interest from solar image data. This capability can be further enhanced when combined with other methods, such as neural networks (refer to Section 2.4.3 for a more detailed description and references) or more traditional image analysis techniques, where it can serve as a pre- or post-processing step for thresholding (Shih et al. 2003), region growing (Aschwanden 2009), Sobel (Zhang et al. 2015; Han et al. 2020) and Canny (Zhang et al. 2010; Liu et al. 2011; Xu et al. 2019) edge detectors, among others.

2.4.2 Limitations of MM

MM also has some weaknesses, many of which are the inverse of its advantages; however, these can be mitigated when the tool is applied to appropriate applications. As noted in the previous subsection, while MM is effective for analysing localised and detailed features, it is less suited for evaluating global image properties compared to linear processing techniques. This limitation arises because MM operations primarily focus on the local relationships between pixels within an environment defined by the SE, making it challenging to capture broader image patterns that require a more global perspective. Although MM is robust against certain types of noise by taking into account the local environment, it can still be vulnerable to noise within the SE's neighbourhood itself. For instance, in the case of an erosion operation, even a few noisy pixels within the SE can significantly alter the result, as these outlier pixels might be treated as actual image features, leading to over-eroded or distorted outputs. This sensitivity can limit MM's effectiveness in handling high levels of random noise unless it is combined with pre-processing noise-reduction techniques. The nonlinear nature of MM might also complicate the interpretation and analysis of results; therefore, a simple-shaped SE is preferable to facilitate understanding of how MM transforms operate on and modify images.

Additionally, applying MM to colour images or multi-dimensional data can be more complex, as it requires advanced vector-based operations or separate processing of each colour channel independently (Samir et al. 2024). In this PhD thesis, the MM algorithms developed for solar feature extraction are straightforward and utilise the basic operators described in the previous section; hence, they require little computational resources. However, more complex MM transforms, particularly iterative ones like morphological reconstruction (Karas

2011) or those involving large-sized SEs, can be computationally intensive compared to simpler processing methods.

MM may also be less suitable for signal processing tasks that require frequency-domain operations, where techniques like Fourier transforms are more appropriate. Indeed, MM excels at extracting shapes and geometrical properties of features in the time and spatial domains, making it ideal for tasks where the temporal pattern or structural characteristics of features are more critical than their frequency content. However, MM does not directly handle the frequency domain or extract the frequency components of a signal (e.g., audio signals), although some promising studies have applied MM techniques to music signal analysis (Romero-García 2023). In contrast, Fourier transforms are specifically designed to decompose a signal into its sinusoidal components, revealing periodicities, oscillatory patterns, and harmonics within the data. Nonetheless, Fourier analysis techniques are less suited for non-stationary signals and can distort geometric features, limiting their ability to extract shape information (Maragos 2009). Integrating MM with frequency-domain methods like the Short-Time Fourier Transform (STFT) leverages the strengths of both approaches (Luo et al. 2007; Rivest 2011). This combination benefits from the global frequency information provided by Fourier analysis while incorporating the local shape details captured by MM, making it a comprehensive tool for signal analysis.

Moreover, one of the most significant challenges with MM is its sensitivity to parameter (i.e., SE) selection, which can make it a refined but time-consuming approach (Shen et al. 2019). The process of manually selecting parameters can be excessively laborious and complex, especially when dealing with intricate images or advanced tasks. The SE must be customised to fit the specific context and characteristics of the image, making automation difficult and necessitating meticulous tuning for each image or new application.

2.4.3 MM versus Machine Learning

Machine Learning (ML) is a subfield of Artificial Intelligence (AI) focused on developing algorithms that emulate human learning processes. These algorithms are designed to automatically improve their performance over time by analysing and learning from large datasets (Géron 2017).

According to Aschwanden 2009 and Camporeale 2019, the application of

ML techniques in the field of space weather is experiencing rapid growth due to three primary factors. First, there is now unprecedented access to vast amounts of data — on the order of petabytes (Chamberlin et al. 2012) — which continues to expand. Second, recent advancements in hardware, particularly in Graphics Processing Units (GPUs), have significantly enhanced the capabilities for training ML algorithms. Third, the widespread adoption of open-source software, driven by substantial investments from major Information Technology (IT) companies such as Google, has further facilitated the use of ML techniques. Consequently, ML is now employed across a wide range of sectors, and its application is particularly well-suited to space weather, where the volume and complexity of data are continually increasing. ML appears to be a promising tool for developing real-time space weather forecasting models, leveraging the vast amounts of available space- and ground-based data. For example, Georgoulis et al. 2021 introduced the Flare Likelihood and Region Eruption Forecasting (FLARECAST) project, which employs various ML techniques to predict the occurrence and likelihood of solar flares. However, challenges remain, as the space weather community generally places greater trust in physics-based models over ML algorithms, which are often criticised for their lack of transparency and interpretability, a concern commonly referred to as the black box problem (Camporeale 2019).

Among machine learning techniques, Neural Networks (NNs) are particularly widely used. Modeled after the structure of human biological neural networks, NNs operate within the framework of supervised learning. In supervised learning, a function maps inputs to outputs based on examples of input-output pairs, which serve as training data. An NN comprises an input layer, an output layer, and one or more hidden layers, each consisting of neurons with associated weights. A neuron is activated when its output surpasses a threshold, after which it transmits data to the subsequent layer. The term Deep Learning (DL) is used when an NN includes multiple hidden layers. DL has been extensively applied in solar physics, with examples including solar event detection (Baek et al. 2021), active region identification (Quan et al. 2021), solar filament recognition (Peng et al. 2013), solar image classification and EUV prominence detection (Armstrong et al. 2019), flare forecasting (Huang et al. 2018), sunspot extraction and classification (Chola et al. 2022), and handwritten character recognition in sunspot drawings (Zheng et al. 2016), among others.

Compared to ML models, MM algorithms are generally simpler and offer more interpretable operators. ML models, on the other hand, are more computationally demanding and require large quantities of high-quality data for training. However, ML models are more flexible and adaptable to complex tasks, as they automatically learn and adjust their parameters through processes like backpropagation. In comparison, SEs in MM must be manually configured. Thus, MM and ML techniques are complementary; when effectively combined, they can achieve high performance, interpretability, and automation in tasks such as solar feature identification.

For instance, Mondal et al. 2020 integrated these two methods into a Morphological Neural Network (MNN) combining multiple erosion and dilation layers. Similar to a convolutional layer in a Convolutional Neural Network (CNN), a dilation (or erosion) layer in an MNN applies a learnable filter (an SE rather than a kernel) to probe and analyse the image. In a traditional convolutional layer, the filter slides across the input image, performing element-wise multiplication with the local region of the image and summing the results to produce a single value in the output feature map. Conversely, in a dilation (or erosion) layer, the SE slides across the image and applies a maximum (or minimum) operator to the local region defined by the SE. In the MNN developed by Mondal et al. 2020, the SEs in each morphological layer are initially randomly initialised and then optimised during training using backpropagation to minimise the loss function, similar to how kernels are optimised in CNNs. Mondal et al. 2020 achieved excellent qualitative results for removing both rain and haze from images. Metric evaluations, including the Structural Similarity Index Measure (SSIM) and the Peak Signal-to-Noise Ratio (PSNR), indicate that the MNN performs comparably to a traditional CNN with a U-Net architecture, while dramatically reducing the number of parameters and thus the computational cost.

MNNs were first introduced by Davidson et al. 1990 and Ritter et al. 1996, who described how these networks induce non-linearity prior to thresholding, in contrast to traditional NNs where non-linearity is applied after thresholding via a nonlinear activation function. These early studies were further expanded by Shen et al. 2019 and Hirata et al. 2021, who provided detailed applications and insights into the functioning of MNNs. Building on this foundation, Nogueira et al. 2019 developed a DL network called DeepMorphNet, which employs MM operations instead of traditional linear convolutions. Similarly, Roy et al. 2021

built MorphConvHyperNet, a network combining morphological erosion and dilation operations within a CNN framework. MorphConvHyperNet demonstrates superior performance compared to traditional CNNs in processing remote sensing hyperspectral image data, effectively extracting both spatial and spectral information. This success highlights the advantages of leveraging the inherent non-linearity of MM operations and their suitability for handling the complexity of hyperspectral images.

Derivaux et al. 2007 explored the advantages of integrating machine learning with mathematical morphology, specifically the watershed transform, in a segmentation algorithm applied to interpret multispectral very high-resolution (VHR) images. In this approach, the MM watershed transform is informed by machine learning. The image undergoes pixel classification using a supervised fuzzy method instead of the traditional gradient-based approach. This classified image is then processed by the watershed operation, leading to improved outcomes compared to the gradient-based pre-processing. Furthermore, Derivaux et al. 2007 tackle the common issue of oversegmentation associated with the watershed transform by incorporating a genetic algorithm to automatically tune the MM watershed parameters. Additionally, Franchi et al. 2020 demonstrated the effectiveness of incorporating MM layers into deep NNs for image denoising, showing that these layers can outperform convolutional layers, particularly in removing salt-and-pepper noise. Moreover, they highlighted the benefits of combining MM layers with convolutional layers for enhanced edge detection.

MNNs thus represent a recent and emerging architecture within the field of image processing. To date, MNNs have primarily incorporated basic operations such as erosion and dilation, but the introduction of more complex morphological operations could potentially enhance the network's expressiveness. Systematic evaluation and comparison with other neural network architectures trained on identical datasets are necessary to fully understand the capabilities and limitations of MNNs. It would be particularly valuable to further explore hybrid networks that integrate both convolutional and morphological layers. Additionally, other neural network architectures, such as recurrent networks, could be combined with morphological operations — for example, in tasks requiring thinning transforms, which are typically achieved through iterative erosion operations. Moreover, MNNs might offer a solution to the black box problem by providing geometrical and topological insights into the network's

functioning. Since the learned weights determine the size and shape of the SEs, they can reveal how the network processes images through geometrical operations, thereby enhancing interpretability.

Building on the integration of ML and MM, recent work submitted to A&A (see list of publications, Chierichini et al.) has explored this approach. Specifically, a ML algorithm — the Random Forest model — was trained on a large dataset generated through morphological operations (see Chapter 5). This dataset comprises coronal off-limb structures and their properties spanning Solar Cycle 24. Within this dataset, jets were labelled using the jet catalogue developed by Liu et al. 2023; Soós et al. 2024; Liu et al. 2024. The trained algorithm was then employed to identify coronal jets in unlabelled data, with the results being visually verified using video sequences. Of the 3452 candidates, the algorithm successfully identified 3268 true positives (with 184 false positives), demonstrating both the effectiveness of the model and the promising potential of combining ML with MM.

2.5 Applications of MM in diverse fields

Morphological image processing has been applied across various sectors, including the medical field (Prêteux 1992; Kimori 2011; Zhao et al. 2012). In medical imaging, MM is utilised to enhance images such as X-rays, Computed Tomography (CT) scans, and Magnetic Resonance Imaging (MRI) (Firoz et al. 2016). Indeed, medical images are often subject to noise and poor contrast due to technical constraints of the imaging devices, emergency situations, or patient-specific conditions and movements during the imaging process, all of which can degrade image quality. MM's ability to smooth noisy and blurred images, as well as address non-uniform backgrounds containing irrelevant medical structures, allows for enhanced visualisation of objects of interest. This capability facilitates early detection of potentially serious diseases through improved image clarity and user interaction (SE fine-tuning).

For instance, MM can aid in diagnosing tumours at an early stage using MRI images. Devkota et al. 2018 implemented morphological reconstruction in the segmentation process of brain tumours of various types and sizes. Their approach achieved better accuracy and computational efficiency compared to other methods like the Fuzzy C-Means method, which was prone to image intensity effects. This advancement assists in determining whether a tumour is

benign or malignant. Similarly, Chaturvedi et al. 2019 evaluated the influence of the SE on the shape, size, and edges of identified tumours in brain CT scan images. They employed simple MM operations to enhance image contrast, thereby improving the visual distinction between different organs and body structures, which are often intertwined and difficult to differentiate from cancerous cells.

In medical imaging, MM is also used to detect organ edges while simultaneously removing noise at a preliminary stage before segmentation. Yu-Qian et al. 2005 demonstrated that an appropriate combination of opening, closing, and dilation operations yields better results in identifying lung edges in CT images compared to a simple morphological gradient, highlighting the importance of choosing an adequate sequence of MM operators to achieve the desired outcome. They also showed that this method outperforms other edge-detection methods such as the Laplacian of Gaussian and the Sobel detector. Hassan et al. 2015 employed MM operations as a pre-processing step to smooth retinal images for blood vessel segmentation using K-means clustering, facilitating the early detection and diagnosis of diseases like diabetic retinopathy. MM is essential in this context as vessel structures are complex, requiring consideration of their shape, diameter, and tortuosity for accurate identification. Hassan et al. 2015 utilised various SEs in 12 different directions to fit and identify all vessels. Sohini et al. 2015 applied MM for enhancing fundus images with morphological reconstruction. Kaiqiong et al. 2011 used morphological multi-scale enhancement and top-hat transforms on angiograms to extract the vascular tree, employing varying-sized linear rotating SEs to adapt to the vessel structure, before recovering the vessel boundaries with morphological watershed. The multiscale operator is particularly helpful as it aids the anti-extensive opening operation in dealing with intensity discontinuities and local noise by using SEs of varying sizes. The application of operators employing multi-scale SEs has been extensively explored in eye imaging, yielding effective vessel extraction (e.g., see Miri et al. 2011; Hou 2014). This approach has also proven beneficial in other medical imaging domains, such as enhancing radiography images of bones and ribs (e.g., see Gaona et al. 2023). Other applications of MM in the medical sector include morphological cell analysis (Chen et al. 2012), vessel detection (Zana et al. 2001), and the counting, shape analysis, and segmentation of red blood cells (Anoraganingrum 1999; Ma et al. 2002; Angulo 2008; Maji et al. 2015).

MM techniques have been extended to various domains beyond the medical sector, particularly in processing remote sensing data (Dong 1997). For instance, MM has been utilised in urban planning and disaster management with automatic building extraction from high-resolution satellite images (Gavankar et al. 2018). It is also effective in land classification and environmental monitoring, such as forest classification (Üstüner et al. 2019) and biodiversity conservation (Matsumoto et al. 2017). Additionally, MM techniques are employed to track beach erosion by extracting coastlines from satellite data (Rishikeshan et al. 2017). Puissant et al. 2008 further demonstrated successful shoreline extraction by applying different MM algorithms and parameters tailored to the type of coastline, achieving excellent results in identifying sandy beaches, dunes, wetlands, and cliffs in multispectral VHR images. MM is also widely used in agriculture for soil analysis, landscape preservation, early detection of plant diseases, and crop monitoring. For example, Pina et al. 2006 used high-resolution satellite data for olive tree pattern segmentation and recognition. Moreover, MM has applications in geology (Beucher 1999), oceanography for detecting and studying mesoscale ocean structures such as warm-core eddies (Lea et al. 1993), and hydrogeology to better understand pollutant transport in hydrogeological systems (Pina et al. 2001).

Due to its shape-based approach, MM is obviously well-suited for computer vision tasks (Haralick 1988; Roerdink 1996) such as object detection and recognition in images and videos. It is also employed in biometrics, including fingerprint identification (Humbe et al. 2007), face feature extraction (Upraity et al. 2014), and iris identification (Mira Jr et al. 2013). Moreover, MM has been applied in military contexts, such as determining coastal water depth (Lea et al. 1996) and improving sea-sky-line detection in low-visibility conditions (Wenqi et al. 2018). Wenqi et al. 2018 showed that MM outperforms other image processing techniques, like simple Gaussian filtering, in sea-sky-line detection. Additionally, MM is particularly useful in industrial inspection for defect detection. For instance, Muslim et al. 2020 used MM to track potholes in roads from videos, ensuring user safety. MM also proves beneficial in the field of engineering materials (Coster et al. 2001), where it can be used for assessing damage and planning material replacements, as well as in cultural heritage preservation, particularly in artifact restoration and art conservation (Dramdahl 2014).

MM is further applied in the astrophysical domain, notably for celestial

object characterisation (Candéas et al. 1997). It addresses the star/galaxy discrimination problem encountered in astronomical image data, where distant galaxies can appear as point-like stars due to limitations in the resolution of observational instruments and blurring effects of the Earth's atmosphere in ground-based observations. MM is also used to detect and analyse the structure and dynamics of galaxies. For example, Aptoula et al. 2006 performed the MM watershed transform for galaxy segmentation on multispectral images and then classified galaxies into spiral and elliptical types using the top-hat operation (described in Subsection 2.3.6). Moore et al. 2006 demonstrated that MM performs comparably to traditional classification techniques in galaxy morphology classification.

2.6 Applications for solar physics research

As discussed in the previous section, MM has been extensively used in medical imaging, industrial inspection, and remote sensing for land cover and environmental monitoring on Earth. Its application has also extended to the astrophysical domain, particularly for celestial object detection and galaxy classification. More recently, MM has been applied to space weather and solar physics. One of the earliest implementations of MM algorithms on solar images to uncover solar features focused on detecting sunspots. Indeed, several studies have utilised MM for identifying sunspots (Zharkov et al. 2005; Curto et al. 2008; Zhao et al. 2016; Ling et al. 2020; Carvalho et al. 2020; Bourgeois et al. 2024a; see Chapter 3 for more references on the use of MM in sunspot detection) and active regions (see Benkhalil et al. 2006; Yan-mei et al. 2021). Additionally, MM has been applied to the extraction of solar plages in chromospheric images. For example, Barata et al. 2018 performed MM operations on Ca II K3 full-disk spectroheliograms from the OGAUC during Solar Cycle 24, achieving effective solar plage extraction.

MM has also been applied to filament recognition. For instance, Fuller et al. 2005 employed MM operators like morphological closing, thinning, and pruning on Hα images from the Meudon Observatory to obtain the skeleton structure of filaments and retrieve their main properties, such as length and curvature. Al-Omari et al. 2007 also used MM techniques on Hα images from the same observatory to filter out noise, thereby improving the performance of the subsequent filament recognition method developed by Qahwaji et al. 2005.

Meanwhile, Shih et al. 2003 utilised an intersection of closings with eight linear SEs oriented in different directions to accommodate different filament shapes and orientations, followed by an additional closing operation with a circular SE to eliminate residual noise around the filaments. This method yielded excellent results, particularly in detecting large filaments in Hα full-disk images from the Big Bear Solar Observatory (BBSO), enabling effective tracking of their evolution. Qu et al. 2005 further refined this approach on Hα images from the BBSO by automatically retrieving not only filaments but also their spines and footpoints, thereby providing an effective means of studying filament disappearances. Koch et al. 2015 developed the FILFINDER method, which integrates various processing techniques, including MM operations, for filament extraction from astronomical data, namely, the Herschel Gould Belt Survey data (André et al. 2010) and the California Molecular Cloud data (Harvey et al. 2013). FILFINDER can successfully detect both large filaments in star-forming molecular cloud regions and fainter filamentary structures, termed striations, located near these molecular clouds. It thus allows for a detailed investigation of the width, stability, orientation, and brightness of these structures. Scholl et al. 2008 focused on detecting both solar filaments and coronal holes using an automated method that incorporates MM operations, such as erosion. Their approach combines EUV images from the Extreme ultraviolet Imaging Telescope (EIT) instrument (Fe IX/X 171 Å, Fe XII 195 Å, and He II 304 Å lines) with magnetograms from the Michelson Doppler Imager (MDI) aboard the Solar and Heliospheric Observatory (SoHO) (Scherrer et al. 1995).

In this PhD thesis, MM is initially employed for sunspot detection in the next chapter to validate its robustness. Subsequently, in Chapter 4, MM is applied to simulation-generated data to extract magnetic flux rope structures within two distinct active regions. In Chapter 5, MM is further utilised on space-borne observations to detect coronal off-limb structures and analyse their statistical properties over an entire solar cycle.

Chapter 3

Sunspot identification using SDO/HMI full-disk intensity images

In this chapter, we present the sunspot detection method developed in Bourgeois et al. 2024a, which enables precise and automated measurements of sunspot areas. As discussed in Section 1.2.4, sunspots serve as a key indicator of solar activity, reflecting concentrations of magnetic flux on the photosphere. Assessing solar activity through sunspot counting is highly valuable, as it has been in use for centuries, providing a long-term record of solar activity over multiple solar cycles. Evaluating solar activity based on sunspot numbers and areas, both historically and currently, allows for the prediction of future space weather events such as CMEs (see Section 1.2.1) and solar flares (see Section 1.2.2), which primarily originate from complex sunspot configurations with strong and intricate magnetic fields. For instance, in the Mount Wilson classification, delta-sunspots are complex sunspot formations containing several umbrae of opposite polarities within the same penumbra. The Mount Wilson classification categorises sunspot groups based on their magnetic field topology and complexity, ranging from the simplest unipolar forms to more complex multipolar configurations (e.g., alpha, beta, gamma, delta, and combinations of these classes; see Nikbakhsh et al. 2019). Among these categories, delta-sunspots are the most unstable, with opposite magnetic polarities in close proximity. These closely situated opposite polarities are indeed prone to magnetic interactions,

such as reconnection, potentially leading to solar flares. Notably, delta-sunspot configurations are highly correlated with the most powerful flares, specifically those classified as X-class in the Geostationary Operational Environmental Satellite (GOES) X-ray flux classification (Patty et al. 1986; Shi et al. 1993, 1994). Moreover, Korsós et al. 2014, 2015a,b, 2018, 2019 and Erdélyi et al. 2022 demonstrated that specific patterns in the horizontal gradient of the magnetic field around the polarity inversion line between two opposite polarities in delta-sunspots are strongly linked to the eruption of X-class solar flares. Therefore, detecting and classifying sunspots is essential for better understanding and predicting solar eruptions.

3.1 Manual vs. automated approaches

Robust methods for sunspot detection and classification are indispensable for space weather forecasting. While manual methods were needed and useful (e.g., the hand-drawn sunspot catalogue from the Debrecen Heliophysical Observatory (DHO) used in this study), they are no longer viable. This is due to the increasing volume of data from both ground-based observatories and space instruments, which are becoming more numerous and complex to process with higher spatial and temporal resolution. Automated detection methods enhance efficiency and reduce human error, bias, and subjectivity, as sunspot counting can be data-dependent and vary significantly between observers. Indeed, even with automated methods — and because these methods are not yet standardised nor synchronised —, significant differences may arise between sunspot records due to variations in facilities and recording devices, observational methods, seeing conditions, image processing techniques, etc. However, automated methods are more easily adaptable to different data sources and can sometimes be applied to both ground-based and space-borne image data without further processing (e.g., MM algorithms, as illustrated by the applications of the white and black top-hat operations in Figures 2.2 and 2.3).

Recently, many studies have employed ML techniques for the automatic detection and classification of sunspots. For example, Santos et al. 2023 used a CNN to identify sunspots in spectroheliograms from the OGAUC. Chola et al. 2022 applied a DL approach to detect and classify sunspots in images from SDO/HMI and SoHO/MDI. Yang et al. 2018 implemented the simulated

annealing genetic method to segment the umbra and penumbra in SDO/HMI intensity images. Similar to this PhD work, they also compared their results with the HMI Debrecen sunspot Data (HMIDD) database from the DHO. Hanaoka 2022 developed an adaptive thresholding method using three different sources of white-light images and compared the resulting sunspot detections against manual records, finding similar levels of performance.

MM, in particular, is well-suited for sunspot extraction because it relies on simple yet efficient shape-oriented algorithms, as opposed to traditional intensity-oriented methods. The MM method's adaptability is enhanced through user interaction and parameter tuning, allowing it to handle various image types, resolutions, and stages of the solar activity cycle (from solar minimum to solar maximum), despite the significant impact of solar activity on intensity and sunspot area variations. MM can produce superior results compared to simple threshold-based detection techniques, as it considers the local environment and is less affected by uneven intensity variations. Additionally, MM offers a favourable balance between accuracy and efficiency. While techniques like DL may achieve higher accuracy or comparable performance, they are often more complex to implement. Once MM parameters are finely tuned, the method can effectively process images in an automated manner (see Section 2.4.1 for further advantages of MM over other image extraction techniques). Since the early 2000s, MM algorithms for automatic sunspot detection in full-disk continuum images have undergone significant improvements (e.g., Zharkov et al. 2005; Curto et al. 2008; Ling et al. 2020; Carvalho et al. 2020). For example, Stenning et al. 2013 leveraged MM algorithms for sunspot classification following the Mount Wilson Observatory criteria, while Hou et al. 2022 utilised MM for umbra/penumbra segmentation on manually drawn sunspot images.

3.2 Data description

In this chapter, we aimed to apply the MM algorithms introduced in Section 2.3 to photospheric observations for detecting sunspot contours. Our goal was to validate these algorithms through both qualitative and quantitative approaches. Qualitatively, we assessed the resulting contours through visual inspection. Quantitatively, we evaluated the accuracy of the MM method by comparing the detected sunspot areas with reference values.

3.2.1 Sunspot catalogues

Two reference sunspot catalogues were employed to compare and validate the results obtained from the MM method: the DHO and Mandal et al. 2020 catalogues.

DHO catalogue

The DHO database comprises a compilation of various solar catalogues that provide detailed information on the area and position of sunspots (Baranyi et al. 2016; Győri et al. 2017). These catalogues include data from ground-based observatories, such as the Debrecen Photoheliographic Data (DPD), which primarily comes from the Gyula and Debrecen observatories but also includes contributions from other observatories worldwide. The DPD is an extension of the Greenwich Photoheliographic Results (GPR) catalogue from the Royal Greenwich Observatory (RGO), which documented sunspot information from 1874 to 1976. Additionally, the DHO database includes data from space-borne observatories, such as the SDO/HMIDD and the SoHO/MDI Debrecen Data (SDD), which gather magnetic and white-light images from SDO/HMI and SoHO/MDI, respectively. In this study, we compared sunspot area values from the HMIDD database with those obtained using the MM sunspot contouring method. We also used the contrast-enhanced SDO/HMI images provided by the DHO to compare their manual detection method with the MM approach on identical data.

Mandal et al. 2020 catalogue

Another sunspot database compiled by Mandal et al. 2020 was used to further compare our sunspot area measurements. The Mandal et al. 2020 catalogue records sunspot data, including both projected and corrected sunspot areas as well as sunspot group areas, covering the period from 1874 to 2019. They cross-calibrated data from various observatories, extensively using data from the RGO as a basis, similar to the DHO catalogue, along with data from the DHO. Additionally, they incorporated data from seven other observatories: Kislovodsk, Pulkovo, Kodaikanal, the Solar Optical Observing Network (SOON), Rome, Catania, and Yunnan. This extensive cross-calibration allowed them to track systematic differences among these sunspot records and to inter-calibrate them,

providing a more reliable catalogue based on multiple databases.

3.2.2 Photospheric observations

Launched by NASA in February 2010, SDO is part of the "Living with a Star" mission (Pesnell et al. 2012). This mission aims to study the Sun's atmosphere and magnetic field, as well as its impact on space weather and the Earth's environment. Positioned in a geosynchronous orbit around Earth, SDO is equipped with three key instruments: AIA, HMI, and the Extreme ultraviolet Variability Experiment (EVE). AIA captures multi-wavelength images in the UV and EUV channels, covering the chromospheric and coronal regions with a 10-second cadence (Lemen et al. 2012). EVE measures the EUV flux across several spectral bands and provides solar irradiance data. Additionally, HMI delivers photospheric velocity measurements (dopplergrams) and data on the intensity and direction of the magnetic field through line-of-sight and vector magnetograms (Schou et al. 2012; Couvidat et al. 2016).

In this work, we utilised full-disk continuum intensity images from SDO/HMI (4096×4096 pixels) as they are well-suited for examining the detailed photospheric structure. Indeed, sunspots are prominently visible in these images as dark patches against the relatively smoother granulation network. To compare our sunspot area measurements with those from the DHO, we used contrast-enhanced versions of these images processed by the DHO. An example of such a contrast-enhanced SDO/HMI image, pre-processed by the DHO, is shown in Figure 3.1. These images cover the period from January 2012 to July 2014 with a 15-day cadence, capturing the peak of solar activity during Solar Cycle 24. This timeframe allowed us to track sunspot area variations during the rising phase and maximum of solar activity, when sunspot areas are at their largest. In total, MM operations were applied to 61 images, captured on the 1st and 15th of each month.

3.3 Algorithms

Once the dataset is gathered, the images must be prepared before applying the sunspot detection algorithms to ensure effective implementation and standardisation of the procedure.

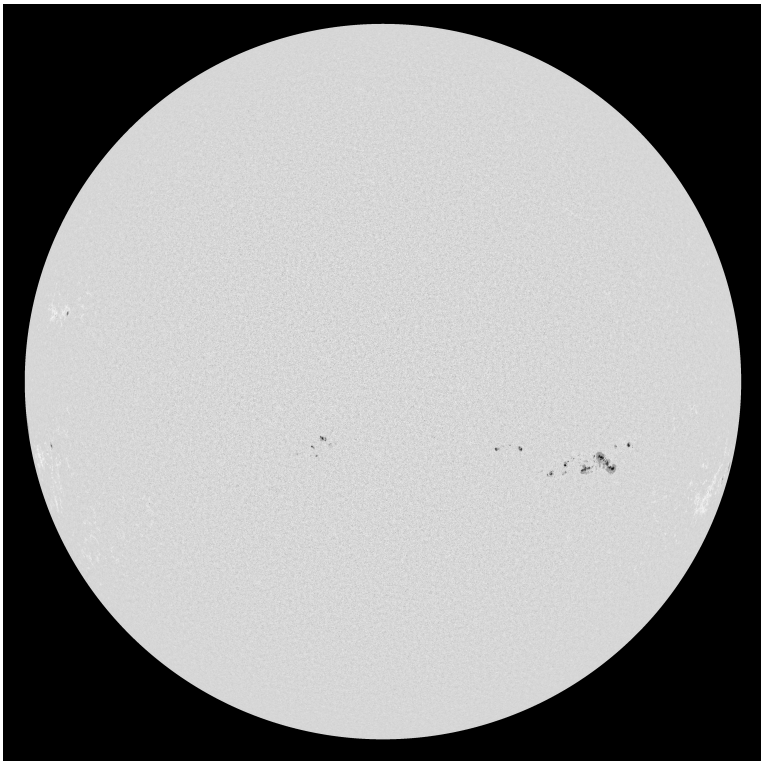

Figure 3.1: Full-disk continuum image captured by the HMI instrument aboard the SDO on January 1, 2014, and contrast-enhanced by the DHO. Source: Bourgeois et al. 2024a.

3.3.1 Preliminary data preparation

First, the image dimensions are reduced to 1024×1024 pixels to facilitate processing and to make them easily comparable to other images (e.g., from ground-based observatories). The resized images are then intensity-normalised, with pixel intensities adjusted so that the mean is set to 0 and the standard deviation to 1. However, the images are not yet ready for further processing. Some contrast-enhanced images exhibit surface imperfections at the solar limb, necessitating additional smoothing around the solar boundaries (see Figure 3.2(a)). To address this, a threshold of 10^{-4} is applied, followed by a fill-hole transformation to erase sunspots and achieve a fully white solar disk against the black background. This process ensures that the disk's edges will be evened out without altering the sunspot structures within. Next, an opening operation is performed using a disk-shaped structuring element with a size of 300 pixels. The disk shape is chosen to avoid distorting the solar disk. In all subsequent

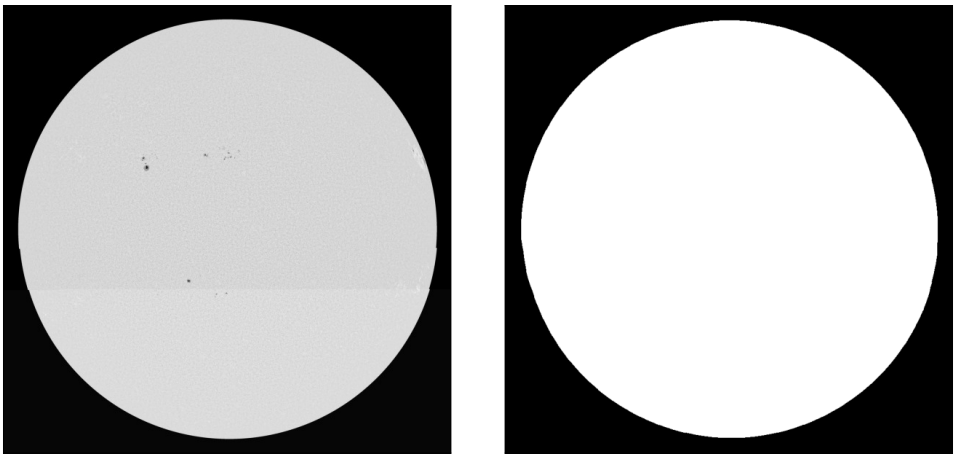

(a) Asperities at the solar limb may appear in the contrast-enhanced SDO/HMI continuum images, as shown in this example (note the irregularities on the left and right edges of the Sun). These irregularities can hinder the performance of the subsequent MM algorithms, as these algorithms are very sensitive to sharp edges and discontinuities in shape.

(b) Label of the Sun after pre-processing Figure 3.2(a), which includes edge smoothing through opening and erosion operations with a disk-shaped structuring element. The image is also resized, normalised, and the solar radius is set to a reference value to standardise the application of MM algorithms for sunspot detection.

Figure 3.2: Pre-processing of the original images to even out the borders at the solar limb, ensuring the effective application of following detection algorithms. Source: Bourgeois et al. 2024a.

MM operations carried out in this chapter, a disk-shaped SE is used because sunspots are isotropic features and thus are best captured with an isotropic SE. Following the opening, an erosion transform is applied with a disk-shaped SE of 5 pixels. These two operations smooth out the borders (see Figure 3.2(b)). Finally, the solar radius is adjusted to a reference value of 450 pixels, as was done in Barata et al. 2018. This value, proven effective in their study, was deemed suitable for standardising the images and applying the sunspot detection algorithms used in this work.

3.3.2 Processing and identification

The sunspot extraction algorithm can now be applied to the photospheric images that were pre-processed as described in the previous subsection. The first step involves enhancing the sunspots against the background to facilitate their extraction (see Figure 3.3(a)). This is achieved using the black top-hat

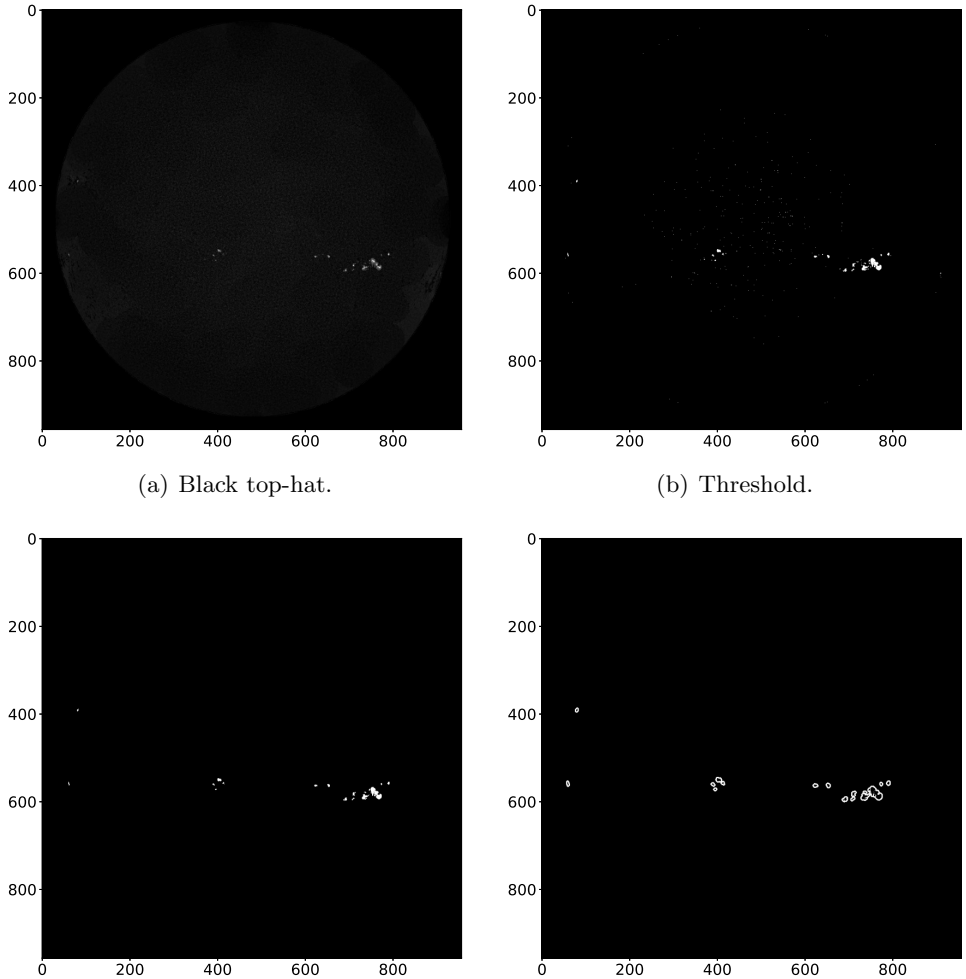

(a) Black top-hat.

(b) Threshold.

(c) Opening by reconstruction.

(d) External gradient.

Figure 3.3: The different steps of the MM sunspot detection algorithm applied to the pre-processed SDO/HMI full-disk image displayed in Figure 3.1. Source: Bourgeois et al. 2024a.

operation, which is ideal for extracting small dark features smaller than the SE (refer to Section 2.3.6 for a detailed explanation of this operator). In this case, an SE size of 70 pixels is chosen. If the SE is too small, the black top-hat operation will not fully recover larger sunspots. Conversely, an excessively large SE would merge sunspots with darker granules around them, although this effect is mitigated by applying a fixed threshold in the subsequent step. The threshold is set to 0.33, resulting in the binary image shown in Figure 3.3(b).

Next, an opening by reconstruction with an SE size of 2.00001 is performed on the thresholded image (Figure 3.3(c)) to remove small noise while preserving the main structures, i.e., the sunspots (see Subsection 2.3.3 for a description of this operator). Finally, the contours of the sunspots are recovered by applying the external gradient to the opened image (see Subsection 2.3.5), as shown in Figure 3.3(d). The external gradient is preferred over the classic morphological gradient to thin the contours and obtain the outer edges of the sunspots. For illustration, Figure 3.4 shows the sunspot contours outlined in red on the original contrast-enhanced image from Figure 3.1. The algorithm successfully delineates the penumbrae boundaries of the sunspots. All resulting sunspot-contoured images were visually inspected and validated, providing satisfactory qualitative detection.

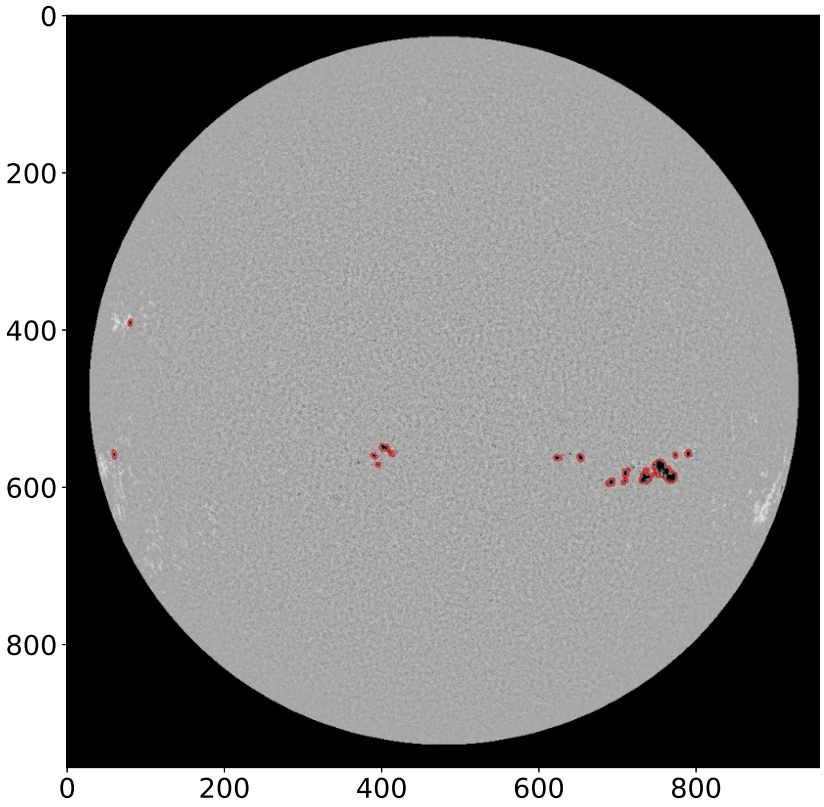

Figure 3.4: Sunspot contours obtained using the MM algorithm described in Figure 3.3, overlaid in red on the original image shown in Figure 3.1. Source: Bourgeois et al. 2024a.

3.4 Evaluation against manual methods

After delineating the sunspot contours using the MM algorithms described in Section 3.3, we measured the areas within each sunspot and summed them across each image in the dataset. We recall that the dataset spans two and a half years, from January 2012 to July 2014, with a 15-day cadence. The resulting total sunspot areas are the projected areas, calculated directly from the sunspot surfaces observed in the images. However, these images are subject to the foreshortening effect, which distorts solar features near the limb. Indeed, some sunspots may appear compressed, elongated, or smaller around the solar limb due to the viewing angle of the SDO satellite. Additionally, sunspots near the limb are less distinct because of the increased length of the light path through the solar atmosphere at this angle, which may lead to more light scattering and absorption, reducing brightness at the Sun's edges. To account for this effect, the corrected sunspot areas were calculated by considering the Sun's curvature and the angle of observation. In this study, we compared both the projected and corrected sunspot area values with those found in the sunspot catalogues mentioned above (see Subsection 3.2.1).

3.4.1 Projected sunspot area measurements

Before evaluating the impact of the foreshortening effect on the performance of the MM sunspot detection method, we first compare the projected sunspot areas obtained with this method to the manual data collected by the DHO and Mandal et al. 2020. Figure 3.5 displays the total summed sunspot area per day over the study period, as provided by the DHO (blue triangles), Mandal et al. 2020 (green dots), and the MM method (red crosses). Notably, the Mandal et al. 2020 data often show larger sunspot areas, likely due to their rigorous cross-calibration of data from various observatories, which minimises errors and reduces the likelihood of missing small sunspot areas.

As the solar cycle progresses towards its maximum (reached in April 2014), the total sunspot area increases significantly, which is expected. However, this growth includes not only the expansion of large sunspots but also the appearance of numerous smaller spots around them. While Mandal et al. 2020 reports the projected areas of these smaller spots with high precision, the DHO and MM methods tend to slightly underestimate the total sunspot area.

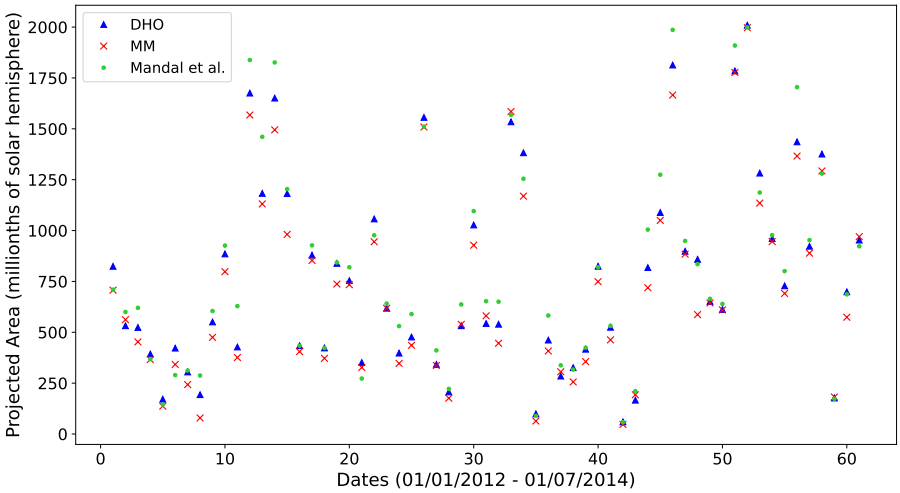

Figure 3.5: Projected total sunspot area per day between 01/01/2012 and 01/07/2014, recorded with a 15-day cadence by the DHO (blue triangles), Mandal et al. 2020 (green dots), and using the labels obtained with the MM method (red crosses). Source: Bourgeois et al. 2024a.

Correlation coefficient	**Corrected areas**	**Projected areas**
MM/DHO	0.91	0.95
MM/Mandal et al.	0.88	0.96
DHO/Mandal et al.	0.93	0.97

Table 3.1: Comparison of correlation coefficients between the MM, DHO, and Mandal et al. 2020 datasets for projected and corrected sunspot areas.

The MM method, in particular, often reports smaller sunspot areas due to the inherent design of the MM algorithms, which prioritise the extraction of medium- and large-sized sunspots and may exclude very small spots or pores that could be mistaken for dark noise on the solar disk. Despite these minor discrepancies, all three catalogues exhibit a similar overall trend, with only slight and nearly systematic variations. These differences are anticipated given the different recording conditions and objectives: the DHO aims for consistent long-term data, Mandal et al. 2020 focuses on precision through inter-calibration, and the MM approach emphasises efficiency and automation.

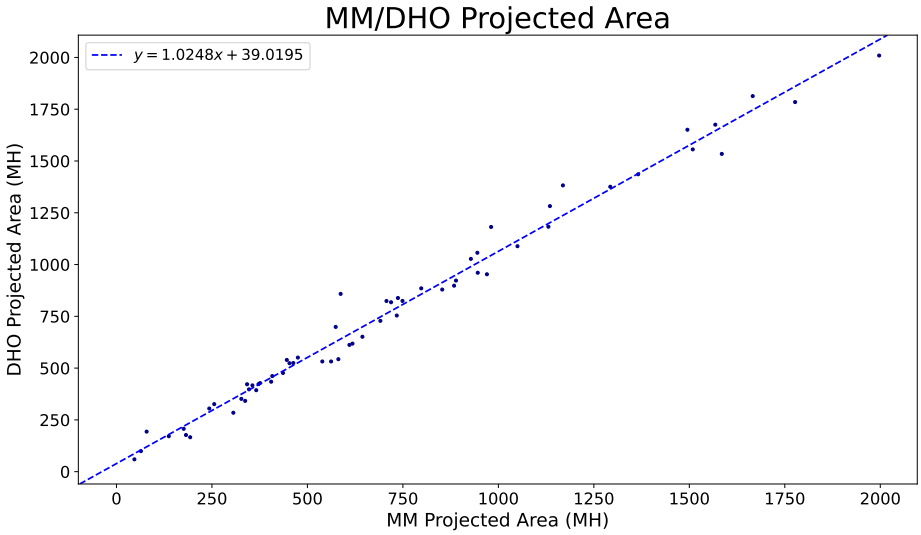

(a) Correlation of projected sunspot areas between the DHO catalogue and the MM approach.

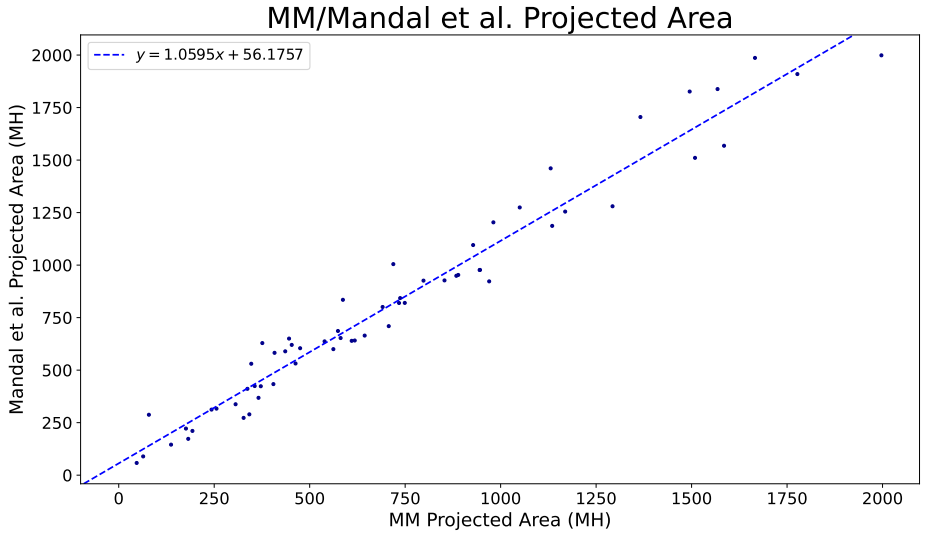

(b) Correlation of projected sunspot areas between the Mandal et al. 2020 catalogue and the MM approach.

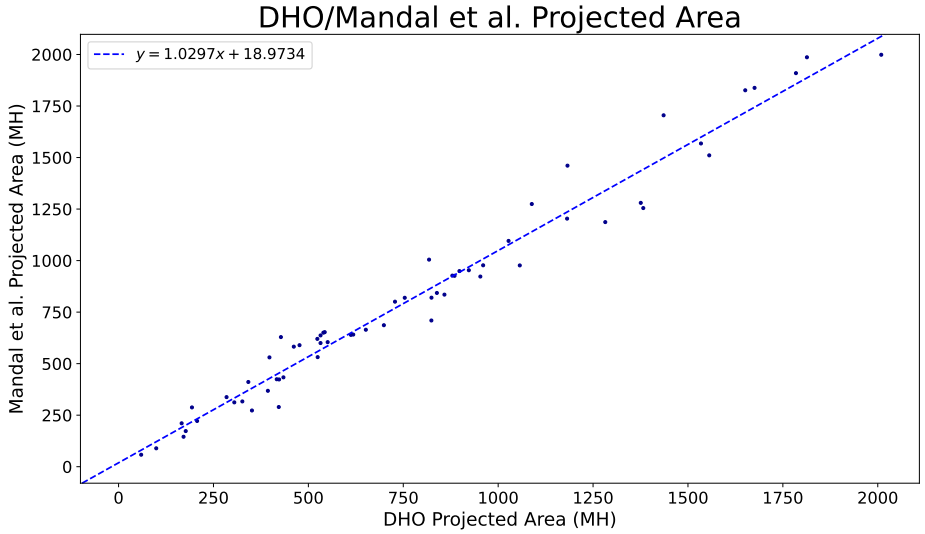

(c) Correlation of projected sunspot areas between the two reference catalogues: DHO and Mandal et al. 2020.

Figure 3.6: Correlation of the total projected sunspot area per day from January 1, 2012, to July 1, 2014 (with a 15-day cadence) as recorded in the DHO and Mandal et al. 2020 catalogues, compared with values obtained using the MM sunspot contouring method. Source: Bourgeois et al. 2024a.

To compare the methods more accurately, we present linear fits in Figure 3.6. Panel 3.6(a) illustrates the linear fit between the DHO and MM data, panel 3.6(b) shows the fit between the Mandal et al. 2020 and MM data, and panel 3.6(c) depicts the fit between the DHO and Mandal et al. 2020 data. The correlation coefficients for these fits are summarised in the last column of Table 3.1. The strongest correlation is observed between the two reference datasets, DHO and Mandal et al. 2020, with a coefficient of 0.97. The linear fits between MM and DHO data, as well as those between MM and Mandal et al. 2020 data, also show very good correlations, with coefficients of 0.95 and 0.96, respectively. Notably, panel 3.6(b) reveals a larger dispersion between the MM and Mandal et al. 2020 data at wider sunspot area values (above 1000 millionths of the solar hemisphere), although the overall correlation remains high.

3.4.2 Corrected sunspot area measurements

As discussed in the introduction of this section, the foreshortening effect can significantly impact solar features near the limb, particularly in the measure-

ment of their areas, which may be distorted and underestimated. We now aim to correct this effect and examine its consequences on the performance of the MM algorithms used for sunspot detection. The sunspot areas corrected for the foreshortening effect (A_{corr}) are calculated by dividing the projected sunspot areas (A_{proj}) by a correction factor d, as described in Equation 3.1: $A_{corr} = A_{proj}/d$. The correction factor d corresponds to the cosine of the angular distance between the solar centre and the sunspots.

$$d = \sin(B_0) \times \sin(B) + \cos(B_0) \times \cos(B) \times \cos(L_0 - L). \tag{3.1}$$

This correction factor requires the heliographic latitude (B_0) and longitude (L_0) of the solar centre (provided by the DHO database), as well as the sunspots' centre coordinates in heliographic coordinates (latitude B and longitude L). The values of B and L are calculated using Equations 3.2 and 3.3, respectively, based on the pixel coordinates of the sunspots' centroids (x_s and y_s) and the pixel coordinates of the solar centre (x_c and y_c). Here, P represents the solar north pole angle (also provided by the DHO database; for example, $P = 0.07°$ on 01/01/2014), while ρ and θ are given by Equations 3.4 and 3.5.

$$B = \arcsin[sin(B_0) \times cos(\rho) + cos(B_0) \times sin(\rho) \times cos(P - \theta)] \tag{3.2}$$

$$L = \arcsin[\frac{1}{cos(B)} \times sin(\rho) \times sin(P - \theta)] \tag{3.3}$$

In Equation 3.4 (calculation of ρ), R is the distance between the solar centre and the sunspots' centroids in pixels (Equation 3.6), R_{sun} is the solar radius in pixels ($R_{sun} = 450$), and d_{app} is the apparent diameter of the Sun, which varies slightly during the year due to the elliptical orbit of the Earth around the Sun, but is fixed here to its average value of 0.5° for simplicity.

$$\rho = \arcsin(\frac{R}{R_{sun}}) - \frac{d_{app}}{2} \times \frac{R}{R_{sun}} \tag{3.4}$$

$$\theta = \arctan \frac{x_s - x_c}{y_s - y_c} \tag{3.5}$$

$$R = \sqrt{(x_s - x_c)^2 + (y_s - y_c)^2} \tag{3.6}$$

The corrected sunspot areas are then compared with values recorded by

the two reference catalogues, DHO and Mandal et al. 2020, and are displayed with red crosses in Figure 3.7. For comparison, the corrected sunspot areas from the DHO and Mandal et al. 2020 catalogues are shown in blue and green, respectively. Similar to the projected areas, the MM approach slightly underestimates the corrected sunspot areas on some days compared to the reference catalogues, but overall, all three sunspot records exhibit a similar trend.

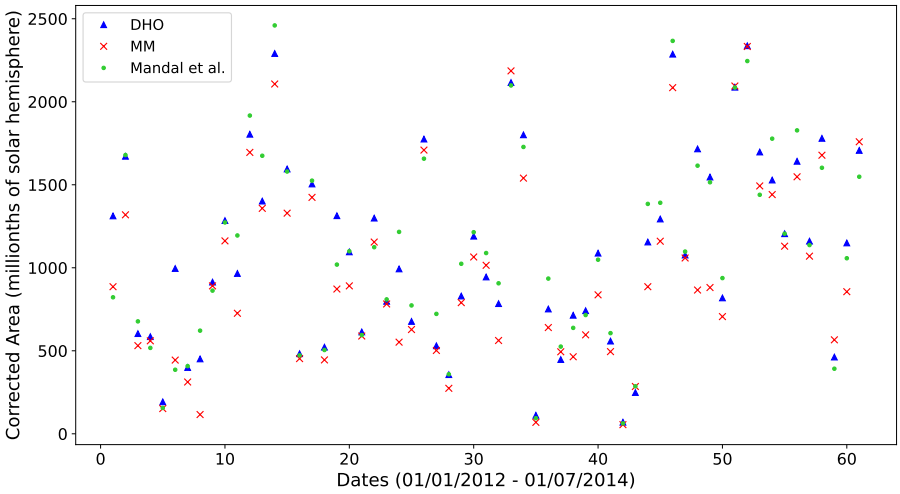

Figure 3.7: Corrected total sunspot area per day (adjusted for the foreshortening effect) from 01/01/2012 to 01/07/2014, recorded with a 15-day cadence by the DHO (blue triangles), Mandal et al. 2020 (green dots), and using the labels obtained with the MM method (red crosses). Source: Bourgeois et al. 2024a.

To evaluate the correlation between methods more precisely, linear fits are provided in Figure 3.8. The correlation coefficients for these fits are summarised in the middle column of Table 3.1, showing generally lower correlations for corrected sunspot areas compared to projected areas. Specifically, the correlation coefficient between the DHO and Mandal et al. 2020 catalogues is 0.93 for corrected sunspot areas, compared to 0.97 for projected areas. This discrepancy arises from differences in how each catalogue performs the correction.

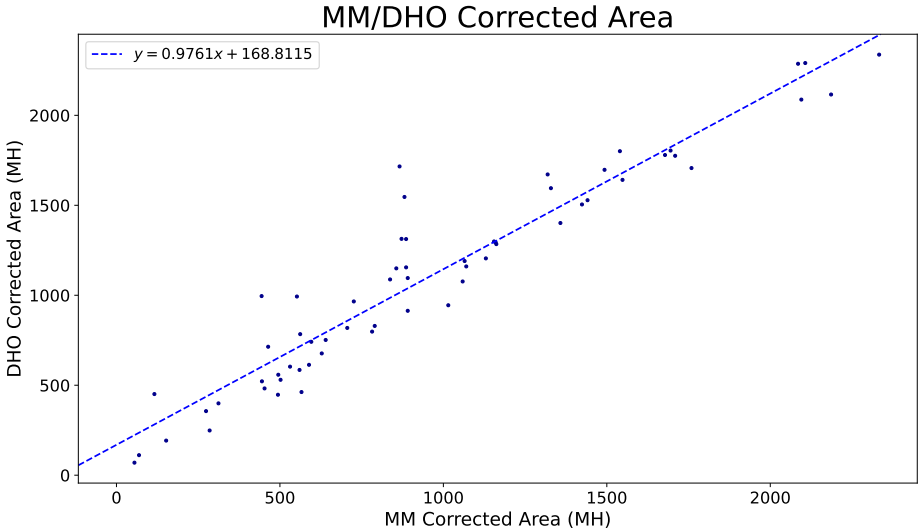

(a) Correlation of corrected sunspot areas between the DHO catalogue and the MM approach.

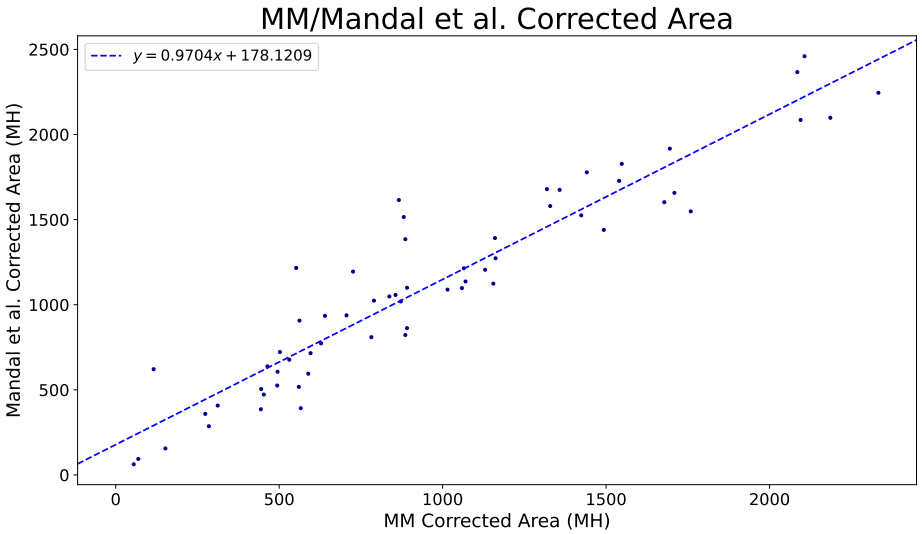

(b) Correlation of corrected sunspot areas between the Mandal et al. 2020 catalogue and the MM approach.

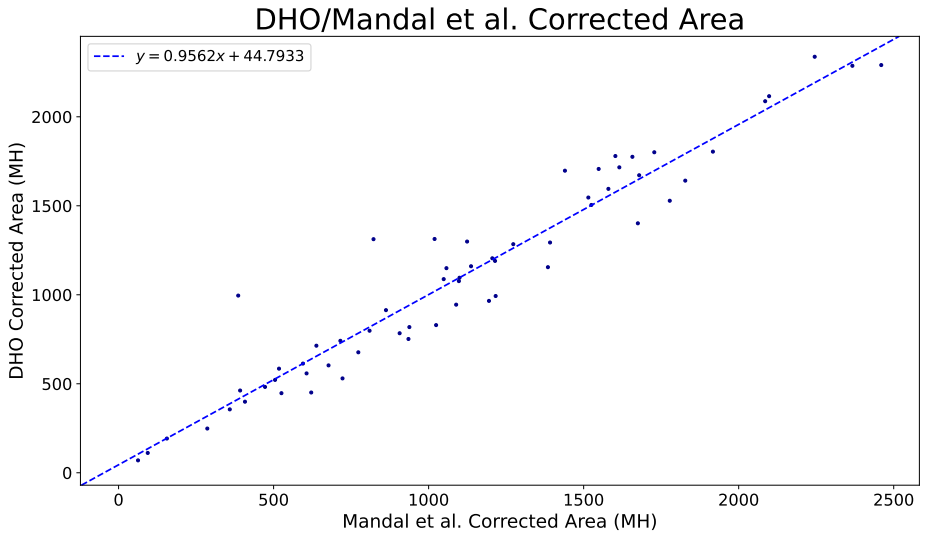

(c) Correlation of corrected sunspot areas between the two reference catalogues: DHO and Mandal et al. 2020.

Figure 3.8: Correlation of the total corrected sunspot area per day from January 1, 2012, to July 1, 2014 (with a 15-day cadence) as recorded in the DHO and Mandal et al. 2020 catalogues, compared with values obtained using the MM sunspot contouring method. Source: Bourgeois et al. 2024a.

The correlation coefficient for the linear fit between the DHO and MM data is 0.91, while the fit between Mandal et al. 2020 and MM data shows the lowest correlation, at 0.88. This slight dispersion appears in Figure 3.8(b), where discrepancies between the MM sunspot areas and the Mandal et al. 2020 catalogue are more visible. Notably, both panels 3.8(a) and 3.8(b) show aligned vertical points around 900 millionths of the solar hemisphere (MH), indicating that the MM method significantly underestimates corrected sunspot areas on these dates compared to both reference catalogues. This pattern does not appear in panel 3.8(c), which compares the two reference catalogues, nor in panels 3.6(a) and 3.6(b), which display projected areas. This suggests that the MM method is likely missing a few sunspot areas near the solar limb.

Although the MM method is less affected by the limb darkening effect compared to simpler thresholding methods, it remains susceptible to local intensity variations on scales smaller than the structuring element used in the black top-hat operation. As a result, some small and faint sunspots near the solar limb may be missed by the MM sunspot detection algorithm. While the MM parameters were fine-tuned to align with visual inspection expectations,

some small spots might still be overlooked visually and, therefore, by the algorithm. This suggests that further visual checking and refinement of the structuring elements could improve the detection of such sunspots. However, it is important to note that perfectly fine-tuning the parameters of an algorithm designed for automatic application across a vast dataset, while ensuring accurate sunspot detection, remains a challenging task.

Nevertheless, the correlation coefficients and curves presented in Figure 3.8 demonstrate a strong agreement among all methods, including the MM results and the cross-calibrated data from Mandal et al. 2020, with respect to corrected sunspot areas.

3.5 Conclusion

In this study, we validated the MM algorithms used for sunspot detection both qualitatively, through visual inspection, and quantitatively, by comparing the measured sunspot areas with those from two reference catalogues. Despite some minor differences in the corrected sunspot area records — including between the two reference catalogues — the overall correlation among all three methods is high. This strong correlation underscores the effectiveness of the MM method for sunspot detection, which proves particularly valuable for automatically processing extensive volumes of satellite image data, thereby aiding in long-term solar activity monitoring and forecasting. Furthermore, these algorithms can be adapted to other contexts, such as extracting more complex features like magnetic flux ropes (discussed in Chapter 4) and coronal off-limb structures (discussed in Chapter 5), as well as for applications involving different resolutions and image types, including simulation data (see Chapter 4).

Chapter 4

Simulation data-based magnetic flux rope extraction

This chapter outlines the analysis and extraction method for magnetic flux ropes (MFRs) as detailed in Wagner et al. 2023b and applied in Wagner et al. 2024a; Wagner et al. 2024b. MFRs are coherent structures in the Sun's corona characterised by magnetic field lines that twist around a central axis, forming a rope-like configuration. This distinguishes them from simple magnetic flux tubes, which feature straight, parallel field lines. The field lines in MFRs are typically anchored at both ends, preserving the structure's integrity and the plasma contained within it. MFRs form through processes such as shearing motions and magnetic reconnection, where magnetic field lines break, twist, and reconnect. While these structures can remain stable for extended periods, they may eventually lose stability and trigger eruptions. MFRs are closely associated with the development of filaments and prominences, particularly when filled with dense plasma, and they play a key role in CMEs (Vourlidas et al. 2013; Green et al. 2018). When MFRs become unstable, they can erupt, contributing to a CME that extends into interplanetary space. In coronagraph images, MFRs are often observed as the bright core of a three-part CME morphology, surrounded by a dark cavity and a leading edge (see Figure 4.1). Understanding the behaviour of MFRs, from their formation to their eventual eruption, is therefore fundamental for accurate space weather forecasting.

However, directly observing MFR structures and the magnetic field in the coronal region is challenging (Kilpua et al. 2019). The corona is a highly dynamic and complex environment, significantly hotter and less dense than the

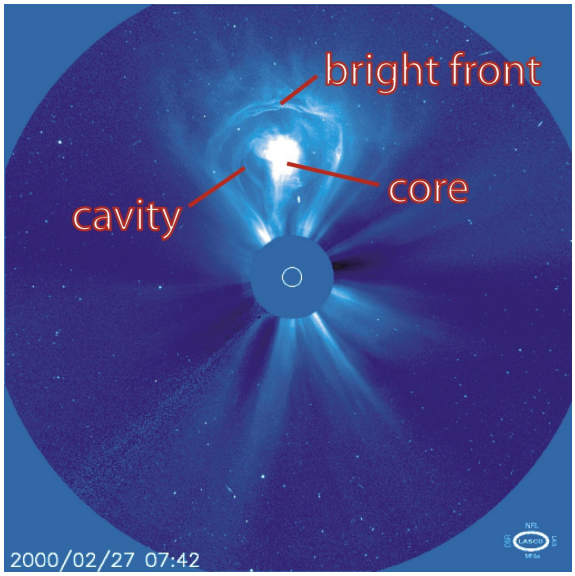

Figure 4.1: CME exhibiting a three-part morphology, consisting of a bright leading front surrounding a cavity and a bright core, which is often associated with an MFR configuration. This white-light image was recorded by the Solar and Heliospheric Observatory (SoHO)/Large Angle and Spectrometric Coronagraph (LASCO) on February 27, 2000. Source: Riley et al. 2008.

photosphere. Due to thermal effects, coronal spectral lines are often too faint for effective measurement. In contrast, absorption lines in the photosphere are generally stronger and well-defined, allowing for direct magnetic field measurements through the Zeeman effect, where the magnetic field causes the splitting of atomic energy levels. Analysing these split lines, such as those of iron, is an efficient way to map the magnetic field's direction and intensity at the photospheric level. The magnetic field in the corona is typically calculated through data-driven modelling, using extrapolation from photospheric magnetic data (Mackay et al. 2011; Cheung et al. 2012; Pomoell et al. 2019; Price et al. 2019; Wagner et al. 2023a; Wagner et al. 2023b). In this chapter, a coronal model is utilised to generate twist number maps that outline the cross-sections of MFRs and allow their evolution to be tracked over time. We then use MM algorithms to extract these structures, improving upon the previous extraction method developed by Wagner et al. 2023a. This approach facilitates a detailed study of MFR evolution, including their propagation, cross-sectional circularity, and insights into their eventual eruption (or failed eruption).

4.1 Data acquisition

The MFRs of two active regions (ARs) are studied: AR 12473 and AR 11176. AR 12473 is examined over a period from 22 December 2015, 23:36 UT to 2 January 2016, 12:36 UT, and AR 11176 from 25 March 2011, 04:00 UT to 1 April 2011, 18:00 UT, both with a six-hour cadence. This time span is chosen to ensure that the two active regions of interest are located close to the solar centre, minimising projection effects. For these two ARs, a time-dependent data-driven magnetofrictional model (TMFM) is used to produce twist number maps from electric field maps derived from SDO/HMI vector magnetogram observations (Lumme et al. 2017; Pomoell et al. 2019). The twist number, as defined by Berger et al. 2006 and Liu et al. 2016, measures how many times two infinitesimally close field lines within the MFR wind around each other. The twist number maps capture the twist within the MFR cross-sections, corresponding to the two-dimensional vertical slices of the ARs near their polarity inversion line (PIL) during the simulation. These maps have a resolution of 0.36 Mm per pixel. The twist number maps for AR 12473 and AR 11176 are provided in Figures 4.2 and 4.3, respectively. Equation 4.1 describes the principle underlying the TMFM, namely, that the plasma velocity $\mathbf{v}$ is proportional to the Lorentz force $\mathbf{J} \times \mathbf{B}$ and inversely proportional to the magnetofrictional coefficient ν (Yang et al. 1986; Pomoell et al. 2019). μ_0 is the magnetic permeability of vacuum.

$$\mathbf{v} = \frac{1}{\nu} \frac{\mu_0 \mathbf{J} \times \mathbf{B}}{B^2} \tag{4.1}$$

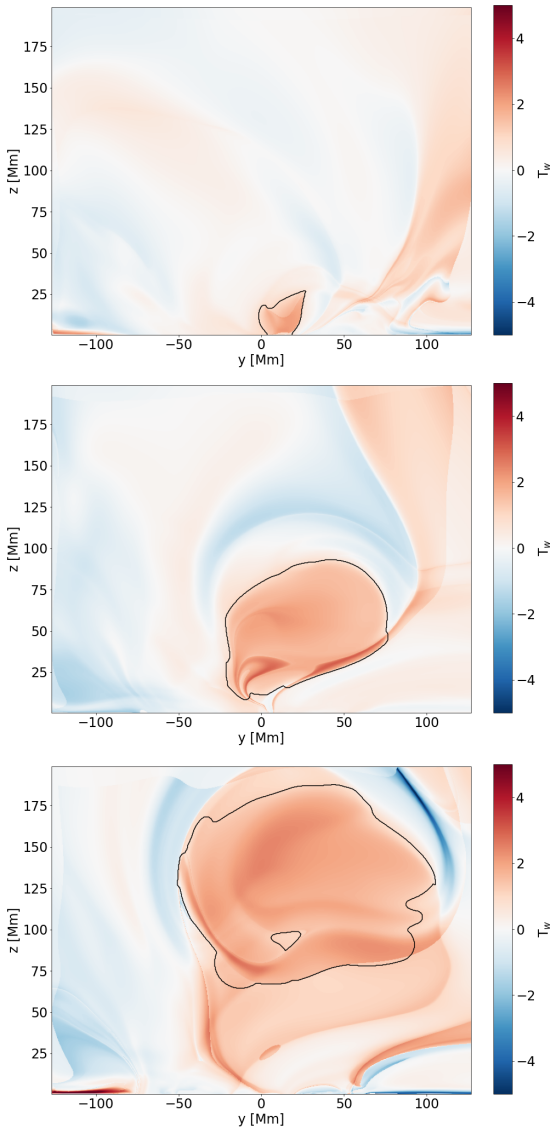

Figure 4.2: Twist number maps for AR 12473 at frame 7 (top row), frame 17 (middle row), and frame 27 (bottom row), representing early, middle, and final stages, respectively. Higher twist values are indicated by more intense colours, with positive twist numbers in red and negative in blue. The thin black outline traces the MFR cross-section in each frame, illustrating its evolution over time. Source: Wagner et al. 2023b.

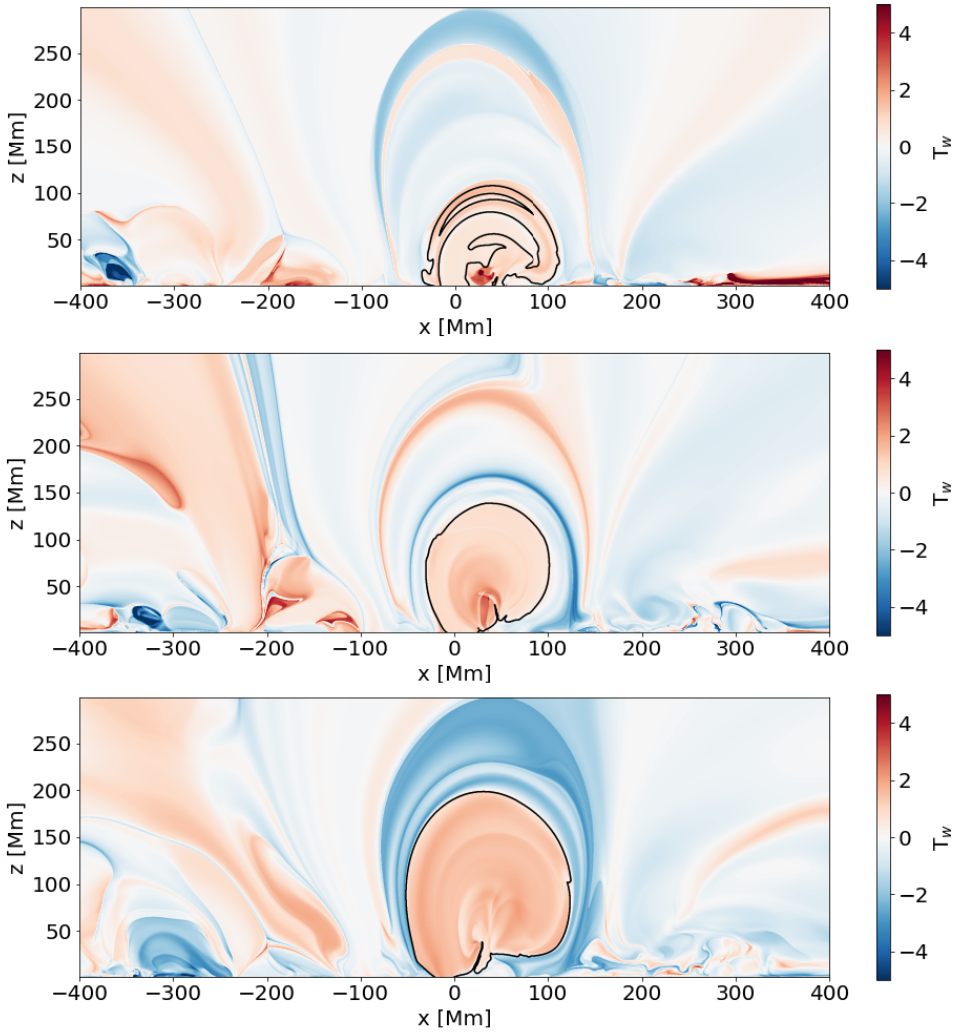

Figure 4.3: Twist number maps for AR 11176 at frame 8 (top row), frame 18 (middle row), and frame 28 (bottom row), representing early, middle, and final stages, respectively. As in Figure 4.2, higher twist values are indicated by more intense colours, with positive twist numbers in red and negative in blue, while the thin black outline traces the MFR contours in each frame. Source: Wagner et al. 2023b.

4.2 Extraction technique

For both AR 12473 and AR 11176, the MFR structure is identified across all frames in the time series using an improved methodology that expands on the one developed by Wagner et al. 2023a, employing mathematical morphology operations. The method in Wagner et al. 2023a required several parameters, e.g., based on the gradient within the twist number maps and the extent of twisted magnetic field lines overlying but not part of the MFR structure. It also assumed that the MFR cross-sections in the twist maps were perfectly circular — a limitation that can be problematic, as will be discussed in Sections 4.3.1 and 4.4. The new method presented in Wagner et al. 2023b, however, does not rely on such parameters or assumptions. Instead, a morphological gradient is directly applied to the twist number maps. This gradient is multi-scale, utilising two structuring elements: one to detect smaller and localised boundaries between highly twisted and less twisted regions, and another for broader transitions. The SEs are selected to be circular, corresponding to the roughly circular shape of the MFR structures, with sizes between 4 and 10 pixels. Clear visual outcomes are achieved by employing a smaller SE of size 5 and a larger one of size 10.

The output images resulting from the gradient operation are then combined with the original twist number maps. A fixed threshold is applied, producing binary masks that highlight the MFR structures in the foreground. The prior application of the multi-scale gradient allows the thresholding process to effectively capture the highly twisted MFR regions while avoiding low-twist areas and minimising the extraction of artifacts or high-twist regions that do not belong to the MFR structure. If necessary, post-processing may be carried out using a morphological opening operation. During visual inspection, any remaining structures in the masks that are not part of the flux rope (despite being highly twisted) must be removed. This post-processing is selectively applied to specific frames. In those requiring it, openings with small SEs may be applied to the entire image, while larger SEs are employed more selectively on certain parts of the image to avoid distorting the overall MFR shape, as larger SEs can smooth edges and disconnect structures (as discussed in Section 2.3.3). To preserve the integrity of the MFR structure, small SEs are initially used, with their size gradually increased if needed.

In this opening operation, the SEs are again selected to be circular to

prevent distortion of the flux rope structures, with their size adjusted according to the simulation stage and the scale and nature of the structures to be removed (e.g., small noise versus large connected structures). For instance, in AR 12473, the SE for the morphological opening operation ranges from 10 to 50 pixels in the early stages of the simulation, whereas in the later stages, sizes exceeding 100 pixels are used to remove larger structures. An example is illustrated in Figure 4.8: panel b) shows the original twist number map of frame 16 (corresponding to the middle stage of the simulation), panels d) and f) display the combination of this twist map with the multi-scale gradient operation using larger and smaller SEs, respectively, and panel g) presents the binary mask after thresholding at a value of 0.8. Panel h) demonstrates the post-processing applied to the binary mask from panel g): initially, an opening operation with a small SE is performed across the entire frame, removing small connections at the bottom of the MFR structure around [y, z] = [0 Mm, 10 Mm]. Subsequently, a second opening operation with a larger SE is conducted to remove a highly twisted filamentary structure connected to the MFR shape at approximately [y, z] = [75 Mm, 50 Mm]. In the case of AR 11176, SE sizes are typically chosen around 10 pixels, as the flux rope in this active region is more stable and is initially well-captured by the gradient operation due to its clearly defined twist boundaries.

The MFR extraction resulting from this post-processing is verified through visual inspection. If the results are deemed satisfactory, a tracking procedure, as described by Wagner et al. 2023a, is implemented to extract the MFR in each frame. Following tracking, additional erosion or dilation operations may be applied to further refine the shape. Specifically, dilation can be used to fill any gaps within the extracted MFR structures, though this extra step is often unnecessary. The source points of the structures are then computed with a uniform distribution and input into visualisation software (e.g., VisIt) to track the evolution of the magnetic field lines and footpoints of the MFRs. The right panel of Figure 4.4 displays three examples of the magnetic field lines resulting from the flux rope MM-based extraction technique for AR 12473 at frames 7, 17, and 27. In contrast, the left panel shows the MFR field lines obtained using the previous method developed by Wagner et al. 2023a. This figure illustrates the evolution of the MFR structure from an early stage to a stage near the end of the simulation. It demonstrates how the MFR lifts and spreads through the simulation domain, highlighting two main sub-structures represented by

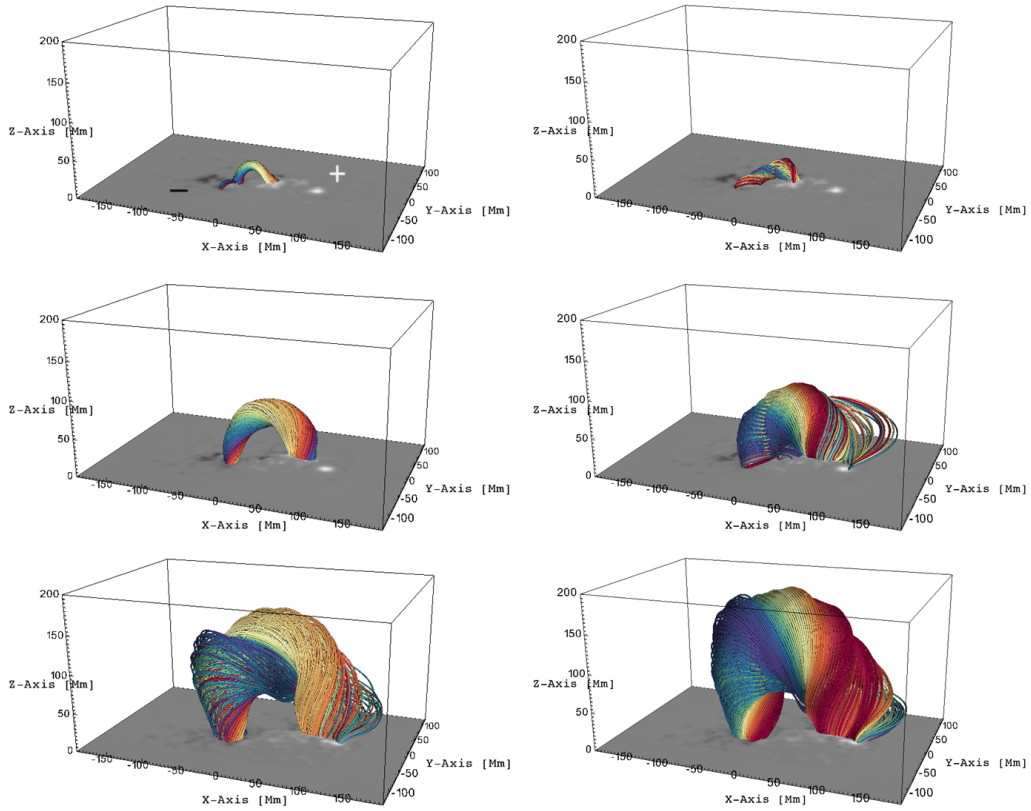

Figure 4.4: Visualisation of the MFR field lines in AR 12473 at frames 7, 17, and 27. The magnetic polarities at the MFR footpoints are indicated in black (negative polarity) and white (positive polarity). The left panel shows the magnetic field lines obtained from the MFR extraction using twist number maps, as performed in Wagner et al. 2023a. The right panel presents the magnetic field lines resulting from the MFR extraction procedure described in Section 4.2, which applies MM algorithms such as the morphological gradient and opening to the same twist number maps. The MFR structure appears highly dynamic and rises rapidly over time within the simulation domain, suggesting that this MFR may be eruptive. Source: Wagner et al. 2023b.

the red/beige and blue lines. Figure 4.4 contrasts the MM method with the previous approach, particularly in terms of bulkiness and consistency, which will be further examined in Section 4.4.

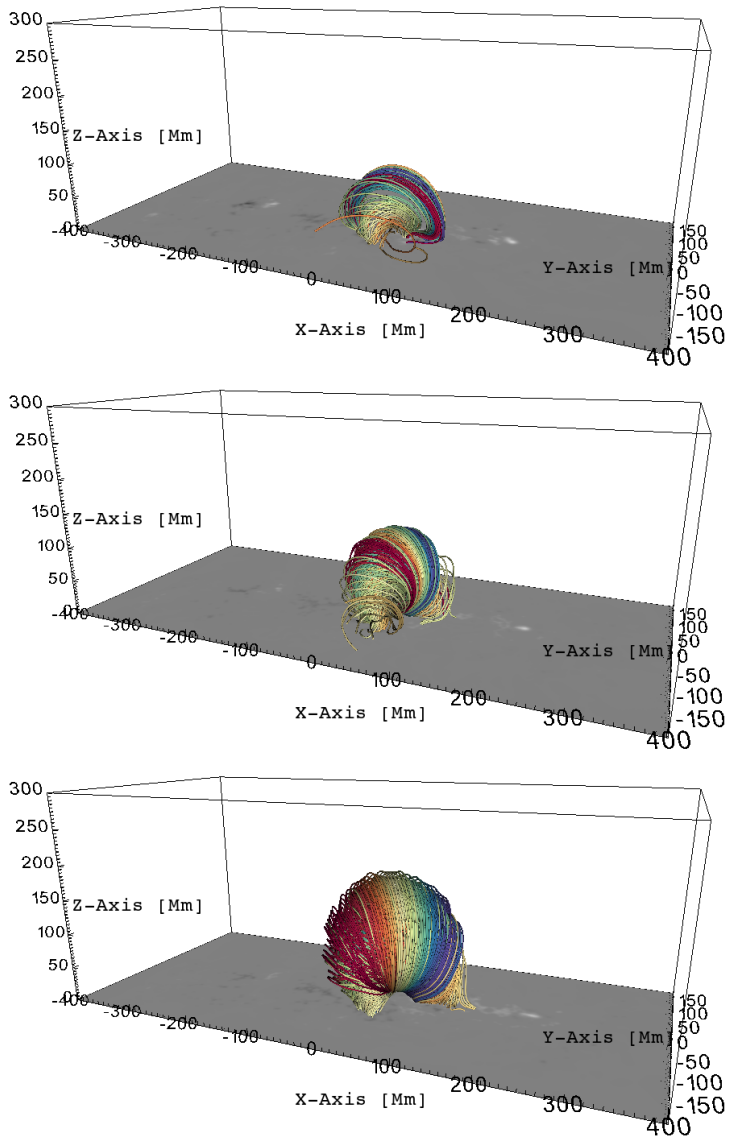

Figure 4.5: Visualisation of the MFR field lines in AR 11176 at frames 8, 18, and 28. The field lines are derived from MFR extraction based on twist number maps using the MM approach (see Section 4.2). As in Figure 4.4, black on the magnetogram at the MFR footpoints represents negative magnetic polarity, while white indicates positive polarity. The MFR is clearly composed of a tightly twisted core and a surrounding larger, less-twisted envelope. The MFR's expansion appears consistent and regular, with its overall shape remaining stable over time, suggesting that this MFR is unlikely to erupt. Source: Wagner et al. 2023b.

Similarly to Figure 4.4, Figure 4.5 depicts the evolution of the MFR field lines extracted using the MM-based methodology for AR 11176 at frames 8, 18, and 28. The MFR structure consists of two main sub-structures that expand over time: a twisted core of toroidal field lines at lower coronal heights (around 10 Mm) and a large, less-twisted envelope that extends up to 200 Mm in the final stages (as shown in the bottom frame of Figure 4.5). The magnetic field lines forming this envelope, while anchored to the same MFR footpoints as the core sub-structure, resemble poloidal field lines. Figures 4.4 and Figure 4.5 illustrate the significant differences in how the MFR structures develop throughout the simulation domain in both active regions. The MFR in AR 11176 (Figure 4.5) emerges at higher heights (around 100 Mm), is more stable, and expands rather than rising quickly. In contrast, the MFR in AR 12473 (Figure 4.4) appears at lower heights (around 50 Mm), is more dynamic, and ascends more rapidly. Building on these visual observations across the entire time series for both AR 12473 and AR 11176, we will further analyse the cross-sectional circularity and propagation of the MFRs in the following section.

4.3 Flux ropes properties

The extracted MFR field lines from the simulation-generated twist number maps in both ARs were compared against observations. We recall that the simulation for AR 12473 spans the period from 22 December 2015, 23:36 UT, to 2 January 2016, 12:36 UT, with a cadence of six hours. During this period, a M1.9 solar flare, recorded by GOES, erupted on 28 December 2015 (see Wagner et al. 2023a), which aligns with the dynamics of the modelled MFR, suggesting it is an eruptive structure. For AR 11176, the simulation covers the period from 25 March 2011, 04:00 UT, to 1 April 2011, 18:00 UT. Although an eruption occurred near this period, it took place after the simulation ended, on 3 April 2011. This eruption was not modelled because the AR was approaching the solar limb, which had to be avoided to correctly apply the TMFM based on magnetogram data. However, a large solar filament was visible on the same period and later appeared as a suspended prominence at the solar limb against the dark outer space on 5 April 2011. It is notable that this filament, which converted into a prominence during the Sun's rotation, elevated in the corona by around 10 Mm, roughly corresponding to the height of the twisted core

sub-structure forming the extracted MFR in AR 11176. Thus, both modelled outcomes appear to correspond well with the observed phenomena, including a powerful eruption with an M1.9 flare in AR 12473 and a large, confined filament/prominence structure near the PIL in AR 11176. These observations corroborate the assumptions derived from the analysis of the modelled MFR evolution, suggesting an eruptive nature for the MFR in AR 12473 and a confined nature for the MFR in AR 11176. The MFRs indeed exhibit distinct behaviours, as will be discussed in Section 4.3.2.

4.3.1 Cross-sectional circularity

The circularity parameter is computed to assess more quantitatively the differences from the methodology used in Wagner et al. 2023a. Circularity is defined as the ratio between the standard deviation of the MFR radius and its mean radius. This parameter helps estimate the variations in the MFR radius, with a circularity of 0 indicating a perfect circular cross-section. It is crucial for verifying the previous method developed by Wagner et al. 2023a, which assumed that the flux rope cross-section is always circular. Figure 4.6 illustrates the circularity of the MFR cross-sections in both AR 12473 (orange curve) and AR 11176 (blue curve). The dotted lines represent the circularity of the MFR structures without post-processing (i.e., without the application of a morphological opening to the binary masks). The vertical dashed lines mark the physical time windows: before these lines, the MFR is not fully formed; after them, the MFR may deform as it reaches the top boundary of the simulation domain. The very early and late stages of the simulation are thus excluded from consideration.

For both active regions, the MFRs become more circular as they ascend and develop through the simulation domain, indicating that while the previous method was not unfounded, it was less suitable for the initial and final stages of the simulation. In the middle frames, the MFR cross-section is notably more circular, particularly for AR 11176, demonstrating that the previous approach becomes more reliable in this scenario. The solid lines correspond to the circularity of the MFR cross-sections after post-processing (which, we recall, includes applying a morphological opening operation to remove noise or unwanted structures). When compared to the dotted lines, they show that the post-processing can significantly influence the shape of the MFR cross-sections

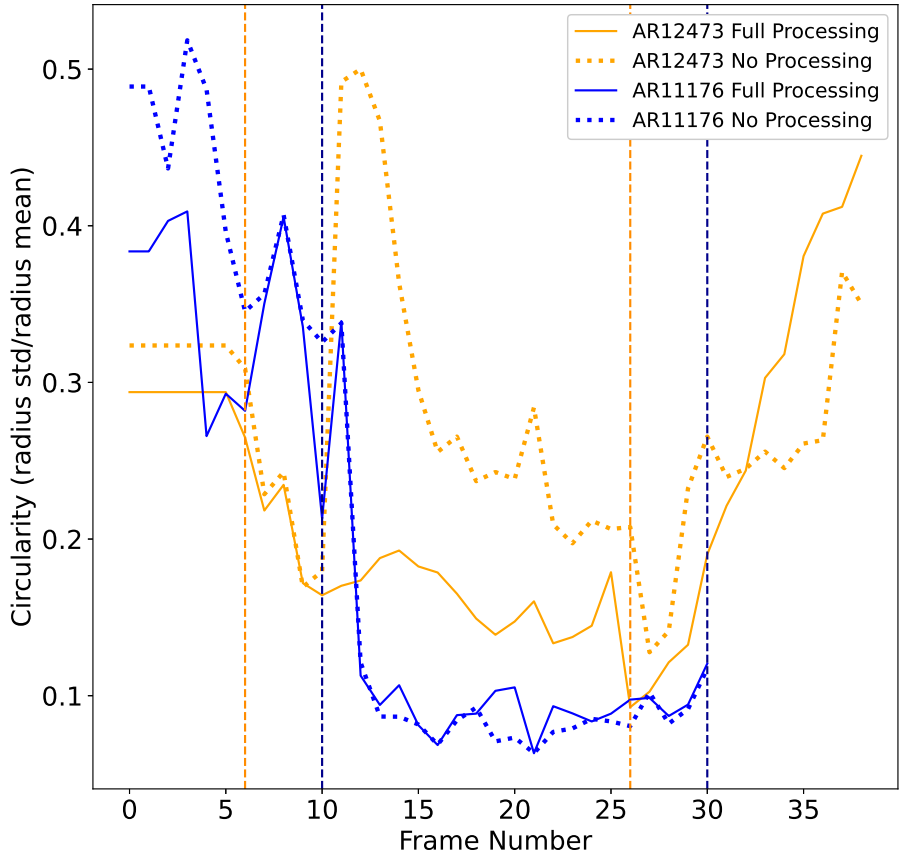

Figure 4.6: Circularity of the MFR cross-sections per frame for both MFRs in AR 12473 (solid orange curve) and AR 11176 (solid blue curve). The dotted curves also represent the circularity of the MFR cross-sections, but without post-processing (i.e., without the application of morphological opening). For example, at frame 16 in AR 12473, the circularity value indicated by the dotted orange curve corresponds to the MFR cross-section in panel (g) of Figure 4.8, while the value shown by the solid orange curve corresponds to the MFR cross-section in panel (h) of Figure 4.8, where the connected channel has been detached from the MFR structure. The dashed vertical lines mark the physical start and end of the simulation (blue for AR 11176 and orange for AR 12473). Before these lines, the MFR is not yet fully established, while after them, the MFR has risen so high that it can interact with the upper boundary of the simulation domain, potentially introducing significant bias. Source: Wagner et al. 2023b.

in some frames. This post-processing step improves the capture of the MFR morphology, making the cross-sections appear more circular. For example, at frame 11 in AR 12473, the post-processing eliminates a significant peak in the circularity distribution, resulting in a more circular MFR cross-section

by separating an elongated structure that does not belong to the MFR (as seen in the middle panel of Figure 4.2 or in the bottom panel of Figure 4.8 around y = 75 Mm and z = 50 Mm). Hence, employing the morphological gradient-based extraction method (combined with post-processing refinement through morphological opening) enables a more accurate representation of the intrinsic morphology of MFR structures.

4.3.2 Propagation and deflection

While the circularity parameter demonstrates the effectiveness of the MM method for MFR extraction, the trajectory and speed of the MFRs in each active region are crucial indicators of their dynamics and potential to erupt. The propagation and orientation of the MFRs in AR 12473 and AR 11176 differ, as shown in Figure 4.7. The top-left panel of Figure 4.7 compares the height of the MFR apex over time (frame number) for both active regions and, consequently, their expansion speed within the simulation box. The MFR in AR 11176 forms at a higher initial height (around 100 Mm) and rises to approximately 200 Mm, indicating an upward movement of about 100 Mm within the physical time window for this AR (as indicated in Figure 4.6, where frame 0 in Figure 4.7 corresponds to frame 10 in Figure 4.6, and frame 20 in Figure 4.7 corresponds to frame 30 in Figure 4.6). In contrast, the MFR in AR 12473 emerges much closer to the photosphere (around 0 Mm) and rises to about 150 Mm in the corona, covering a distance of over 150 Mm within the physical time window for this AR (with frame 0 in Figure 4.7 corresponding to frame 6 in Figure 4.6, and frame 20 in Figure 4.7 corresponding to frame 26 in Figure 4.6). This comparison shows that the MFR in AR 12473 rises more rapidly through the solar atmosphere than that in AR 11176.

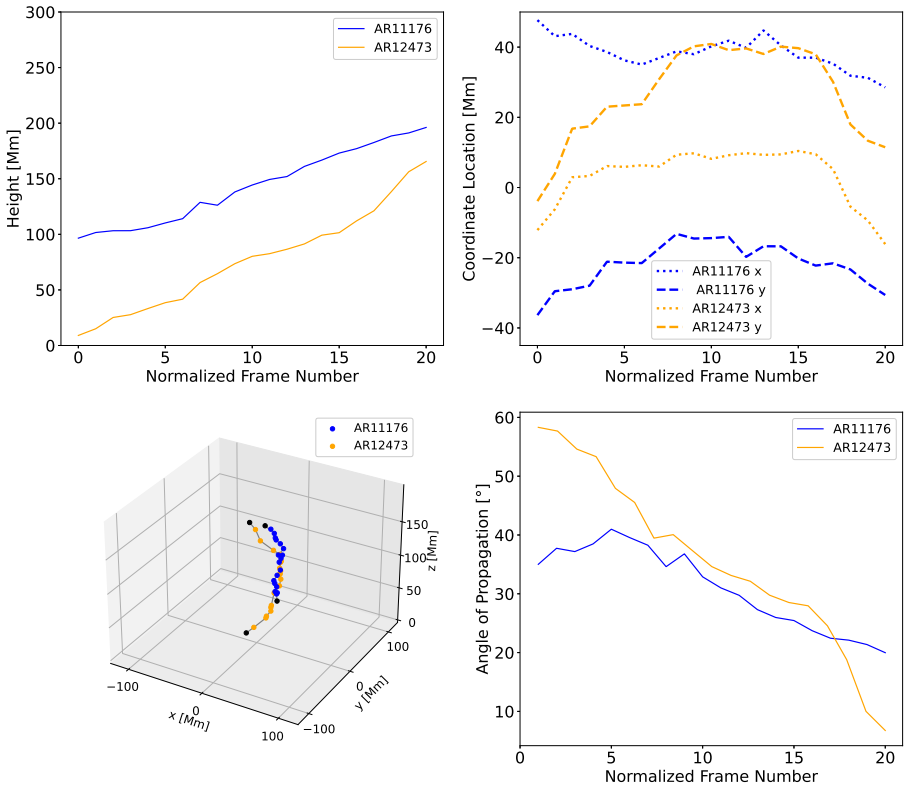

Figure 4.7: Propagation and orientation of the MFRs in AR 12473 and AR 11176. The top left panel shows the height of the extracted MFR structures per frame in each active region across 21 frames, with a cadence of 6 hours between frames. The first frame (frame 0) represents the physical start of the simulation (corresponding to frame 6 for AR 12473 and frame 10 for AR 11176 in Figure 4.6), while frame 20 represents the physical end of the simulation (corresponding to frame 26 for AR 12473 and frame 30 for AR 11176 in Figure 4.6). The top right panel displays the evolution of the horizontal x (dotted lines) and y (dashed lines) coordinates of the MFR structures in both ARs. The bottom left panel illustrates the 3D trajectory followed by both MFRs. The bottom right panel shows the angle of propagation of the MFRs as a function of the frame number. In all panels, orange represents the MFR in AR 12473, and blue represents the MFR in AR 11176. Source: Wagner et al. 2023b.

The bottom-right panel of Figure 4.7 shows the angle of propagation of the MFRs as a function of frame number. Here, the angle of propagation is defined at each frame as the angle between the vertical z-axis and the vector connecting the initial and current locations of the MFR apex. Once again, the MFRs in both active regions exhibit distinct behaviours. In AR 12473, the MFR begins with a high angle of propagation of 60°, indicating a rapid deviation from radial expansion at the outset. This angle then steadily decreases over time, eventually returning almost to the initial x and y coordinates, as shown by the black dots at the extremities of the orange curve in the bottom-left panel of Figure 4.7, which represent the MFR apex location at the beginning and end of the simulation. In contrast, the MFR in AR 11176 follows a more stable trajectory (see bottom-left panel of Figure 4.7), with angles of propagation that do not exceed 40° throughout the simulation (see bottom-right panel of Figure 4.7). This observation is further supported by the top-right panel of Figure 4.7, where the evolution of the x-coordinate of the MFR apex in AR 11176 (dotted blue line) and the y-coordinate (dashed blue line) appears steadier compared to the corresponding x- and y-coordinates of the MFR apex in AR 12473 (dotted and dashed orange lines, respectively). In particular, the y-coordinate of the MFR apex in AR 12473 undergoes a significant variation of approximately 40 Mm, ultimately returning to near its initial position by the end of the simulation (as displayed in the bottom-left panel of Figure 4.7). Although the MFRs in the two ARs exhibit markedly different dynamics and evolution, the extraction technique employing MM transformations accurately tracks both trajectories over their respective time series.

4.4 Benefits of the method over the previous assumption-based approach of perfect circularity

The MM-based approach described in Section 4.2 offers several advantages over the previous methodology used by Wagner et al. 2023a for MFR extraction from the TMFM-generated twist number maps. First, this approach is simpler, as it does not require prior assumptions or parameters. Although the SEs used in MM operations must be tested and validated through visual inspection — a process that can be somewhat time-consuming — this step allows for greater user control and the possibility of automation once optimal SEs are identified.

Notably, the post-processing with morphological opening grants substantial user control and helps customise the extraction process.

The same applies to the multi-scale morphological gradient, which enhances the boundaries between low- and highly-twisted regions in the twist number maps. Here again, the choice of SEs plays a crucial role, as it can yield significantly different outcomes. This is evident when comparing panels (c) and (e) of Figure 4.8, where the gradient applied to the twist map with large SEs (panel (c)) differ from that using smaller ones (panel (e)). Similarly, the difference is noticeable in panels (d) and (f) of Figure 4.8, where the morphological gradient is combined with the original twist number map. The MFR structure appears fainter in panel (f) due to the use of smaller SEs in the gradient operation. Consequently, larger SEs were chosen to provide a clearer definition of the MFR shape in the maps, as shown in panels (c) and (d).

Additionally, the MM approach is less computationally demanding compared to the previous methodology in Wagner et al. 2023a; all operations complete in seconds on a standard computer due to the straightforward nature of the MM operations employed in this extraction process and the use of sufficiently small SEs. Moreover, the MM approach yields more accurate results. This is illustrated in Figure 4.4, which compares the magnetic field lines computed from the MFR structure extracted at three specific frames (7, 17, and 27) in AR 12473 using the method of Wagner et al. 2023a (left panel) and the MM method (right panel). Although both methods capture the overall morphology of the MFR well at these frames, the MM approach clearly captures a greater number of field lines, resulting in a more consistent and robust MFR morphology, even at earlier stages when the MFR is just emerging from the photosphere. The MM method thus identifies more pertinent field lines while effectively excluding non-twisted lines that might overlap with the MFR structures. Additionally, in frame 17 (middle frame) of the right panel, a set of field lines connects to the positive polarity of the AR (shown in white on the right side of the magnetogram used as the lower boundary of the simulation domain). The Wagner et al. 2023a method (left panel) does not reveal this set of field lines in the corresponding frame. However, this structure reappears in later stages, specifically at frame 27 (bottom panel of the figure), in both methods, indicating that it is indeed part of the MFR. The MM approach was able to recognise these field lines as components of the flux rope at earlier stages than the Wagner et al. 2023a method, demonstrating its superior accuracy.

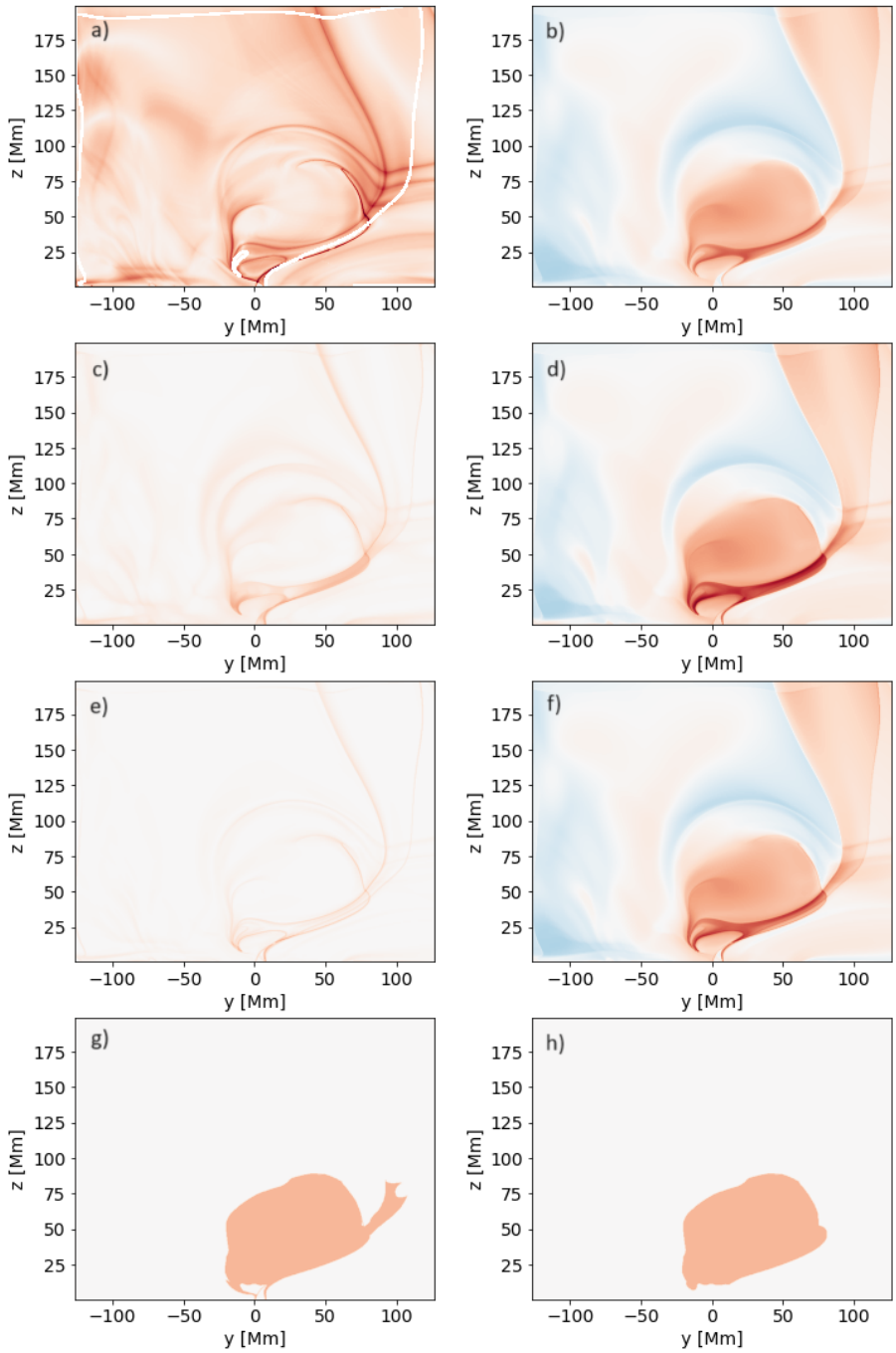

Figure 4.8: Visualisation of the MFR structure at frame 16 for AR 12473. Panel (a) presents the squashing factor map, while panel (b) shows the corresponding twist number map. Panel (c) displays the multi-scale gradient operation applied to the twist number map from panel b) using large structuring elements with sizes 5 and 10, and panel (d) combines the twist number map from panel (b) with the gradient from panel (c). Panel (e) also shows the multi-scale gradient, but with smaller SEs, and panel (f)

combines the twist number map from panel (b) with this gradient using smaller parameters. Panel (g) depicts the resulting binary mask after thresholding the combination of the twist number map and the gradient from panel (d). The threshold is fixed at 0.8 for this frame and remains constant across the entire time series, enabling effective MFR extraction. Panel (h) displays the MFR mask from panel (g) after post-processing, where a morphological opening with a small SE was applied to the entire image to remove small connections at the bottom of the MFR structure. A second opening with a larger SE was selectively applied to a sub-region of the frame around [y, z] = [75 Mm, 50 Mm] to remove the connected twisted channel appearing in panel g) that does not belong to the MFR structure. Source: Wagner et al. 2023b.

The MM method is also preferable to the previous approach because it does not necessitate the assumption of perfectly circular flux rope cross-section to be effective. As discussed in Section 4.6, the Wagner et al. 2023a technique may lack reliability, particularly when the MFR cross-section deviates from a circular shape, which is the case in the early and late stages of the simulation. Other methods could also be considered for effective MFR extraction, such as using squashing factor maps instead of twist number maps (see panel (a) of Figure 4.8). The squashing factor (Démoulin et al. 1996; Titov et al. 2002) inherently emphasises edges and variations in twist number, potentially making the application of the morphological gradient unnecessary. This factor is a metric used to analyse the complexity and topology of magnetic field lines; a high squashing factor indicates regions where magnetic field lines are significantly distorted – stretched or compressed – often associated with magnetic reconnection sites and dynamic environments. Conversely, a low squashing factor reveals a more uniform field. While useful for identifying twisted structures, the squashing factor method can sometimes produce contours that do not close entirely, complicating the subsequent application of a threshold. Additionally, it lacks the flexibility and tunability of the MM gradient, which can be adjusted through the use of different SEs. On the other hand, the combination of the MM gradient with twist number maps allows for the application of a consistent threshold throughout the entire time series, automating the extraction process and mitigating the influence of noise or artifacts.

4.5 Concluding remarks

In summary, the MM method used in this study, which employs a multi-scale gradient to enhance edges in twist number maps from TMFM simulations and

incorporates morphological opening during post-processing, proves effective in capturing the cross-sectional shapes of MFRs across the time series of two active regions. The series cover the period around 28 December 2015 for AR 12473 and around 3 April 2011 for AR 11176, corresponding to solar eruptions in these regions. The method successfully tracks the evolution of the MFRs into well-defined twisted structures. Although the modelled MFR field lines do not capture the eruption in AR 11176 due to the simulation ending before this event, they accurately represent the magnetic environment associated with a large suspended prominence observed in this AR. Analysis reveals a more gradual and uniform expansion with a consistently compact and circular shape for this MFR. In contrast, the MFR in AR 12473, as delineated by the MM method, exhibits more dynamic behaviour, characterised by rapid ascent and two significant deflections: an initial deviation from the radial direction and a later return to the original horizontal plane location. Thus, the MM method effectively captures the contrasting dynamics and behaviours of these two MFRs: one likely eruptive (consistent with the M1.9 solar flare on 28 December 2015 in AR 12473) and the other non-eruptive (matching the suspended prominence rather than the later eruption in AR 11176). This is particularly valuable given that there are currently limited automated methods available for detecting MFRs, such as the approach developed by Lowder et al. 2017, which involves thresholding magnetic field line helicity maps. Advancing these automated detection techniques is essential for improving coronal modelling and gaining deeper insights into solar eruptions in the Sun's upper atmosphere.

Chapter 5

Detection and statistical analysis of coronal off-limb structure properties

Up to this point, this thesis has focused on the analysis and detection of faculae in chromospheric images (see Chapter 2), sunspots in photospheric observations (see Chapter 3), and magnetic flux ropes in simulation-generated data from the low corona (see Chapter 4). However, the higher corona, and the corona as a whole, hosts various solar structures that play crucial roles in triggering space weather phenomena. This chapter introduces the dataset of coronal structures derived by Bourgeois et al. 2024b and examines their properties as detailed in that study. These coronal structures include loops, prominences, and coronal jets, which are larger and longer-lived than their chromospheric counterparts, spicules (Secchi 1878).

Coronal jets, in particular, are crucial to study as they share dynamic properties with larger solar eruptions, such as CMEs, which are driven by magnetic activity, though their effects are more localised (Raouafi et al. 2016). These elongated plasma ejections are visible across various wavelengths — for example, chromospheric channels highlight shorter jets (up to 10 Mm), known as spicules. Understanding the mechanisms behind their formation and eruption — including Alfvén waves and pulses, MHD shocks, granular buffeting, magnetic reconnection, and instabilities — is key to interpreting solar wind acceleration and addressing the long-standing problem of atmospheric heating

(i.e, in the chromosphere and corona), which manifests as sudden temperature rises exceeding one million Kelvins far from the solar surface.

Alfvén waves and pulses, in particular, have been extensively studied. Barnes 1969 proposed a model for solar wind heating through the damping of hydromagnetic waves. More recently, Grant et al. 2018 provided observational evidence of chromospheric heating in a sunspot umbra via Alfvén wave dissipation. Van Doorsselaere et al. 2020 reproduced high coronal temperatures using a 3D MHD model incorporating Alfvén waves. Additionally, Alazraki et al. 1971 and Belcher 1971 demonstrated how coronal Alfvén waves affect solar wind properties, accelerating the solar wind. Wedemeyer-Böhm et al. 2012 suggested that vortex flows might generate Alfvén waves and transport energy from the lower to the upper atmosphere. Other studies (Liu et al. 2019; González-Avilés et al. 2019; Oxley et al. 2020; Scalisi et al. 2021) proposed that shear (e.g., torsional) solar motions could be responsible for generating Alfvén waves and associated jets.

Coronal jets also contribute to the acceleration of coronal streamers (Satya Narayanan et al. 1985; Usmanov et al. 2000) and the heating of prominences (Soler et al. 2016), coronal loops (Halberstadt et al. 1995; Ballegooijen et al. 2017), and coronal plumes (Wu et al. 2003). Despite significant progress, the physics underlying the dynamics of these coronal structures — such as jets, loops, prominences, streamers, and plumes — remains not fully understood. However, gaining a better understanding of these phenomena is crucial for interpreting eruptive events in the near-Sun environment and assessing their impact on Earth.

Previous studies have focused on specific types of coronal structures, such as jets, prominences, coronal loops, and streamer-associated CMEs. For instance, Liu et al. 2023 analysed $1,215$ coronal jets, with Soós et al. 2024 later extending this work to include a total of $2,704$ jets observed throughout SC 24. Similarly, Zhang et al. 2024 examined $50,456$ prominences during approximately the same period (2010–2020). Research on coronal loops includes Li et al. 2023's study of 111 loops observed in Solar Orbiter (SolO)/Extreme Ultraviolet Imager (EUI) 174 Å images, focusing on a particular active region, while Shrivastav et al. 2024 analysed 42 oscillations in small-scale coronal loops, also using SolO/EUI 174 Å. Zimovets et al. 2015 investigated 58 kink oscillations in coronal loops using SDO/AIA 171 Å data from 2010 to 2014. In addition, Moon et al. 2006 examined streamer-associated CMEs and found that about a

quarter of the 3,810 CMEs they inspected, recorded by SoHO/LASCO, were streamer-associated, highlighting the significant role of coronal streamers in space weather phenomena.

In this chapter, we examine all coronal off-limb structures visible in our dataset, detected using a simple yet efficient mathematical morphology algorithm described in Section 5.2. This approach enhances the statistical analysis of coronal structure properties and provides insights into the overall evolution of the corona. The corona presents many complexities and challenges, including understanding coronal heating (which originates in the chromosphere), solar wind acceleration into interplanetary space, and eruptive behaviours. Observing the magnetic field dynamics in the corona through these structures is key to deciphering the underlying physics, both in terms of broad solar cycle evolution and localised effects.

5.1 Data collection for Solar Cycle 24

We sought to identify coronal off-limb structures using SDO/AIA 304 Å images spanning Solar Cycle 24, from June 2010 to December 2021. Initially, Liu et al. 2023 pre-processed these images, which were selected at 6-hour intervals: 00:00:00, 06:00:00, 12:00:00, and 18:00:00 UT daily. Soós et al. 2024 later refined the dataset by introducing additional times at 03:00:00, 09:00:00, 15:00:00, and 21:00:28 UT, resulting in a 3-hour interval dataset. The pre-processing procedure described by Liu et al. 2023 involved downsizing image dimensions from 4096×4096 to 512×512 for better data management and computational efficiency, normalisation to ensure consistency in pixel values across all images, binarisation, and enhancing coronal features by masking chromospheric elements up to 14 Mm above the solar radius. This last step removes unwanted chromospheric features, while the choice of the observation wavelength in the 304 Å channel facilitates the identification of coronal off-limb structures. An example of a pre-processed image according to the methodology of Liu et al. 2023 is shown in Figure 5.1. The inverted image is displayed for visualisation purposes, meaning that the bright coronal off-limb structures and surrounding noise appear in black against the white solar disk and background of outer space. In this image (as well as in all the images within the dataset), we aim to eliminate pepper noise and focus exclusively on the coronal off-limb structures bursting around the solar disk. The two red arrows in Figure 5.1

indicate the locations of two visually checked coronal jets.

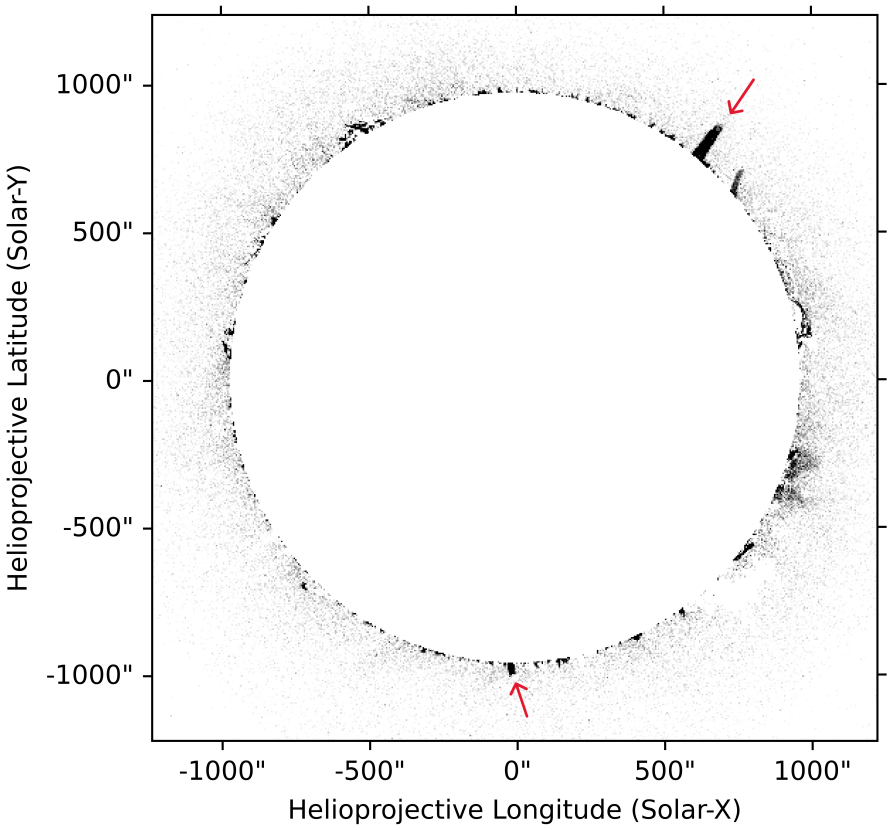

Figure 5.1: Pre-processed image from SDO/AIA in the 304 Å channel, observed on 06/06/2010 15:00:00 UT, created following the methodology outlined by Liu et al. 2023, which includes downsizing, normalisation, and masking of the solar disk to a height of 14 Mm above the solar radius. For improved visualisation, the image is inverted so that coronal features are displayed in black against the white background. The red arrows highlight coronal jets that have been manually verified through visual inspection of 1-hour video sequences (see Soós et al. 2024 for reference). Source: Bourgeois et al. 2024b.

5.2 MM algorithm

Once all the images were pre-processed following the methodology described by Liu et al. 2023 as shown in Figure 5.1, the dataset was ready for MM operations to remove noise and extract the features of interest — namely, the coronal off-limb structures around the solar disk. As in previous chapters of this thesis, the DIPlib library was used as a powerful tool for quantitative image analysis.

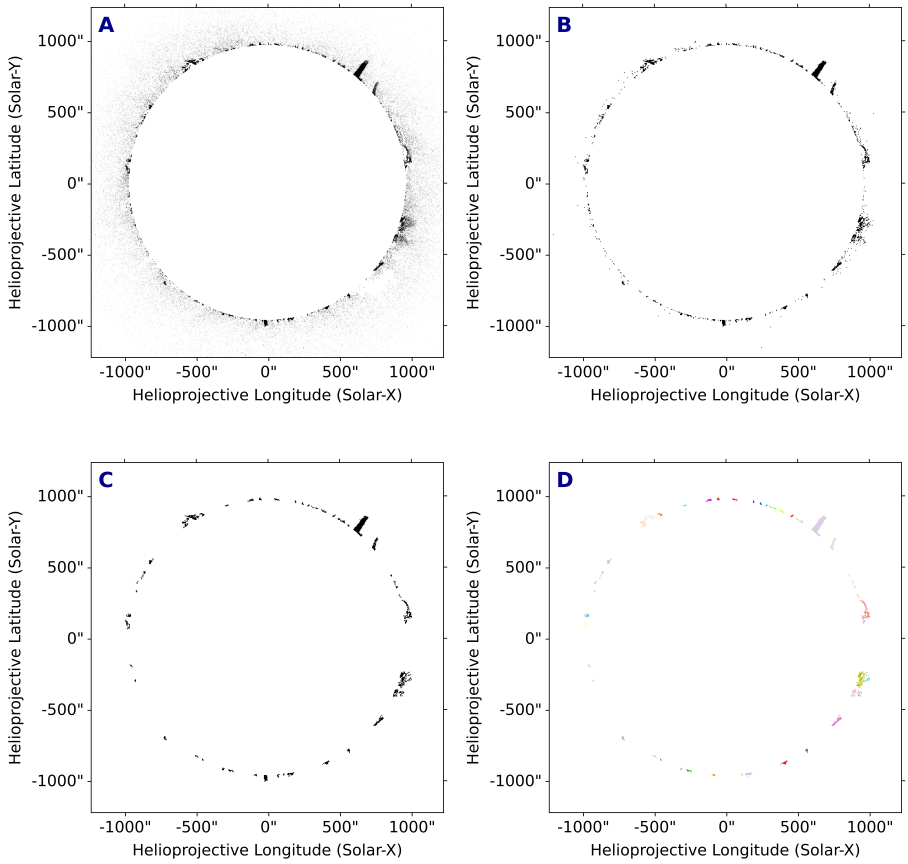

Figure 5.2: Key steps of the extraction algorithm utilised for the image depicted in Figure 5.1. Note that the images are inverted for enhanced visualisation. Panel A: Application of the white top-hat operation: this process isolates small, bright features in the image (highlighted here in black) that are smaller than the SE size of 200 pixels. Panel B: Implementation of a fixed threshold. Panel C: Small object removal function: noise smaller than the SE size of 5 pixels is removed, allowing only the relevant structures to remain. Panel D: Labelling: each coronal off-limb structure is uniquely identified. Source: Bourgeois et al. 2024b.

The MM algorithm applied to the images in the dataset is outlined in Figure 5.2. The first and most critical step — as it allows for the identification of coronal off-limb structures as peaks in the image — is to apply a white top-hat operation. As shown in panel A of Figure 5.2, this operation indeed extracts small, bright features that are smaller than the SE size used in this process (200 pixels; see Table 5.1). As detailed in Section 2.3.6, this operation subtracts the result of the morphological opening from the original image. The opening step isolates relatively small coronal off-limb structures (compared

Table 5.1: Parameter values applied in the top-hat, small object removal function, and thresholding operation.

Top-hat	Threshold	Object removal
200	135	5

to the size of the solar disk), while the white top-hat operation, through subtraction, restores and emphasises these features.

Next, the second step, shown in panel B of Figure 5.2, involves applying a threshold operation with a cut-off value of 135 (see Table 5.1) to discard background noise with lower pixel intensity values. Despite this thresholding step, some residual noise persists around the solar disk, necessitating the use of a small object removal function, which, as its name suggests, removes objects smaller than a certain size in a binary image (refer to the DIPlib library). As shown in panel C of Figure 5.2, applying this small object removal function with a value of 5 pixels (see Table 5.1) helps eliminate the remaining noise, resulting in a cleaner image where the desired coronal off-limb structures are more clearly identified. While we used this small removal function as provided in DIPlib, similar results could also have been achieved using the morphological opening operation. Subsequently, these structures are uniquely labelled, as illustrated in panel D of Figure 5.2, with each colour and number representing a distinct coronal off-limb structure. In this example, 53 individual coronal off-limb structures are extracted.

Finally, a morphological half-gradient by dilation was applied, enabling the detection of the external contours of the labelled structures. An example of these identified contours is shown in Figure 5.3, where the contouring resulting from the external gradient operation is superimposed in red onto the original image from Figure 5.1. To enhance the visualisation of the identified structures, the image is inverted, displaying the bright coronal features in black. Additionally, the large red contours generated by the gradient transform were eroded using an erosion operation with an SE size of 2.5 pixels to improve the clarity of the identified structures.

5.3 Data filtering

The resulting dataset containing all the processed images with identified contours of the coronal off-limb structures required further filtering, as many SDO

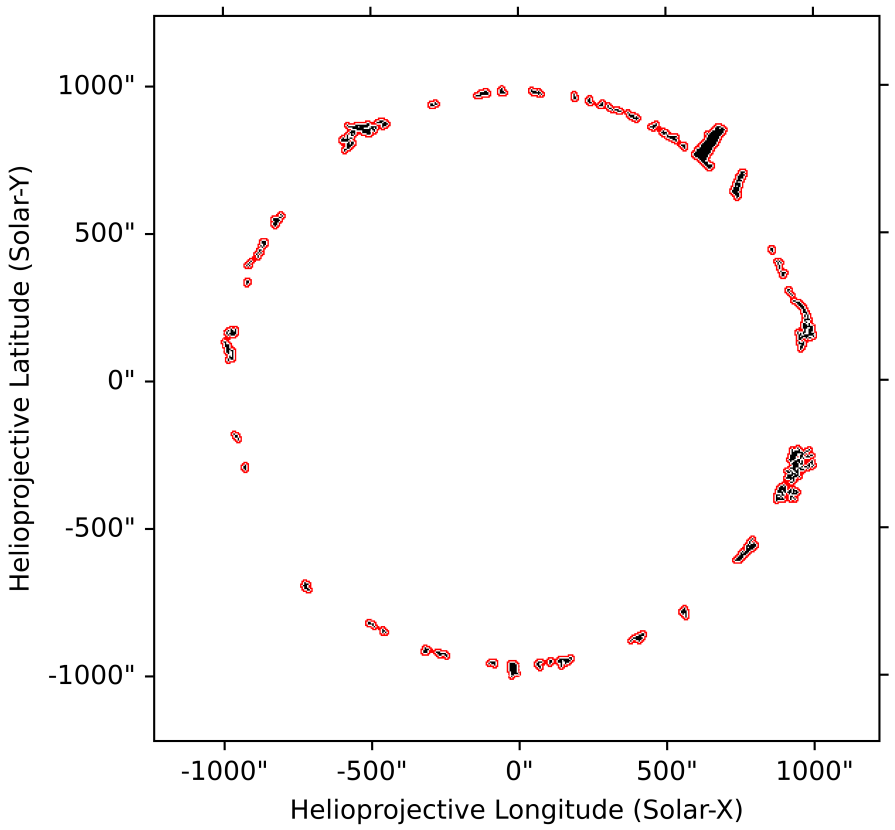

Figure 5.3: Identified coronal off-limb structures in the image presented in Figure 5.1, recorded on 06/06/2010 at 15:00:00 UT. For enhanced visualisation, the image has been inverted, causing the coronal off-limb structures to appear in black against the white background. The external contours of these structures are highlighted in red, following the application of the morphological half-gradient operation by dilation. This process emphasises the boundaries of the coronal structures, aiding in their identification and analysis. Source: Bourgeois et al. 2024b.

images were too noisy or had misaligned solar disk. First, we visually inspected half of the dataset to manually remove poor-quality images, aiming to create a cleaner dataset and reduce false identifications. Although this process was thorough, it was also highly time-consuming. To expedite the process for the second half of the dataset, we adopted a more efficient approach by eliminating images that were statistical outliers in terms of structure density. In noisy or misaligned images, the MM algorithm often mistakenly identified each noise artifact as a coronal structure, resulting in an unusually high density of detected features. By discarding these high-density outlier images, we significantly

improved the dataset's quality.

Additionally, to deal with the noise inherent in the original data, we applied a threshold value of 685 Mm, which sets a minimum distance between the bottom pixel coordinates of the detected coronal off-limb structures and the solar centre coordinates. This step was necessary because, in noisy images, the MM algorithm tends to detect noise artifacts within the solar disk and identifies them as coronal structures. Consequently, images with identified coronal structures located inside the solar disk are indicative of noise. The threshold effectively filtered out these poor-quality images without requiring visual checks. As a result of all these filtering steps, we obtained a cleaner dataset with a significantly reduced rate of false identifications. In total, the dataset contains $32,985$ cleaned images and identifies a large number of $877,843$ coronal off-limb structures.

5.4 Validation

For validation, results from the Semiautomated Jet Identification Algorithm (SAJIA) developed by Liu et al. 2023 were compared against those obtained from the MM method. The dataset of $1,215$ coronal jets provided by SAJIA was visually verified and later expanded to $2,704$ jets by Soós et al. 2024. The SAJIA was subsequently upgraded to the Automated Jet Identification Algorithm (AJIA) by Liu et al. 2024 to enhance the algorithm's capacity to identify true jets. The coronal jets detected by both SAJIA and AJIA were manually checked using video sequences (Soós et al. 2024), resulting in a large jet dataset that includes true jets, false identifications, unknown jets, and uncertain jets — the latter being defined as cases where there is insufficient video data before or after jet detection to confirm the validity of the identification.

Visual checks confirmed that the MM algorithm successfully extracted the coronal jets (both true and false) identified by Liu et al. 2023; Soós et al. 2024; Liu et al. 2024. The spatial distribution (latitude, longitude, and position angle), as well as area and intensity, were compared between the SAJIA-detected coronal jets and the structures identified using the MM method, revealing similar results. This validation process not only confirms the effectiveness of the MM method employed in this work but also categorises several structures in the MM-produced dataset: $2,688$ true jets, $5,118$ false jets (which resemble

straight-like jets in static images but do not behave as jets when their dynamic behaviour is checked on video), 42 unknown jets, and 39 uncertain jets. All other structures are labelled as "MM_U" in the dataset, indicating unknown MM-detected coronal structures.

5.5 Major characteristics of coronal off-limb structures

In the cleaned dataset, several properties of the coronal off-limb structures are recorded at each time step (every three hours) between June 2010 and December 2021. These structures encompass a broad range of coronal features, from prominences and coronal loops to coronal jets and other coronal phenomena. It is important to note that the dataset does not distinguish these different features into separate categories. Additionally, if a coronal off-limb structure persists for more than three hours, it is classified as a new structure at the next time step. This approach may introduce some bias, as two entries with differing properties in the dataset could actually correspond to the same physical feature.

With this in mind, the dataset includes the following properties: the observation day and time (recorded in UT), the perimeter and area of the structures (measured in Mm and pixels, and in Mm^2 and $pixels^2$, respectively), and the intensity of the structures recorded in digital numbers (DN). The intensity values are corrected for the degradation of the charge-coupled device (CCD) onboard SDO/AIA using the *aia* package (Barnes et al. 2020). The dataset also includes the skewness and kurtosis of the intensity distribution, which provide information about the horizontal spread (skewness) and the vertical spread (kurtosis) of the intensity values.

Additionally, the length and width of the structures were measured using the Feret diameter tool provided by the DIPlib library. The Feret diameter represents the distances between any two parallel tangents to the object's outline; consequently, the length corresponds to the maximum Feret diameter, while the width corresponds to the minimum Feret diameter. The dataset also includes the ratio of length to width, as well as the Aspect Ratio Feret, which differs from the length-to-width ratio. The Aspect Ratio Feret is defined as the ratio between the width and the perpendicular diameter to the width, which indeed does not necessarily equal the length.

The dataset further contains spatial information on the central coordinates of the structures (in pixels) and their position angle (PA), which indicates the angle of the structure's centroid from the solar north pole, measured counterclockwise. The latitude and longitude of the coronal features' centroids are also included, along with their latitude and longitude values corrected for the $B0$ angle using the *sunpy* package (Community et al. 2020). The $B0$ angle is the heliographic latitude of the solar disk centre, which varies sinusoidally between $-7.23°$ and $+7.23°$ as seen from Earth. However, this $B0$ correction introduced unintended sinusoidal trends at the solar poles in our analysis of latitudinal distributions. Therefore, we opted to use the uncorrected latitude and longitude values in the subsequent analysis presented in this chapter.

Some morphological and shape descriptors were also incorporated into the dataset, including the Podczeck shape descriptors. These five descriptors evaluate the elongation of an object (Equation 5.1) and its similarity to shapes such as a square (Equation 5.2), a circle (Equation 5.3), a triangle (Equation 5.4), and an ellipse (Equation 5.5). In Equations 5.1–5.5, A denotes the area of the structures defined inside the contours detected by the MM method, P represents the perimeter, w is the width, l is the length, and h refers to the structure's diameter perpendicular to the width (which, we recall, is not necessarily equal to the length).

$$P_{elongation} = \frac{P}{l} \tag{5.1}$$

$$P_{square} = \frac{A}{wh} \tag{5.2}$$

$$P_{circle} = \frac{4A}{\pi h^2} \tag{5.3}$$

$$P_{triangle} = \frac{2A}{wh} \tag{5.4}$$

$$P_{ellipse} = \frac{4A}{\pi hw} \tag{5.5}$$

The dataset also includes measures of circularity and roundness. Circularity is defined as the ratio between the mean radius and the standard deviation of the radius, reflecting variations in the radius; a circularity value of 0 represents no variations, indicating a perfectly circular-shaped structure. Roundness, a similar metric, assesses the circularity of the structure using its perimeter and area (see Equation 5.6), where a roundness value of 1 denotes a fully circular

shape.

$$R = \frac{4\pi A}{P^2} \tag{5.6}$$

Additional descriptors, such as bending energy, eccentricity, solidity, and convexity, are also recorded in the dataset. Bending energy quantifies the deformation of the structures' contours, while eccentricity again measures how much a structure deviates from a circular shape, based on the aspect ratio of its best-fit ellipse. Solidity and convexity provide insights into the convexity of the structures. Convexity is defined as the ratio between the perimeter of the convex hull and the perimeter of the structure, where the convex hull represents the smallest convex boundary enclosing the structure (a convex set being one that includes any line segment connecting two of its points). Solidity also measures convexity but in a higher dimension, as it calculates the ratio between the area of the structure and the area of its convex hull. Both measurements range from 0 to 1, with a value of 1 indicating a fully convex shape with no protrusions.

Other attributes included in the dataset are the maximum radius, minimum radius, mean radius, and standard deviation of the radius for each structure. The dataset also records the top and bottom pixel coordinates of each structure, along with the distances (in both pixels and Mm) from these coordinates to the solar centre.

Finally, as discussed in Section 5.4, most structures in the dataset are categorised as unknown structures, while the remaining ones are classified as true jets, false jets, unknown jets, and uncertain jets, using the labelled jet dataset developed by Liu et al. 2023; Soós et al. 2024; Liu et al. 2024. The full property dataset is available at the following link on the University of Sheffield Online Research Data (ORDA) repository: DOI: 10.15131/shef.data.27130590.

5.6 Strengths and limitations of the dataset

The developed dataset, which includes numerous properties of coronal off-limb structures (as described in the previous section), is a significant asset. The extensive collection of 877,843 recorded coronal off-limb structures spanning a solar cycle facilitates in-depth analysis of the solar corona and its long-term evolution. This wealth of data allows for the identification of patterns and

trends that may not be apparent in smaller datasets. Furthermore, the variety of recorded properties — particularly those that are critical for correlating these coronal features with space weather phenomena, such as latitude, longitude, area, and intensity — enables thorough statistical analyses. As such, this dataset provides a robust foundation for advancing our understanding of coronal behaviour, their relationship with space weather events, and the subsequent impacts on the heliosphere and Earth.

However, several important limitations should be noted. First, long-lived structures are not recorded as such; any structure lasting longer than three hours is classified as a new structure. The detection method also does not distinguish between different types of coronal structures, except for coronal jets, which have been labelled by Liu et al. 2023; Soós et al. 2024; Liu et al. 2024. Furthermore, it does not provide information about the stage of a structure (i.e., whether it is in the beginning, intermediate, or late stage of evolution).

Another limitation pertains to the measurement of length and width of the structures as recorded in the dataset. As explained in Section 5.5, these properties are calculated using the Feret diameter, where the length corresponds to the maximum Feret diameter and the width to the minimum. However, depending on the orientation of the structure in the image (for example, in the case of a highly inclined feature on the solar disk), the maximum Feret diameter may actually represent the width, while the minimum Feret diameter may represent the length. This interchangeability, influenced by the orientation of the structure, can render these measurements unreliable for statistical analysis.

Thirdly, the size of the SE used in the white top-hat transform to extract coronal off-limb structures from the dataset images was determined through visual inspection. The SE size of 200 pixels (see Section 5.2) was selected to retain the largest coronal structures of interest while minimising noise. Nonetheless, this approach might have inadvertently filtered out some smaller but significant coronal structures or misclassified larger noise artifacts as actual coronal features. However, this effect is considered negligible due to the vast number of identified coronal structures and the fact that half of the dataset underwent visual verification.

Finally, it is crucial to consider the degradation of the CCD sensor on the AIA instrument, which can introduce significant bias into the intensity measurements. As illustrated in Figure 5.4, the sensitivity of the AIA's CCD has been declining at an alarming rate across all wavelength channels, particularly

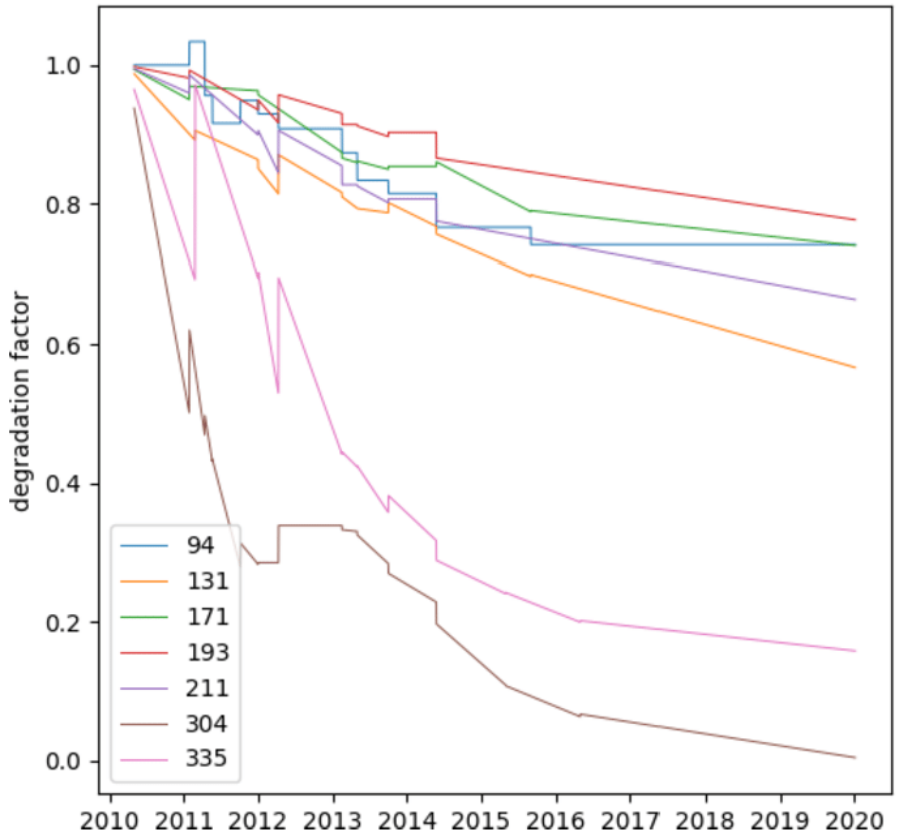

Figure 5.4: Evolution of the AIA's CCD sensitivity degradation over time across all seven AIA EUV wavelength channels: 94 Å, 131 Å, 171 Å, 193 Å, 211 Å, 304 Å, and 335 Å. The degradation is particularly severe in the 335 Å channel and even more pronounced in the 304 Å channel, which experiences the most significant decline. Although the remaining channels are less affected, they still display alarming degradation factors, ranging from 0.6 to 0.8 by 2020, indicating a substantial loss in sensitivity over time. Source: Zwaard et al. 2021.

in the 335 Å and 304 Å channels, with the latter being exclusively used in this study. Figure 5.4 shows that this sensitivity degradation began almost immediately after the SDO was launched and started operations. Within two years, the 304 Å channel experienced a significant drop in sensitivity, reaching a degradation factor of approximately 0.2. By 2020, this had further declined to nearly 0.0, making it the most affected channel. Even the less affected channels (94 Å , 131 Å , 171 Å , 193 Å , and 211 Å) have not been immune to this issue, with their degradation factors ranging between 0.6 and 0.8 by 2020. This decline in CCD sensitivity is an important factor to take into account, as it

can heavily impact our analysis of the intensity of coronal off-limb structures observed in the 304 Å channel. This is illustrated in Figure 5.5, which shows the monthly number of coronal off-limb structures and their average intensity over time from 2011 to 2021. The colour and size of the data points represent the intensity of the structures (corrected for CCD deterioration, as noted in Section 5.5), with larger and darker markers indicating higher-intensity features, and smaller, lighter markers indicating lower-intensity features.

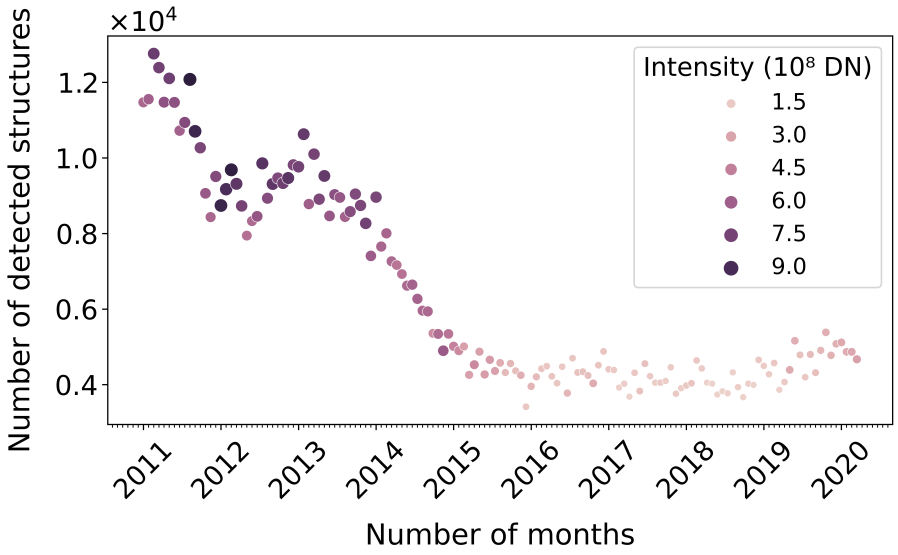

Figure 5.5: Number of detected coronal off-limb structures and their average intensity per month, from January 1, 2011, 00:00:00 UT to December 31, 2021, 21:00:28 UT (recorded at three-hour intervals). The intensity is represented by the size and colour of the markers in digital numbers (DN). Both intensity and the number of structures show a correlation, with peaks in 2011 (just a few months after SDO began observations) and in 2013 (before solar maximum). This is followed by a very sharp decrease, and a slight increase around 2020, indicating the onset of Solar Cycle (SC) 25. Source: Bourgeois et al. 2024b.

Figure 5.5 reveals a higher number of structures and stronger intensities between 2011 and 2014, followed by a drastic decrease in both intensity and density. Notably, the highest number of detected structures occurred in 2011, with a rapid decline observed thereafter, interrupted by a brief increase between 2012 and 2013. At the beginning of Solar Cycle (SC) 25 around 2020, there is a slight resurgence in both the density and intensity of the features. While these observations generally align with the expected evolution of the solar cycle, the steep decline after 2011 and 2013 may not be solely due to the solar cycle

itself; it could also be influenced by the degradation of the CCD, which began shortly after the SDO's launch in 2010 (Ahmadzadeh et al. 2019; Zwaard et al. 2021; Soós et al. 2024) and continues to affect the results despite the corrective measures provided by the *aia* package (Barnes et al. 2020). Therefore, it is crucial to interpret the statistical information regarding the intensity of coronal off-limb structures in the subsequent figures with caution (e.g., in Figures 5.8, 5.9, 5.10), keeping the CCD's significant deterioration in mind.

5.7 Latitudinal activity and North-South asymmetry

Having presented the dataset, we will now explore its properties, beginning with the latitude distribution of the $877,843$ recorded coronal off-limb structures. This analysis aims to understand how these coronal features evolve latitudinally throughout the solar cycle and to determine whether they exhibit behaviour similar to that of their photospheric (e.g., sunspots) and chromospheric (e.g., faculae, filaments) counterparts, following the classical pattern known as the butterfly diagram. In the butterfly diagram, solar activity begins at mid-latitudes, around 20° to 30° in both hemispheres, during solar minimum. Then, as solar activity intensifies, it progressively shifts closer to the equator, forming the so-called wings of the butterfly diagram. This cycle repeats as solar activity reemerges at mid-latitudes with the onset of the next solar cycle (Schwabe et al. 1844; Maunder 1904; Hathaway 2010).

The latitudinal distribution of all detected coronal off-limb structures is shown in Figure 5.6, which displays the probability density function (PDF) of the latitude — representing the likelihood of coronal structures appearing at specific latitudes. To avoid edge effects at the distribution boundaries (at $-90°$ and $90°$ latitude), the data has been "rolled up", meaning it has been extended continuously on both ends to smooth out the edges. The probability density is lowest near the solar poles, where coronal activity is less pronounced. A local minimum is also observed near the equator, indicating that although coronal activity tends to migrate closer to the equator as it intensifies, it does not reach the equator itself, which is in accordance with the pattern seen in the butterfly diagram. The highest probability density is observed in two notable peaks: around 20° to 30° in the Northern hemisphere and $-30°$ to $-20°$ in the

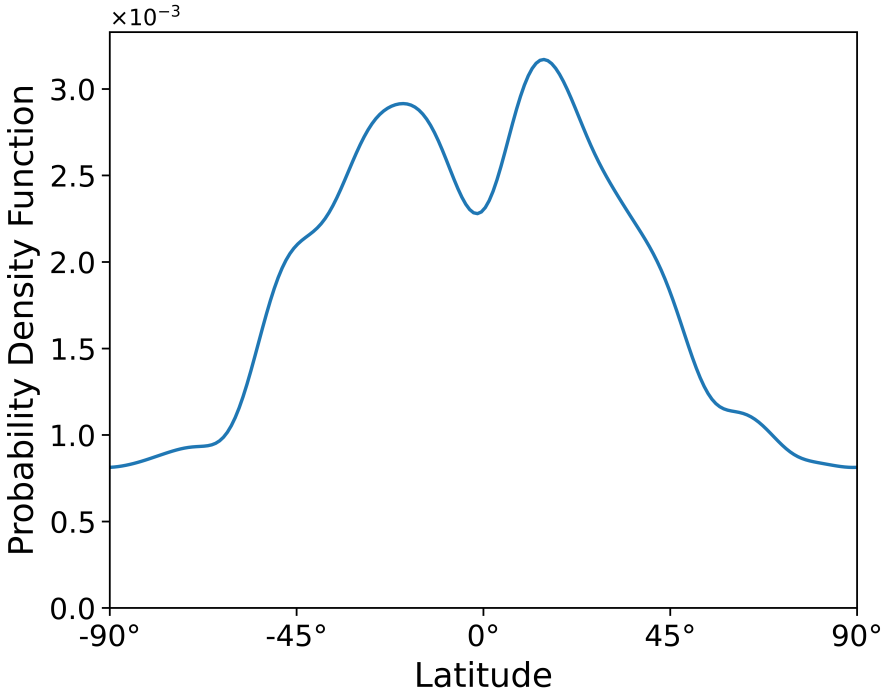

Figure 5.6: Probability density function of the latitude of coronal off-limb structures spanning SC 24. Two peaks at approximately $20°/30°$ and $-30°/-20°$ indicate the active latitude belts, similar to the butterfly diagram, with a slight difference between these peaks suggesting the North-South (N-S) asymmetry. Source: Bourgeois et al. 2024b.

Southern hemisphere, corresponding to the active latitude bands seen in other solar features. There is a slight gap between these two peaks: the Northern peak has a probability density of $3,17 \times 10^{-3}$, while the Southern peak is slightly lower at $2,91 \times 10^{-3}$.

This difference points to the so-called North-South (N-S) asymmetry, an imbalance in the distribution of solar activity between the Northern and Southern hemispheres (Babcock 1959; Svalgaard et al. 2013; Janardhan et al. 2018). Although the underlying cause of this asymmetry is not yet fully understood, studies highlight its connection to differential rotation, near-equatorial meridional circulation (Blanter et al. 2021), and the dynamo mechanisms driving solar activity. As demonstrated by Kitchatinov et al. 2021, the N-S asymmetry may arise from the interaction between a dominant dipolar magnetic field and a weaker quadrupolar magnetic field. Specifically, when these fields are synchronised (i.e., in locking phase), the interaction can lead to a Northern-

dominant asymmetry when in phase or to a Southern-dominant asymmetry when in antiphase. This process is influenced by fluctuations in dynamo effects, such as the alpha effect, which twists and converts toroidal magnetic fields into poloidal fields through turbulent convection in the convection zone. When the alpha effect undergoes symmetric changes across the equator, it can enhance or even trigger quadrupolar excitation by the dipolar field. Moreover, Kitchatinov et al. 2021 show that during Grand Minima, magnetic quenching — where the efficiency of the alpha effect is reduced — becomes less effective at stabilising the dipolar and quadrupolar fields, thereby leading to more pronounced asymmetries.

The N-S asymmetry is further highlighted in Figure 5.7(a), which displays the PDF distribution of the latitude of coronal off-limb structures across the years from 2010 to 2021. The first row includes only six months of data, starting in June 2010, while all other rows represent complete years. This distribution is obtained by applying kernel density estimation (KDE), a non-parametric method that uses a kernel function (in this case, a Gaussian function) to treat and smooth each data point by approximating it with this function, resulting in a continuous probability density curve. A bandwidth of 0.5 is used to avoid over-fitting or over-smoothing. As in Figure 5.6, the KDE distribution has been "rolled up" to prevent edge effects. In Figures 5.7(a) and 5.7(b), the KDE distribution is not normalised, so the height of the rows (representing time, with years in Figure 5.7(a) and months in Figure 5.7(b)) can be evaluated qualitatively but not compared quantitatively. This applies to all subsequent PDF distributions of this chapter generated by applying KDE (Figures 5.11, 5.12, 5.13). The bandwidth value of 0.5 is also consistently applied across all these figures.

In Figure 5.7(a), coronal activity is predominantly observed in the Northern hemisphere during SC 24, except for the periods 2013-2014 and 2020-2021. This observation aligns with the findings of Zhang et al. 2024 on active regions, which also indicate a predominance of activity in the Northern hemisphere, with the exception of the years 2012-2015 and 2020. Coronal activity is modulated by the solar cycle evolution, with its latitudinal behaviour following the characteristic butterfly diagram pattern, featuring regions of increased activity around $20°/30°$ and $-30°/-20°$ that shift over time. These regions move towards the equator during the ascending phase of the solar cycle and towards higher latitudes during the descending phase. Coronal activity in the Northern

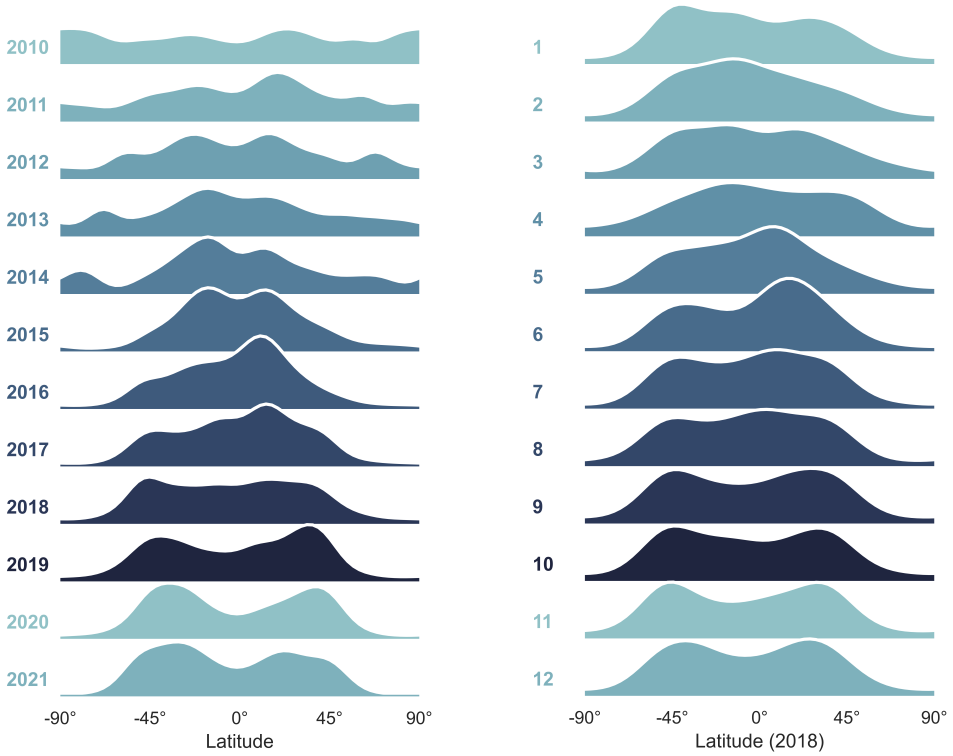

(a) Yearly distribution of coronal off-limb structures per latitude (row 1 corresponds to the year 2010; row 12 corresponds to the year 2021). The first row (year 2010) includes only half of the data, starting from June, while all other rows represent complete years. This distribution clearly shows the evolution of the solar cycle, showing two distinct peaks in the latitudinal distribution of coronal features in both hemispheres that gradually move toward the equator as SC 24 progresses. At the onset of SC 25, these peaks shift back to higher latitudes in both hemispheres.

(b) Monthly distribution of coronal off-limb structures per latitude throughout the year 2018 (row 1 represents January; row 12 represents December). The peak heights of preferred latitudes fluctuate between hemispheres, revealing the N-S asymmetry. At first, there is a predominance of coronal activity in the Southern hemisphere, followed by a shift to the Northern hemisphere, with nearly symmetrical activity between the hemispheres by the end of the year.

Figure 5.7: Yearly (covering SC 24) and monthly (for the year 2018) distributions of coronal off-limb structures per latitude. The distributions align with the butterfly diagram and highlight the N-S asymmetry.

hemisphere is particularly pronounced in the years 2016 and 2017, corresponding to the declining phase of SC 24, where the distribution shows almost a single peak concentrated in the Northern hemisphere. Around the minimum of SC 25, between 2018 and 2021, active latitudes reappear at mid-latitudes,

and the peaks in both hemispheres become more widely separated, located at approximately 40° and −40°. During this period, the N-S asymmetry shifts from Northern predominance in 2019 to near symmetry in 2020, and then to Southern predominance in 2021, illustrating the N-S asymmetry on annual scale.

In addition to these yearly observations, we also examine monthly variations in the KDE distribution of the latitude of coronal off-limb structures for the year 2018, as shown in Figure 5.7(b). It is notable that the N-S asymmetry also fluctuates throughout the months within a single year. Initially, during the first four months, activity predominates in the Southern hemisphere, before shifting to the Northern hemisphere in the following four months. By the final four months of 2018, this N-S asymmetry nearly vanishes, as the maxima of activity in both hemispheres reach similar levels. This four-month alternating period has also been observed in other years (see Bourgeois et al. 2024b for details on the monthly distribution of coronal off-limb structures throughout 2021). It appears to align closely with the Rieger period of approximately 158 days, which has been observed in various solar phenomena, such as solar flares and sunspots (Rieger et al. 1984). The Rieger period indicates the presence of medium-term periodicities in solar activity that are not accounted for by the broader solar cycle of approximately 11 years. The global solar dynamo and the modulation of magnetic fields within the convection zone by Rossby waves — these large-scale waves induced by the Coriolis effect and influenced by differential rotation — are believed to play a significant role in this periodicity (Dimitropoulou et al. 2008), which, in turn, seems to manifest in the N-S asymmetry within the latitudinal distribution of coronal off-limb structures.

The monthly distributions of other years during SC 24 exhibit a similar trend but with varying asymmetries. Some years may display a more pronounced Northern-dominance or Southern-dominance asymmetry; for instance, 2021 clearly shows a predominance of coronal activity in the Southern hemisphere, interrupted by a brief period of slight Northern predominance (see Bourgeois et al. 2024a). These month-to-month fluctuations are notable. They illustrate the intricate short-term distribution of coronal off-limb structures across hemispheres and are thus important for understanding and forecasting coronal behaviour. When one hemisphere experiences higher activity, solar eruptions are more likely to occur in that area, which can differentially affect space weather conditions on Earth and for satellites in orbit.

The N-S asymmetry is well documented in the literature, though interpretations can sometimes be conflicting. For instance, while Figure 5.6 suggests a Northern-dominant asymmetry in the distribution of coronal features during SC 24 — a pattern supported by similar findings in daily sunspot numbers (Chandra et al. 2022) — other studies present a more Southern-dominant asymmetry, such as in the distribution of coronal jets during SC 24 (Liu et al. 2023). Contradictions also arise in observations of other solar cycles. For example, Hao et al. 2015 reported a Southern-dominant asymmetry during SC 22 and a Northern-dominant asymmetry during SC 23 in filament activity, while Chandra et al. 2022 observed a predominance of sunspot activity in the Southern hemisphere for both SCs 22 and 23. Li et al. 2009 and Chandra Joshi et al. 2009 also found a Southern dominance in sunspot and prominence activity for SC 23. These inconsistencies stem, in part, from the different approaches and methods applied in each study. In our study, for instance, long-lived coronal structures (lasting more than three hours) can be counted multiple times, a limitation also noted in Hao et al. 2015's analysis of filaments. This can introduce biases, especially when compared with studies that account for each feature separately, such as Liu et al. 2023's algorithm for identifying coronal jets. Furthermore, these studies focus on distinct solar features, observed at various scales and in different layers of the solar atmosphere, which may behave differently in terms of N-S asymmetry due to localised effects. The N-S asymmetry shown in Figures 5.6 and 5.7 should therefore be interpreted with caution, as it also depends on the parameters used in this study. Assessing the statistical significance of the N-S asymmetry remains challenging, as noted by Carbonell et al. 2007.

5.8 Intensity trends

In this section, we explore the intensity trends of coronal off-limb structures as they evolve across both latitude and time. Analysing these intensity patterns is essential for understanding how coronal features develop and change throughout the solar cycle. However, it is important to consider here the potential impact of CCD deterioration (see Section 5.6), as it may affect the accuracy of the recorded intensities over time.

The intensity distribution of coronal off-limb structures is displayed in Figure 5.8, where the intensity of each feature is indicated by the colour bar, ranging from 10^3 to 10^6 DN on a logarithmic scale. This scaling helps to

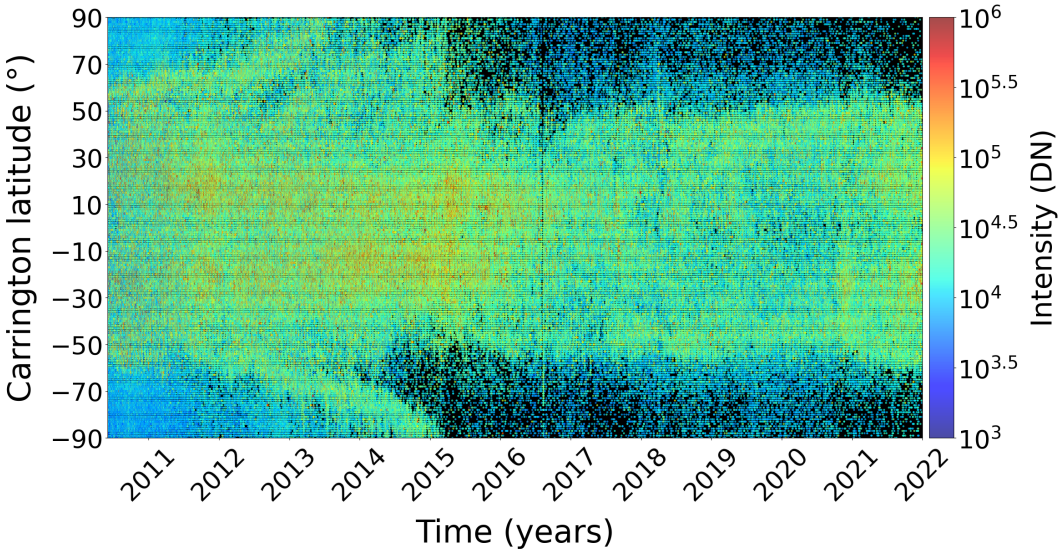

Figure 5.8: Latitude of coronal off-limb structures distributed as a function of time over SC 24. The intensity of the structures is represented by the colour bar based on a logarithmic scale, enhancing the visualisation of the intensity distribution. The colour gradient ranges from blue for lower intensities to red for higher intensities. Structures appearing red (approximately $10^5/10^6$ DN) clearly reveal the butterfly diagram pattern. Those appearing green (around $10^{4.5}$ DN) illustrate the "rush-to-the-poles" phenomenon observed between 2010 and 2015. During this period, the Northern hemisphere experienced several surges, with the first surge beginning earlier than that in the Southern hemisphere. Source: Bourgeois et al. 2024b.

highlight trends among features with a wide range of intensity levels. The high-intensity coronal off limb structures ($\sim 10^6$ DN), shown in red, clearly trace the wings of the butterfly diagram. Indeed, these features migrate from latitudes of approximately $20°/30°$ downwards and $-30°/-20°$ upwards toward the equator as the solar cycle approaches its peak, reached in 2014, and then nearly vanish during the declining phase. They begin to reemerge slightly around the mid-latitudes at the start of the next cycle, aligning with the butterfly diagram pattern.

In contrast, lower-intensity coronal structures do not show this migration pattern as distinctly, presenting a more complex and intriguing distribution. Low-intensity ($\sim 10^3$ DN) and medium-intensity structures ($\sim 10^{4.5}$ DN) continue to appear significantly throughout the descending phase of SC 24. These lower-intensity structures also tend to emerge at higher latitudes and nearer the solar poles, particularly during the rising phase, suggesting that different dynamics or formation mechanisms may be at play compared to their

higher-intensity counterparts — unless this pattern is primarily driven by the effects of CCD degradation.

The medium-intensity coronal off-limb structures, shown in green, indicate the migration of elongated structures from high-latitude regions toward the solar poles in both hemispheres prior to the magnetic field reversal around the solar maximum. This phenomenon, commonly referred to as the "rush-to-the-poles" (Lockyer 1931; Hyder 1965; Diercke et al. 2024), is clearly visible in Figure 5.8. It has also been observed in the latitudinal distributions of solar filaments (Diercke et al. 2024), prominences (Zhang et al. 2024), and even in simulation data with the distribution of flux ropes (Yeates 2013). It is noteworthy that the "rush-to-the-poles" is observable in coronal structures of moderate intensity, rather than in those with higher intensity.

The "rush-to-the-poles" phenomenon also reflects the N-S asymmetry. Indeed, in the Southern hemisphere, the "rush-to-the-poles" begins later, in 2012, compared to 2010 in the Northern hemisphere, revealing a two-year offset between hemispheres. This hemispheric difference is consistent with Zhang et al. 2024's study on active regions and prominences, which found that the peak number of these structures occurred two years earlier in the Northern hemisphere (2011) than in the Southern hemisphere (2013). Additionally, the "rush-to-the-poles" in the Northern hemisphere experiences multiple surges, unlike the smoother progression observed in the Southern hemisphere. This pattern was also noted by Gopalswamy et al. 2016, who identified several surges in the Northern hemisphere's latitudinal distribution of prominences.

A closer examination of the distribution of coronal off-limb structures across latitudes, when categorised by intensity, is provided in Figure 5.9 with a histogram using 11 bins. Coronal structures are grouped into three intensity categories, as indicated in the legend: blue represents structures with intensities below $20,000$ DN ($388,936$ structures), orange represents those between $20,000$ and $55,000$ DN ($280,513$ structures), and green represents structures with intensities above $55,000$ DN ($208,394$ structures). Once again, the active latitude belts are obvious, consistent with the butterfly diagram pattern around $20°$ and $-20°$ latitude. All intensity categories follow this trend, forming a double-peaked Gaussian-like distribution. However, lower-intensity structures (blue) display a broader Gaussian distribution, with a higher concentration of these structures at latitudes above $50°$ and below $-50°$, particularly near the poles, when compared to the higher-intensity categories (orange and green).

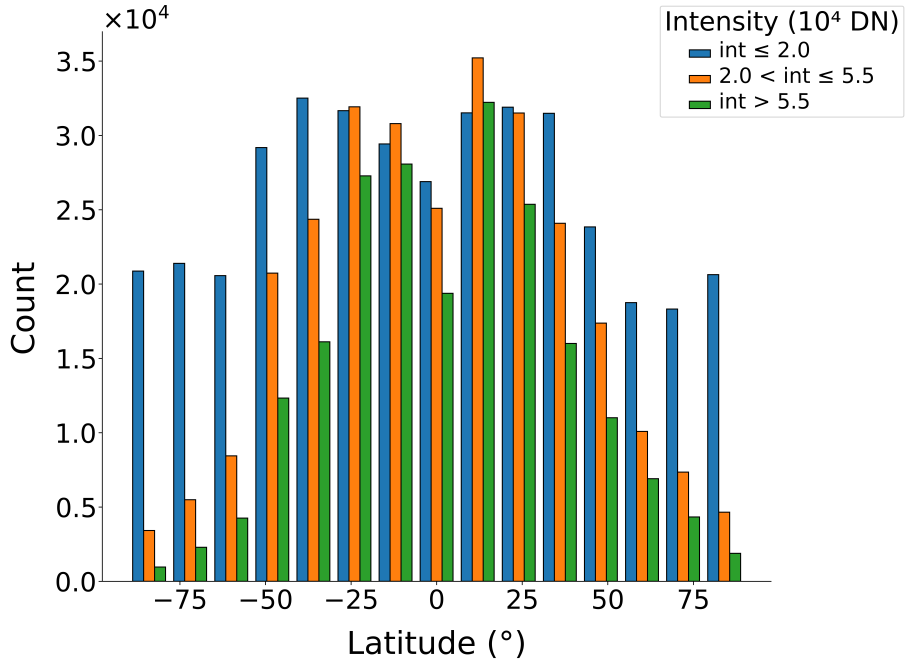

Figure 5.9: Number of coronal off-limb structures observed over SC 24, distributed by latitude in 11 bins. The structures are categorised based on their intensity values: those with an intensity lower than 20,000 DN are represented in blue (388,936 structures), those with intensities between 20,000 and 55,000 DN are displayed in orange (280,513 structures), and those with intensities exceeding 55,000 DN are shown in green (208,394 structures). Source: Bourgeois et al. 2024b.

Similar findings were reported by Soós et al. 2024 for polar jets. They found that polar jets tend to be smaller, less intense, but more numerous than those at lower latitudes. Likewise, small-scale coronal events may follow this pattern of high density and low intensity in polar and high-latitude regions, although this behaviour could also be influenced by CCD degradation.

Indeed, the impact of CCD deterioration is noticeable in Figure 5.10, which presents a histogram showing the time distribution of coronal off-limb structures, grouped by the same intensity categories as in Figure 5.9 (blue for lower-intensity structures, orange for medium-intensity, and green for high-intensity). Notably, a peculiar and pronounced peak in the number of lower-intensity features stands out in 2010, likely a result of CCD degradation. In that year, the SDO spacecraft had just begun operations and was still able to capture fainter features. Figure 5.10 also highlights the differing trends between lower-intensity and higher-intensity structures. While the declining phase of

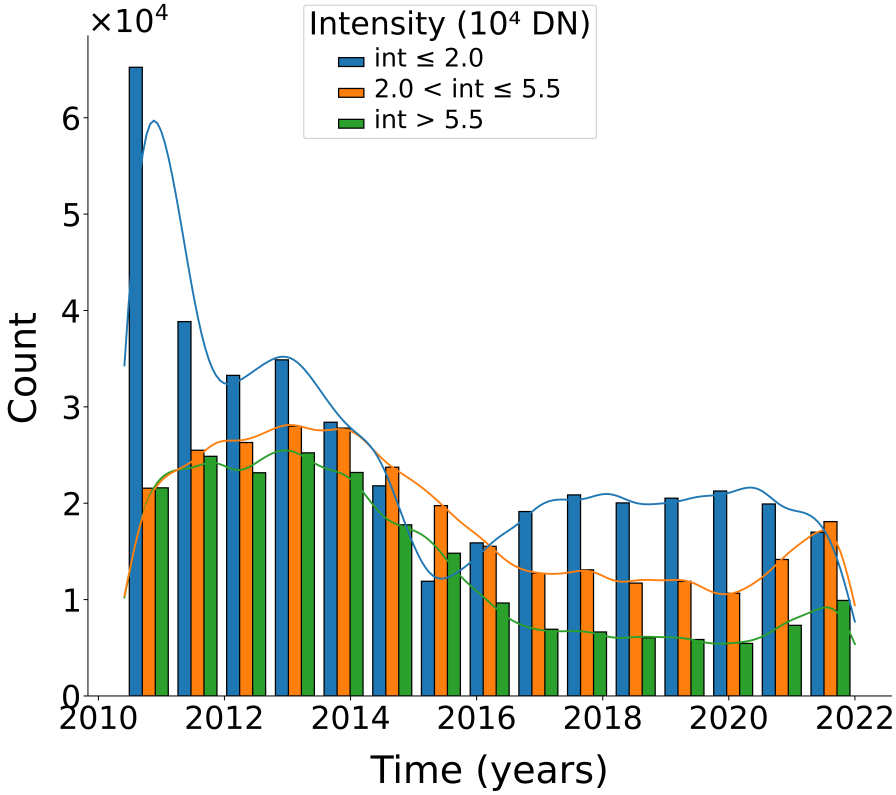

Figure 5.10: Number of coronal off-limb structures observed over SC 24, distributed over time in 11 bins. Similar to Figure 5.9, the structures are categorised into three intensity categories: blue for intensities less than 20,000 DN, orange for intensities between 20,000 and 55,000 DN, and green for intensities greater than 55,000 DN. Source: Bourgeois et al. 2024b.

SC 24 (approximately from 2015 to 2019) is marked by the expected decrease in medium- and high-intensity features, the number of low-intensity structures unexpectedly rises significantly after 2015 and remains stable, as also seen in Figure 5.8.

This unusual increase in certain solar structures based on properties such as intensity or area during the descending phase of the solar cycle has been documented in previous studies. For instance, Zhang et al. 2024 observed this trend in prominences: while the number of large-area prominences (with a projected area larger than 4.10^3 Mm^2) decreased during the decaying phase of SC 24, the number of smaller-area prominences increased during the same period. In contrast, we did not observe similar trends in area for coronal off-limb structures. Since only the intensity behaviour of these structures differs, it

may be attributed to CCD degradation. This complicates interpretation — especially given our lack of detailed knowledge about the types of structures and their evolutionary stages within each intensity group.

5.9 Longitudinal activity

In the following section, we explore the longitudinal distribution of coronal off-limb structures in order to gather evidence supporting the existence of active longitudes. This investigation raises several important questions: Does the longitudinal distribution of these structures mirror their latitudinal distribution, which features a broad zone of intensified activity (between 0° and 30° latitude) evolving with the variations of the solar cycle? What are the characteristics of these active longitudes in terms of their number, location, and lifespan? Furthermore, do we observe the "flip-flop" effect, which manifests as a shift in dominant activity between active longitudes every few years? This effect was initially detected in the longitudinal distribution of starspots on other stars (Jetsu et al. 1991; Elstner et al. 2005).

Previous studies have indeed identified inhomogeneities in the longitudinal distributions of solar features, often observed in two preferred clusters located roughly 180° apart, commonly referred to as "active longitudes" or "activity nests" in the literature (Chidambara Aiyar 1932; Dodson et al. 1968; Bogart 1982; Bai 1987; Jetsu et al. 1993, 1997; Bumba et al. 2000; Mordvinov et al. 2004; Vernova et al. 2004). Active longitude belts have been detected not only on the Sun but also on other stars (Berdyugina et al. 2002; Lanza et al. 2009). These belts tend to remain relatively stable, typically located within a range of 20° to 60° over the span of 10 to 15 Carrington rotations (Bumba et al. 1969; Castenmiller et al. 1986; Toma et al. 2000; Gyenge et al. 2016; Kostyuchenko et al. 2024). For example, Plyusnina 2010 reported a positional dispersion of 26° from one cycle to the next across 10 solar cycles.

However, beyond this period of 10 to 15 Carrington rotations, active longitudes may become less detectable or disappear altogether, raising questions about their long-term existence. For instance, Pelt et al. 2005 challenged the bimodal pattern in the longitudinal distribution of sunspots found by Berdyugina et al. 2003, attributing it to potential biases in data processing. Despite such debates, the existence of active longitudes is generally accepted within the solar community, though their underlying causes and observable

characteristics (e.g., number, location, lifespan) remain contested (Berdyugina et al. 2003). Active longitudes may persist for several months or even years (typically around 10 to 15 Carrington rotations) before disappearing and reappearing after variable periods of time, sometimes in different locations, which hinders their accurate detection and analysis.

Active longitudes have been detected across the longitudinal distributions of various solar phenomena, including sunspots (Berdyugina et al. 2003), active regions (Gyenge et al. 2012), CMEs (Skirgiello 2005; Gyenge et al. 2017), solar flares (Bumba et al. 1969; Heras et al. 1990; Mordvinov et al. 2002; Zhang et al. 2007; Zhang et al. 2008; Gyenge et al. 2016), the interplanetary magnetic field (Neugebauer et al. 2000), and coronal streamers (Li 2011). In this section, we specifically analyse the longitudinal distribution of coronal off-limb structures, aiming to uncover patterns and behaviours associated with active longitudes.

Given the substantial amount of data in our dataset, we set to examine the longitudinal distribution of coronal off-limb structures on a monthly basis rather than annually. Analysing yearly data, coupled with the effects of differential rotation, would obscure the distribution trends. Figure 5.11(a) displays the monthly distribution of the longitude of coronal off-limb structures (measured at their central coordinates) in 2018, i.e., at the end of the decaying phase of SC 24, one year before the onset of the next cycle. Each row corresponds to one month, with row 1 representing January and row 12 representing December 2018.

Distinct peaks are visible for almost every month, frequently separated by 180°, a pattern also noted in other studies (Chidambara Aiyar 1932; Bogart 1982; Bai 1987; Heras et al. 1990; Berdyugina et al. 2003; Zhang et al. 2007; Plyusnina 2010; Gyenge et al. 2012; Liu et al. 2023). For example, in January 2018 (row 1), there are two peaks around 80° and 260°; in March (row 3), around 180° and 360°; in April (row 4), around 160° and 340°; in May (row 5), around 90° and 280°; in June (row 6), around 45° and 225°; in August (row 8), around 160° and 340°; in September (row 9), around 90° and 270°; in October (row 10), around 40° and 250°; in November (row 11), at 0°, 180°, and 360°; and in December (row 12), around 160° and 340°. Perhaps the most notable instance is in July (row 7), with peaks around 0°, 180°, and 360°.

In parallel to the N-S asymmetry noted in the latitudinal distribution of coronal off-limb structures (see Figure 5.7), we also observe an East-West (E-W) asymmetry in their longitudinal distribution. In some months, peaks appear

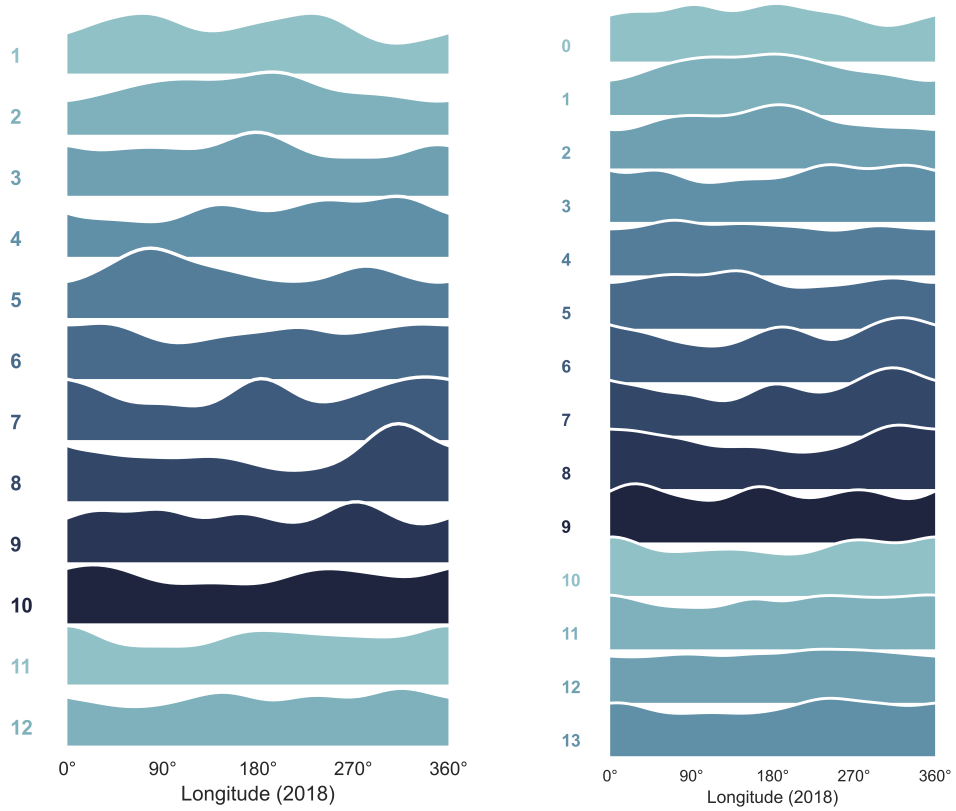

(a) Monthly distribution of coronal off-limb structures per longitude throughout the year 2018 (row 1 represents January; row 12 represents December). Each month, one to three peaks in preferred longitudes are observed, often spaced about 180° apart. Interestingly, these peaks gradually shift from month to month.

(b) 27-day distribution of coronal off-limb structures per longitude throughout the year 2018 (for example, row 1 represents the first 27 days of the year). This 27-day period corresponds to Bartels' rotation, reflecting the Sun's apparent rotation as observed from Earth. Longitudinal peaks and troughs are evident, indicating preferred and disfavoured longitudinal zones of coronal features; however, these peaks are less regular and well-defined than those in Figure 5.11(a) due to the absence of bias introduced by the monthly partitioning.

Figure 5.11: Monthly and 27-day (in 2018) distributions of coronal off-limb structures per longitude. These distributions reveal distinct patterns, highlighting the bias introduced by the monthly distribution compared to the 27-day period distribution.

at markedly different height levels at opposite heliographic longitudes. For example, in March (row 3), the peak at 180° is higher than that at 360°; in

April (row 4), the peak at 160° is smaller than the one at 340°; in May (row 5), the peak at 100° is significantly higher than the peak at 280°; in August (row 8), the peak at 160° is significantly smaller than that at 340°; and in September (row 9), the peak at 90° is smaller than the one at 270°.

Figure 5.11(a) also shows longitudinal shifts of the peaks over the months. For instance, a clear progressive displacement of the peak location is evident when following the peak in row 1 at 260° moving to approximately 200° in row 2, then to 180° in row 3, 160° in row 4, around 100° in row 5, 45° in row 6, and finally to 0° in row 7 (and possibly row 8). Another diagonal shift is visible, transitioning from 360° in row 3 to 180° in row 7, and a further shift from 360° in rows 6–7 to 160° in row 12. The gradual movement of these peaks suggests that they shift at an almost constant rate, indicating that this monthly distribution is also skewed. Given that the Carrington rotation occurs approximately every 27 days, certain longitudinal zones are counted twice within a single month. This bias progressively propagates over time, producing recurring peaks that shift almost consistently from month to month. In an ideal scenario with a uniform distribution, the shift would be perfectly consistent; however, in this case, the distribution is not uniform, introducing slight variations in the shifting pattern.

Hence, we opted to examine the longitudinal behaviour of coronal off-limb structures over a 27-day timeframe, as shown in Figure 5.11(b), which aligns with Bartels' rotation — accounting for the Sun's apparent rotation as seen from Earth. The resulting distribution in Figure 5.11(b) reveals significant differences compared to Figure 5.11(a). The peaks observed in the monthly distribution of coronal off-limb structures in Figure 5.11(a) differ in the 27-day distribution, particularly with the 180° separation between active longitudes becoming less distinct in Figure 5.11(b). However, while the peaks appear more sporadically in Figure 5.11(b), they are still present — albeit at distances that may be closer together or farther apart than the expected 180°. For instance, in rows 6 and 7, peaks occur at 0°, 180°, and 340°, with the latter two peaks closer together and farther from the first. In row 9, peaks are observed at 20°, 180°, and 290°, again showing a smaller separation than 180°. Meanwhile, row 8 shows two widely spaced peaks at 0° and 340°, while rows 0, 1, and 2 display two peaks located very close to each other. Thus, although the 180° separation between peaks is not evident in Figure 5.11(b), clear peaks and troughs in the longitudinal distribution of coronal off-limb structures still suggest the

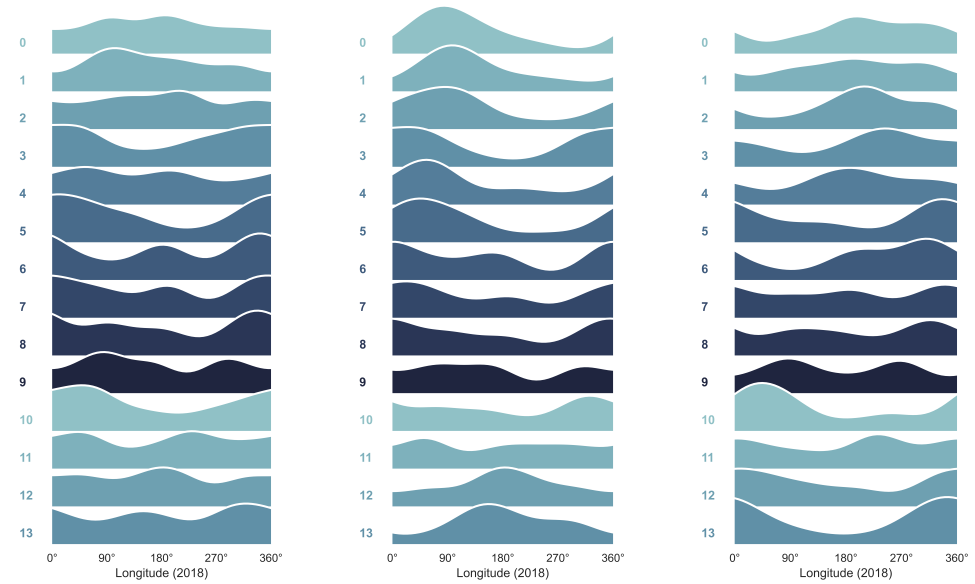

(a) 27-day longitudinal distribution of coronal off-limb structures at both latitude belts of 35°/45° and −45°/ − 35°.

(b) 27-day longitudinal distribution of coronal off-limb structures at the latitude belt of 35°/45° (Northern hemisphere).

(c) 27-day longitudinal distribution of coronal off-limb structures at the latitude belt of −45°/ − 35° (Southern hemisphere).

Figure 5.12: 27-day distribution of coronal off-limb structures per longitude in 2018 at different latitude belts corresponding to this 27-day rotation period. Panel a) shows the longitudinal distribution centred on 40° latitude in the Northern hemisphere and −40° in the Southern hemisphere, within a 10° range. Panel b) focuses on the longitudinal distribution in the Northern hemisphere only (+40° ± 5°), while panel c) examines the longitudinal distribution in the Southern hemisphere (−40° ± 5°). These latitude belts are specifically selected as they rotate at approximately a 27-day period, unlike higher latitude belts, which rotate more slowly, or lower latitude belts, which rotate more quickly.

existence of preferred longitudinal belts and quieter regions with lower coronal activity.

The lack of a consistent 180° separation can be attributed to the effects of differential rotation and fluctuations in solar activity across different latitude bands (Usoskin et al. 2007). When investigating the longitudinal distribution of coronal structures, it is important to account for the varying rotation rates of different latitude bands, which should align with the selected period for the distribution. For example, latitudinal regions around −40° in the Southern hemisphere and +40° in the Northern hemisphere follow the Carrington rotation

period of approximately 27 days. In contrast, the equatorial zone rotates with a 25-day period, while the solar poles rotate at around 35 days. This differential rotation may cause a displacement of the same active longitudes across these different latitude bands.

To account for this, Figure 5.12 presents the 27-day distribution of the longitude of coronal off-limb structures in 2018, focusing on latitude bands that rotate at roughly a 27-day period. Figure 5.12(a) shows the distribution for a 10° band centred around ±40°. Figure 5.12(b) focuses on a 10° band centred around +40° in the Northern hemisphere, while a 10° band centred around −40° in the Southern hemisphere is used in Figure 5.12(c). We chose to plot the longitudinal distribution separately for each hemisphere in Figures 5.12(b) and 5.12(c), as this allows us to observe the effects of the N-S asymmetry on the distribution. Moreover, we noticed that using latitude belts with widths ranging from 5° to 10° does not significantly alter the longitudinal characteristics of the distribution. As an example, we present here the results using a 10° latitude belt.

In Figure 5.12, active longitudes are distinctly visible, often displaying two or three peaks that migrate over time. These peaks are frequently separated by approximately 180°, as seen in rows 6, 7, 12, and 13, where prominent peaks occur around 0°, 180°, and 360°; in row 9, with peaks at 90° and 270°; and in row 11, where peaks are observed around 70° and 250°. In other rows, some peaks are either farther apart, as in rows 3, 5, and 10, or closer together, as in rows 0 and 4. Compared to Figure 5.11(b), active (and quiet) longitude belts are now much more discernible when considering latitude bands that rotate at the distribution period. While some longitudinal peaks shift over time, others remain stable across several periods. For instance, a peak consistently appears around 0° and 360° from row 3 to row 13, while other peaks persist for only one or two rotations, such as the peak at 180° in rows 6 and 7, which reappears later around 180° in rows 11 to 13. Notably, these peaks are not always of equal height, indicating an E-W asymmetry: some active longitudes tend to display more coronal activity than their counterparts located 180° apart. For example, in rows 6 and 7, the peaks at 0° and 360° are higher than the middle peak at 180°; this is contrary to row 12, where the middle peak at 180° is the highest. Such predominance of coronal activity in one active longitude compared to its counterpart at 180° illustrates the "flip-flop" phenomenon, where leading activity nests oscillate between active longitude belts. This dynamic behaviour

reflects the intricate nature of coronal off-limb structures and their underlying magnetic processes.

It is noteworthy that coronal activity in both hemispheres from Figures 5.12(b) and 5.12(c) is complementary, jointly contributing to the distribution seen in Figure 5.12(a). However, this contribution is not always equal across hemispheres and varies over time, influenced by the N-S asymmetry observed in Figure 5.7(b). In Figure 5.7(b), we saw that coronal activity predominates in the Southern hemisphere early in the year, shifts toward the Northern hemisphere mid-year, and becomes more balanced toward year's end. Observing this N-S asymmetry in the distribution of active longitudes, as also reported by Mordvinov et al. 2004; Berdyugina et al. 2006; Zhang et al. 2011, may provide insights into the mechanisms behind their formation. In particular, Dikpati et al. 2005, 2018, 2020 emphasised the role of (quasi-) stationary Rossby waves in generating active longitudes. These waves, coupled with toroidal fields in the tahocline and subject to differential rotation-induced instabilities, could lead to magnetic flux emergence in favoured longitudinal zones (Gaizauskas et al. 1983).

The origin of active longitudes indeed appears to be linked to modulations of the global mean magnetic field by a non-axisymmetric background field interacting with axisymmetric dynamo modes (Mordvinov et al. 2002; Kitchatinov et al. 2005; Jiang et al. 2007; Olemskoy et al. 2009; Raphaldini et al. 2023). Further evidence of this dynamo connection is presented by Canfield et al. 1998; Pevtsov et al. 1999; Pevtsov et al. 2003, who found that magnetic structures in active longitude belts often contradict the hemispheric helicity rule. This rule typically holds that active regions in the Northern hemisphere display left-handed (negative) helicity (i.e., magnetic field lines twist counterclockwise), while those in the Southern hemisphere show right-handed (positive) helicity (i.e., field lines twist clockwise). However, active longitudes may contain structures with reversed helicity — right-handed in the Northern hemisphere and left-handed in the Southern hemisphere — leading to interactions between structures of opposite helicity within localised areas. These interactions can result in magnetic reconnection and shearing, which may create a conducive environment for solar eruptions, such as flares and CMEs. Active longitudes are thus characterised as highly dynamic sites of concentrated flux, perpetually moving and stirring, with considerable magnetic complexity.

Interestingly, Figures 5.12(b) and 5.12(c) reveal opposite locations for

active longitudes in their respective hemispheres. For instance, in rows 0 to 5, active longitudes in the Northern hemisphere are found between 0° and 180°, while in the Southern hemisphere, longitudinal peaks are located between 180° and 360°. In rows 12 and 13, there are two clear peaks at 0° and 360° longitude in the Southern hemisphere (at the −40° latitude belt), whereas a peak is observed around 180° longitude in the Northern hemisphere (at the 40° latitude belt). This configuration results in three peaks appearing in rows 12 and 13 of Figure 5.12(a) at these longitudes. Further interesting patterns emerge in row 10, where Figure 5.12(b) shows a peak around 340° longitude in the Northern hemisphere, while Figure 5.12(c) indicates a peak around 70° longitude in the Southern hemisphere. This leads to the presence of two peaks at these longitudes in row 10 of Figure 5.12(a). Similarly, in row 11 of Figure 5.12(b), a peak appears around 45° longitude in the Northern hemisphere, while a peak occurs around 250° longitude in the Southern hemisphere (Figure 5.12(c)), resulting in two peaks at these longitudes in row 11 of Figure 5.12(a). These observations suggest that an increase in coronal off-limb structures at a specific longitude band in one hemisphere may correspond to a decrease in the opposite hemisphere along the same longitude band. This is particularly intriguing, as it implies that opposing active longitudes can manifest in different hemispheres, potentially explaining the "flip-flop" effect as a consequence of the N-S asymmetry. As discussed in Section 5.7, the N-S asymmetry can vary over solar cycles, as well as on annual and monthly timescales, causing the active longitude in the more active hemisphere to dominate over that of the less active hemisphere.

To draw a comparison, we plotted the distribution of the longitude of coronal off-limb structures in the equatorial zone in Figure 5.13, using a 25-day period corresponding to the rotation rate of this zone. Figure 5.13(a) showcases this 25-day distribution over a 10° latitude band centred around the equator at 0°. Figure 5.13(b) highlights the latitude belt between 0° and 5° in the Northern hemisphere, while Figure 5.13(c) depicts the longitudinal distribution within the latitude belt spanning from −5° to 0° in the Southern hemisphere. With the distribution confined to a small range around the equator, the N-S asymmetry is much less apparent compared to Figure 5.12. Consequently, Figures 5.13(a), 5.13(b), and 5.13(c) appear very similar, with prominent peaks occurring at approximately the same locations in each distribution; for example, a notable peak around 340° is visible from rows 3 to 9 in all three figures.

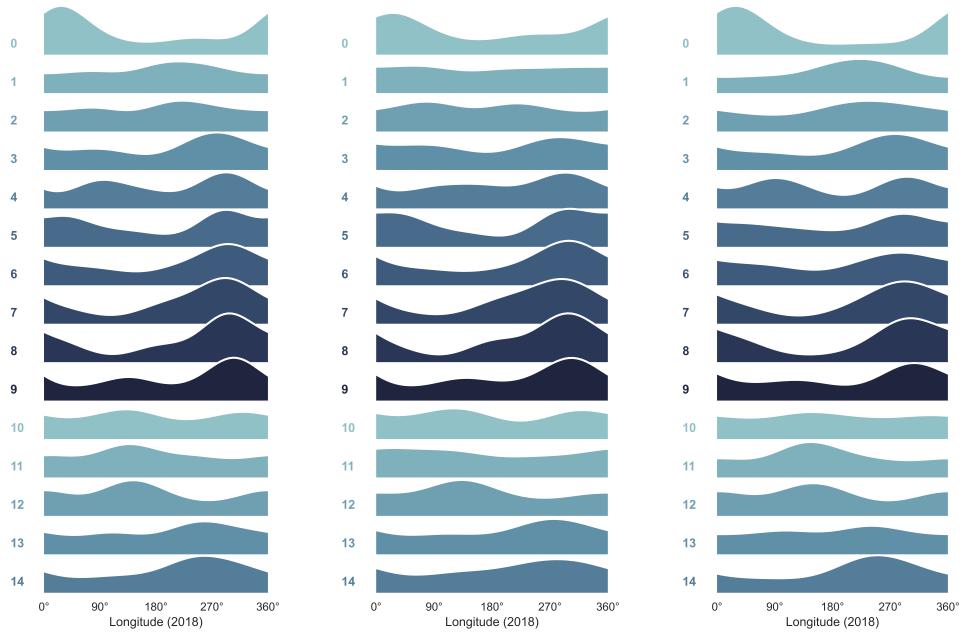

(a) 25-day longitudinal distribution of coronal off-limb structures at the latitude belt of ±5°.

(b) 25-day longitudinal distribution of coronal off-limb structures at the latitude belt of 0°/5°.

(c) 25-day longitudinal distribution of coronal off-limb structures at the latitude belt of −5°/0°.

Figure 5.13: 25-day distribution of coronal off-limb structures per longitude in 2018 at different latitude belts corresponding to this 25-day rotation period. Panel a) shows the longitudinal distribution centred at 0° latitude, within a 10° range; panel b) focuses on the Northern hemisphere only (0° to 5°), and panel c) on the Southern hemisphere (−5° to 0°). These latitude belts are selected because they rotate at approximately a 25-day period, in contrast to Figure 5.12, where mid-latitude bands centred around 40° and −40° rotate with a 27-day period.

A significant displacement of the active longitudes is observed. One peak emerges at approximately 0° in row 0, then rapidly migrates along the following rows, reaching row 4, where it settles between 270° and 360° and remains until row 9. Another shift occurs from rows 10 to 12, as the main peak appears at longitudes between 90° and 180°, before ultimately shifting to around 270° in rows 13 and 14. Although the 180° separation between peaks is less visible here (except in certain rows, such as row 4), the active longitude bands stand out, marked by high peaks. This pattern provides evidence of longitudinal inhomogeneities in coronal activity and supports the existence of active longitudes.

5.10 Concluding remarks

The identification of coronal off-limb structures using MM algorithms applied to SDO/AIA 304 Å images during SC 24 enabled detailed statistical analyses of their properties. This study not only confirmed expected latitudinal concentrations but also uncovered longitudinal patterns, revealing the existence of favoured longitude belts, termed active longitudes. After analysing monthly and 27-day distributions across the entire dataset, it became clear that differential rotation across latitudes must be accounted for when examining longitudinal distributions.

Specifically, plotting the 27-day longitudinal distribution centred around $+40^\circ$ and -40° within a 10° latitude band, as well as the 25-day distribution centred around the equator, confirmed the presence of active longitudes. These active longitudes migrate over time and often appear approximately 180° apart. When latitude bands farther from the equator were studied independently for the Northern and Southern hemispheres (e.g., the $+40^\circ$ and -40° latitude bands), a clear North-South asymmetry emerged, evident in the alternating occurrence of active longitudes between hemispheres. This phenomenon may also contribute to explaining the East-West asymmetry, or "flip-flop" effect.

These findings thus reveal a longitudinal pattern akin to the butterfly diagram for latitudinal distribution, offering significant implications for space weather forecasting. Identifying longitudinal regions of heightened coronal activity could enhance prediction accuracy. The dataset could also be used to correlate the properties of coronal off-limb structures with the characteristics of space weather phenomena, such as their frequency and magnitude, as well as to compare these results with studies from previous solar cycles for deeper historical insights. Furthermore, enriching the dataset by classifying structures through cross-referencing with other datasets of specific coronal features (e.g., coronal loops or prominences) could further advance its utility for space weather forecasting.

Chapter 6

Conclusion and Outlook

Space weather forecasting is becoming increasingly critical as society grows more reliant on technological systems that are vulnerable to solar eruptions. Strong solar storms have already impacted various technologies, but the potential for even larger events, akin to or exceeding those observed in the past — before the advent of modern infrastructure — poses a significant risk. Such events could disrupt numerous sectors and, in extreme cases, threaten the structure of modern society.

To predict and understand space weather, it is crucial to identify precursors of solar activity, which manifest as diverse features across the different layers of the Sun's atmosphere. Capturing these features requires a combination of instruments operating from both ground-based and space-based platforms, spanning a wide range of wavelengths. The vast and ever-growing volume of data generated by these instruments, particularly by spacecraft, has now outpaced the capacity for manual analysis, necessitating the use of automated processing techniques to fully exploit these datasets.

In this context, the MM approach developed and applied in this thesis (see Chapter 2) has proven to be particularly effective. It offers a robust and efficient means of processing large-scale solar data, enabling more precise analysis of solar activity and its implications for space weather forecasting.

This thesis first explored the application of MM to sunspot detection using satellite images from SDO, demonstrating high robustness by delivering results comparable to those obtained through manual methods, which are more subjective and time-intensive (see Chapter 3). This achievement is significant, as sunspots are essential indicators of solar activity. In particular, accurate

and automated measurements of sunspot areas and configurations are needed, given that the magnitude of solar eruptions is strongly correlated with the size and complexity of these features.

In addition to high-resolution SDO data, the MM algorithms successfully detected sunspots in lower-resolution images from ground-based observatories, including OGAUC and CAO. They also identified solar faculae in chromospheric images from both ground-based and space-borne observatories (see Chapter 2), features that are crucial for characterising active regions on the Sun. This highlights the versatility of the MM approach, which can adapt to a variety of datasets and image resolutions.

Beyond observational data, MM algorithms were also applied to simulation outputs, specifically twist number maps derived from the TMFM (see Chapter 4). This led to improvements over the methodology previously used by Wagner et al. 2023a for extracting magnetic flux rope structures, offering enhanced characterisation of their morphology and propagation. Since magnetic flux ropes are frequently embedded in CMEs and often serve as precursors to these eruptions, their early identification provides a valuable tool for predicting CMEs with greater lead time, a critical step toward improving space weather preparedness.

Finally, the application of MM algorithms to SDO/AIA 304 Å images over SC 24 enabled the identification of coronal off-limb structures and the creation of a large dataset documenting these features and their properties (see Chapter 5). This dataset provides valuable insights into the spatial distribution of coronal structures, uncovering patterns such as the butterfly diagram for higher-intensity coronal off-limb structures in terms of their latitudinal distribution. Furthermore, it offers new evidence supporting the existence of active longitude belts — longitudinal regions where coronal activity tends to concentrate, influenced by latitude and differential rotation. The observed N-S asymmetry highlights hemispheric differences in the longitudinal distribution of coronal activity, with offset behaviour between the hemispheres and alternating zones of localised activity within each. This dataset, therefore, opens pathways for enhancing understanding of coronal activity behaviour by identifying regions of heightened solar activity.

The MM approach has proven to be a highly effective tool for solar feature characterisation across all layers of the solar atmosphere. It has been successfully applied to the photosphere with sunspot identification, the chromosphere

with solar faculae detection, the low corona through magnetic flux rope extraction, and the broader corona via the detection of coronal off-limb structures. Although the method operates automatically once parameters are implemented, determining the optimal parameters can be challenging. Incorporating ML techniques to automatically fine-tune these parameters, as suggested by recent studies (see Chapter 2), could provide a valuable complementary approach.

Beyond methodological advancements, access to high-resolution solar data is indispensable for improving the identification and analysis of solar features. Recently launched missions like the Parker Solar Probe or Solar Orbiter offer promising opportunities in this regard. Equally important is the expansion of ground-based observatories, which are more cost-effective and accessible, enabling continuous monitoring of solar activity. Ground-based facilities are particularly valuable for studying the chromosphere, a critical layer in addressing the long-standing mystery of atmospheric heating.

Together, advancements in both methodology and data acquisition are crucial for unravelling the complexities of solar eruptions, which remain one of the great enigmas of solar physics. These efforts will also play a pivotal role in developing more accurate space weather forecasting systems, addressing the growing societal need to mitigate the risks posed by solar storms and their impact on modern technology.

Building on the advancements made in this PhD thesis, future work will focus on further developing and refining MM algorithms and extending their application to other solar features, such as filaments and solar jets. For instance, incorporating more complex transforms, such as the watershed transform, could enable effective segmentation of these features. Identifying solar jets, in particular, may benefit from a dynamic MM approach that tracks their evolution over time, as their rising and falling motion in the Sun's atmosphere makes them difficult to distinguish using static images alone. Automating jet detection, which is currently performed manually (Soós et al. 2024), would significantly reduce time demands, and MM appears well-suited for this task as it can also process video data.

Regarding sunspot detection, the work developed in Chapter 3 of this thesis can be extended to include the segmentation of umbra and penumbra within sunspots and the classification of sunspots, particularly delta-sunspots, which are strongly associated with intense solar eruptions.

The extraction of magnetic flux ropes, as discussed in Chapter 4, could be

enhanced by employing other techniques in combination with MM, such as machine learning. Such a combination could enable the automatic fine-tuning of parameters, allowing for more robust application to diverse MFR structures across different active regions.

For the identification of coronal off-limb structures, future directions outlined in Chapter 5 include expanding the analysis to data from earlier and future solar cycles, applying the MM detection method across different SDO/AIA wavelengths, and leveraging the dataset developed in this thesis to classify specific features in conjunction with existing datasets from the literature.

By addressing these directions, future research can build upon the foundational work presented in this thesis, contributing to the broader goal of advancing solar physics and deepening our understanding of space weather phenomena.

This publication is part of the Space Weather Awareness Training Network (SWATNet) which has received funding from the European Union's Horizon 2020 research and innovation programme under the Marie Skłodowska-Curie Innovative Training Networks, Grant Agreement No 955620. The publication reflects only the author's view and does not represent the opinion of the European Commission (EC), and the EC is not responsible for any use that might be made of information contained.

Bibliography

Ahmadzadeh, Azim, Dustin J. Kempton, and Rafal A. Angryk (July 2019). "A Curated Image Parameter Data Set from the Solar Dynamics Observatory Mission". In: *The Astrophysical Journal Supplement Series* 243.1, p. 18. DOI: 10.3847/1538-4365/ab253a. URL: https://dx.doi.org/10.3847/1538-4365/ab253a.

Alazraki, G. and P. Couturier (Aug. 1971). "Solar Wind Acceleration Caused by the Gradient of Alfven Wave Pressure". In: *Astronomy and Astrophysics* 13, p. 380.

André, Ph., A. Men'shchikov, S. Bontemps, V. Könyves, F. Motte, N. Schneider, P. Didelon, V. Minier, P. Saraceno, D. Ward-Thompson, J. Di Francesco, G. White, S. Molinari, L. Testi, A. Abergel, M. Griffin, Th. Henning, P. Royer, B. Merín, R. Vavrek, M. Attard, D. Arzoumanian, C. D. Wilson, P. Ade, H. Aussel, J.-P. Baluteau, M. Benedettini, J.-Ph. Bernard, J. A. D. L. Blommaert, L. Cambrésy, P. Cox, A. Di Giorgio, P. Hargrave, M. Hennemann, M. Huang, J. Kirk, O. Krause, R. Launhardt, S. Leeks, J. Le Pennec, J. Z. Li, P. G. Martin, A. Maury, G. Olofsson, A. Omont, N. Peretto, S. Pezzuto, T. Prusti, H. Roussel, D. Russeil, M. Sauvage, B. Sibthorpe, A. Sicilia-Aguilar, L. Spinoglio, C. Waelkens, A. Woodcraft, and A. Zavagno (2010). "From filamentary clouds to prestellar cores to the stellar IMF: Initial highlights from the Herschel Gould Belt Survey***". In: *A&A* 518, p. L102. DOI: 10.1051/0004-6361/201014666. URL: https://doi.org/10.1051/0004-6361/201014666.

Andrews, M. D. (Jan. 2001). "Lasco and eit Observations of the Bastille day 2000 Solar Storm". In: *Solar Physics* 204.1/2, pp. 179–196. DOI: 10.1023/a:1014215923912. URL: https://doi.org/10.1023/a:1014215923912.

Angulo, Jesús (Jan. 2008). "A Mathematical Morphology Approach to Cell Shape Analysis". In: pp. 543–547. ISBN: 978-3-540-71991-5. DOI: 10.1007/978-3-540-71992-2_87.

Anoraganingrum, D. (1999). "Cell segmentation with median filter and mathematical morphology operation". In: *Proceedings 10th International Conference on Image Analysis and Processing*, pp. 1043–1046. DOI: 10.1109/ICIAP.1999.797734.

Aptoula, E., S. Lefèvre, and C. Collet (2006). "Mathematical morphology applied to the segmentation and classification of galaxies in multispectral images". In: *2006 14th European Signal Processing Conference*, pp. 1–5.

Armstrong, John A. and Lyndsay Fletcher (June 2019). "Fast Solar Image Classification Using Deep Learning and Its Importance for Automation in Solar Physics". In: *Solar Physics* 294.6. DOI: 10.1007/s11207-019-1473-z. URL: https://doi.org/10.1007%2Fs11207-019-1473-z.

Aschwanden, Markus (Apr. 2009). "Image Processing Techniques and Feature Recognition in Solar Physics". In: *Solar Physics* 262, pp. 235–275. DOI: 10.1007/s11207-009-9474-y.

Aschwanden, Markus J. (2004). *Physics of the Solar Corona. An Introduction.*

Aschwanden, Markus J., Amy Winebarger, David Tsiklauri, and Hardi Peter (Apr. 2007). "The Coronal Heating Paradox". In: *The Astrophysical Journal* 659.2, p. 1673. DOI: 10.1086/513070. URL: https://dx.doi.org/10.1086/513070.

Babcock, Harold D. (Sept. 1959). "The Sun's Polar Magnetic Field." In: *The Astrophysical Journal* 130, p. 364. DOI: 10.1086/146726.

Baek, Ji-Hye, Sujin Kim, Seonghwan Choi, Jongyeob Park, Jihun Kim, Wonkeun Jo, and Dongil Kim (Nov. 2021). "Solar Event Detection Using Deep-Learning-Based Object Detection Methods". In: *Solar Physics* 296.11, 160, p. 160. DOI: 10.1007/s11207-021-01902-5.

Bai, Taeil (Mar. 1987). "Distribution of Flares on the Sun: Superactive Regions and Active Zones of 1980–1985". In: *The Astrophysical Journal* 314, p. 795. DOI: 10.1086/165105.

Bain, H. M., K. Copeland, T. G. Onsager, and R. A. Steenburgh (2023). "NOAA Space Weather Prediction Center Radiation Advisories for the International Civil Aviation Organization". In: *Space Weather* 21.7. e2022SW003346 2022SW003346, e2022SW003346. DOI: https://doi.org/10.1029/2022SW003346.

Baker, D. N., X. Li, A. Pulkkinen, C. M. Ngwira, M. L. Mays, A. B. Galvin, and K. D. C. Simunac (Oct. 2013). "A major solar eruptive event in July 2012: Defining extreme space weather scenarios". In: *Space Weather* 11.10, pp. 585–591. DOI: 10.1002/swe.20097.

Ballegooijen, A. A. van, M. Asgari-Targhi, and A. Voss (Oct. 2017). "The Heating of Solar Coronal Loops by Alfvén Wave Turbulence". In: *The Astrophysical Journal* 849.1, p. 46. DOI: 10.3847/1538-4357/aa9118. URL: https://dx.doi.org/10.3847/1538-4357/aa9118.

Baranyi, T., L. Győri, and A. Ludmány (2016). *Heritage of Konkoly's Solar Observations: the Debrecen Photoheliograph Programme and the Debrecen Sunspot Databases*. arXiv: 1608.08419 [astro-ph.SR].

Barata, T., S. Carvalho, I. Dorotovic, F. Pinheiro, A. Garcia, J. Fernandes, and A. M. Lourenco (2018). "Software tool for automatic detection of solar plages in the Coimbra Observatory spectroheliograms". In: *Astronomy and Computing*. DOI: 10.48550/ARXIV.1811.08389. URL: https://arxiv.org/abs/1811.08389.

Barnes, Aaron (Jan. 1969). "Collisionless Heating of the Solar-Wind Plasma. II. Application of the Theory of Plasma Heating by Hydromagnetic Waves". In: *The Astrophysical Journal* 155, p. 311. DOI: 10.1086/149866.

Barnes, Will, Mark Cheung, Monica Bobra, Paul Boerner, Georgios Chintzoglou, Drew Leonard, Stuart Mumford, Nicholas Padmanabhan, Albert Shih, Nina Shirman, David Stansby, and Paul Wright (Nov. 2020). "aiapy: A Python Package for Analyzing Solar EUV Image Data from AIA". In: *The Journal of Open Source Software* 5.55, 2801, p. 2801. DOI: 10.21105/joss.02801.

Beckers, Jacques M. (Jan. 1972). "Solar Spicules". In: *Annual Review of Astronomy and Astrophysics* 10, p. 73. DOI: 10.1146/annurev.aa.10.090172.000445.

Belcher, J. W. (Sept. 1971). "ALFVÉNIC Wave Pressures and the Solar Wind". In: *The Astrophysical Journal* 168, p. 509. DOI: 10.1086/151105.

Benkhalil, A., V. V. Zharkova, S. Zharkov, and S. Ipson (May 2006). "Active Region Detection and Verification With the Solar Feature Catalogue". In: *Solar Physics* 235.1-2, pp. 87–106. DOI: 10.1007/s11207-006-0023-7.

Berdyugina, S. V., D. Moss, D. Sokoloff, and I. G. Usoskin (2006). "Active longitudes, nonaxisymmetric dynamos and phase mixing". In: *A&A* 445.2, pp. 703–714. DOI: 10.1051/0004-6361:20053454. URL: https://doi.org/10.1051/0004-6361:20053454.

Berdyugina, S. V., J. Pelt, and I. Tuominen (2002). "Magnetic activity in the young solar analog LQ Hydrae* - I. Active longitudes and cycles". In: *A&A* 394.2, pp. 505–515. DOI: 10.1051/0004-6361:20021179. URL: https://doi.org/10.1051/0004-6361:20021179.

Berdyugina, S. V. and I. G. Usoskin (2003). "Active longitudes in sunspot activity: Century scale persistence". In: *A&A* 405.3, pp. 1121–1128. DOI: 10.1051/0004-6361:20030748. URL: https://doi.org/10.1051/0004-6361:20030748.

Berger, Mitchell A. and Chris Prior (June 2006). "The writhe of open and closed curves". In: *Journal of Physics A Mathematical General* 39.26, pp. 8321–8348. DOI: 10.1088/0305-4470/39/26/005.

Beucher, Serge (June 1990). "Segmentation d'images et morphologie mathématique". Theses. École Nationale Supérieure des Mines de Paris. URL: https://pastel.hal.science/tel-00108290.

— (May 1999). "Mathematical morphology and geology: when image analysis uses the vocabulary of Earth Science, a review of some applications". In.

Biermann, L. (Jan. 1951). "Kometenschweife und solare Korpuskularstrahlung". In: *Zeitschrift für Astrophysik* 29, p. 274.

Biermann, L., B. Brosowski, and H. U. Schmidt (Mar. 1967). "The interactions of the solar wind with a comet". In: *Solar Physics* 1.2, pp. 254–284. DOI: 10.1007/BF00150860.

Blanter, Elena and Mikhail Shnirman (June 2021). "North-South Asymmetry of Solar Meridional Circulation and Synchronization: Two Rings of Four Coupled Oscillators". In: *Solar Physics* 296.6, 86, p. 86. DOI: 10.1007/s11207-021-01821-5.

Bogart, Richard S. (Feb. 1982). "Recurrence of solar activity: Evidence for active longitudes". In: *Solar Physics* 76.1, pp. 155–165. DOI: 10.1007/BF00214137.

Bourgeois, Slava, Teresa Barata, R. Erdélyi, Ricardo Gafeira, and Orlando Oliveira (Jan. 2024a). "Sunspots Identification Through Mathematical Morphology". In: *Solar Physics* 299. DOI: 10.1007/s11207-023-02243-1.

Bourgeois, Slava, Simone Chierichini, Sz Soós, R. Erdélyi, J. Liu, Marianna Korsós, R. Gafeira, and Teresa Barata (Dec. 2024b). "Long-term properties of coronal off-limb structures". In: *Astronomy & Astrophysics*. DOI: 10.1051/0004-6361/202451257.

Bright, David S. and Eric B. Steel (1987). "Two-dimensional top hat filter for extracting spots and spheres from digital images". In: *Journal of Microscopy*

146.2, pp. 191–200. DOI: https://doi.org/10.1111/j.1365-2818.1987.tb01340.x. eprint: https://onlinelibrary.wiley.com/doi/pdf/10.1111/j.1365-2818.1987.tb01340.x. URL: https://onlinelibrary.wiley.com/doi/abs/10.1111/j.1365-2818.1987.tb01340.x.

Bumba, V., A. Garcia, and M. Klvaňa (2000). "Longitudinal Distribution of Solar Magnetic Fields and Activity During the Ending and Starting Periods of Activity Cycles". In: *Solar Physics* 196. DOI: 10.1023/A:1005226228739.

Bumba, V. and V. N. Obridko (Jan. 1969). "'Bartels' active longitudes', sector boundaries and flare activity". In: *Solar Physics* 6.1, pp. 104–110. DOI: 10.1007/BF00146800.

Cade III, William B. and Christina Chan-Park (2015). "The Origin of "Space Weather"". In: *Space Weather* 13.2, pp. 99–103. DOI: https://doi.org/10.1002/2014SW001141. eprint: https://agupubs.onlinelibrary.wiley.com/doi/pdf/10.1002/2014SW001141. URL: https://agupubs.onlinelibrary.wiley.com/doi/abs/10.1002/2014SW001141.

Campi, Cristina, Federico Benvenuto, Anna Maria Massone, D. Shaun Bloomfield, Manolis K. Georgoulis, and Michele Piana (Sept. 2019). "Feature Ranking of Active Region Source Properties in Solar Flare Forecasting and the Uncompromised Stochasticity of Flare Occurrence". In: *The Astrophysical Journal* 883.2, p. 150. DOI: 10.3847/1538-4357/ab3c26. URL: https://doi.org/10.3847/1538-4357/ab3c26.

Camporeale, E. (2019). "The Challenge of Machine Learning in Space Weather: Nowcasting and Forecasting". In: *Space Weather* 17.8, pp. 1166–1207. DOI: https://doi.org/10.1029/2018SW002061. eprint: https://agupubs.onlinelibrary.wiley.com/doi/pdf/10.1029/2018SW002061. URL: https://agupubs.onlinelibrary.wiley.com/doi/abs/10.1029/2018SW002061.

Candéas, Alcione Jandir, Ulisses de Mendonça Braga Neto, and Edson Costa de Barros Carvalho Filho (Apr. 1997). "A Mathematical Morphology Approach to the Star/Galaxy Characterization". In: *Journal of the Brazilian Computer Society* 3.3, pp. 14–29. ISSN: 0104-6500. DOI: 10.1590/S0104-65001997000100002.

Canfield, Richard C. and Alexei A. Pevtsov (Jan. 1998). "Helicity of Solar Active-Region Magnetic Fields". In: *Synoptic Solar Physics*. Ed. by K. S. Balasubramaniam, Jack Harvey, and D. Rabin. Vol. 140. Astronomical Society of the Pacific Conference Series, p. 131.

Carbonell, M., J. Terradas, R. Oliver, and J. L. Ballester (2007). "The statistical significance of the North-South asymmetry of solar activity revisited". In: *Astronomy and Astrophysics* 476.2, pp. 951–957. DOI: 10.1051/0004-6361:20078004. URL: https://doi.org/10.1051/0004-6361:20078004.

Carrasco, Víctor Manuel Sánchez and José Manuel Vaquero (2020). "Portuguese eyewitness accounts of the great space weather event of 1582". In: *J. Space Weather Space Clim.* 10, p. 4. DOI: 10.1051/swsc/2020005. URL: https://doi.org/10.1051/swsc/2020005.

Carrington, R. C. (Nov. 1859). "Description of a Singular Appearance seen in the Sun on September 1, 1859". In: *Monthly Notices of the Royal Astronomical Society* 20.1, pp. 13–15. ISSN: 0035-8711. DOI: 10.1093/mnras/20.1.13. eprint: https://academic.oup.com/mnras/article-pdf/20/1/13/3059054/mnras20-0013.pdf. URL: https://doi.org/10.1093/mnras/20.1.13.

Carvalho, S., S. Gomes, T. Barata, A. Lourenço, and N. Peixinho (2020). "Comparison of automatic methods to detect sunspots in the Coimbra Observatory spectroheliograms". In: *Astronomy and Computing* 32, p. 100385. ISSN: 2213-1337. DOI: https://doi.org/10.1016/j.ascom.2020.100385. URL: https://www.sciencedirect.com/science/article/pii/S2213133720300391.

Castenmiller, M. J. M., C. Zwaan, and E. B. J. van der Zalm (June 1986). "Sunspot Nests - Manifestations of Sequences in Magnetic Activity". In: *Solar Physics* 105.2, pp. 237–255. DOI: 10.1007/BF00172045.

Chamberlin, Phillip, William Dean Pesnell, and Barbara Thompson (2012). *The Solar Dynamics Observatory*. Springer New York, NY. DOI: https://doi.org/10.1007/978-1-4614-3673-7.

Chandra, Y., B. Pande, M. C. Mathpal, and S. Pande (Sept. 2022). "N-S Asymmetry and Periodicity of Daily Sunspot Number During Solar Cycles 22-24". In: *Astrophysics* 65.3, pp. 404–413. DOI: 10.1007/s10511-022-09749-9.

Chandra Joshi, Navin, Neeraj Bankoti, Seema Pande, Bimal Pande, and Kavita Pandey (July 2009). "Study of Distribution and Asymmetry of Solar Active Prominences During Solar Cycle 23". In: *Solar Physics* 260. DOI: 10.1007/s11207-009-9446-2.

Chaturvedi, Rajan and Dr. Naresh Kumar Chaudhary (2019). "Mathematical Morphology and Medical Image Processing". In: *IOSR Journal of Engineering*.

Chen, Shengyong, Mingzhu Zhao, Guang Wu, Chunyan Yao, and Jianwei Zhang (Jan. 2012). "Recent Advances in Morphological Cell Image Analysis". In: *Computational and mathematical methods in medicine* 2012, p. 101536. DOI: 10.1155/2012/101536.

Cheung, Mark C. M. and Marc L. DeRosa (Sept. 2012). "A METHOD FOR DATA-DRIVEN SIMULATIONS OF EVOLVING SOLAR ACTIVE REGIONS". In: *The Astrophysical Journal* 757.2, p. 147. DOI: 10.1088/0004-637X/757/2/147. URL: https://dx.doi.org/10.1088/0004-637X/757/2/147.

Chidambara Aiyar, P. R. (Dec. 1932). "Two Longitudinal Zones of Apparent Inhibition of Sunspots on the Solar Disc". In: *Monthly Notices of the Royal Astronomical Society* 93.2, pp. 150–151. ISSN: 0035-8711. DOI: 10.1093/mnras/93.2.150. eprint: https://academic.oup.com/mnras/article-pdf/93/2/150/3311540/mnras93-0150.pdf. URL: https://doi.org/10.1093/mnras/93.2.150.

Chola, Channabasava and J V Biabl Benifa (2022). "Detection and classification of sunspots via deep convolutional neural network". In: *Global Transitions Proceedings* 3.1. International Conference on Intelligent Engineering Approach(ICIEA-2022), pp. 177–182. ISSN: 2666-285X. DOI: https://doi.org/10.1016/j.gltp.2022.03.006. URL: https://www.sciencedirect.com/science/article/pii/S2666285X22000103.

Cliver, Edward W. and William F. Dietrich (2013). "The 1859 space weather event revisited: limits of extreme activity". In: *J. Space Weather Space Clim.* 3, A31. DOI: 10.1051/swsc/2013053. URL: https://doi.org/10.1051/swsc/2013053.

Community, The SunPy, Will T. Barnes, Monica G. Bobra, Steven D. Christe, Nabil Freij, Laura A. Hayes, Jack Ireland, Stuart Mumford, David Perez-Suarez, Daniel F. Ryan, Albert Y. Shih, (Primary Paper Contributors), Prateek Chanda, Kolja Glogowski, Russell Hewett, V. Keith Hughitt, Andrew Hill, Kaustubh Hiware, Andrew Inglis, Michael S. F. Kirk, Sudarshan Konge, James Paul Mason, Shane Anthony Maloney, Sophie A. Murray, Asish Panda, Jongyeob Park, Tiago M. D. Pereira, Kevin Reardon, Sabrina Savage, Brigitta M. Sipőcz, David Stansby, Yash Jain, Garrison Taylor,

Tannmay Yadav, Rajul, Trung Kien Dang, and (Sunpy Contributors) (Feb. 2020). "The SunPy Project: Open Source Development and Status of the Version 1.0 Core Package". In: *The Astrophysical Journal* 890.1, p. 68. DOI: 10.3847/1538-4357/ab4f7a. URL: https://dx.doi.org/10.3847/1538-4357/ab4f7a.

Coster, Michel and Jean-Louis Chermant (Apr. 2001). "Image analysis and mathematical morphology for civil engineering materials". In: *Cement and Concrete Composites* 23, pp. 133–151. DOI: 10.1016/S0958-9465(00)00058-5.

Couvidat, S., J. Schou, J. T. Hoeksema, R. S. Bogart, R. I. Bush, T. L. Duvall, Y. Liu, A. A. Norton, and P. H. Scherrer (Aug. 2016). "Observables processing for the Helioseismic and Magnetic Imager instrument on the Solar Dynamics Observatory". In: *Solar Physics* 291.7, pp. 1887–1938. DOI: 10.1007/s11207-016-0957-3. arXiv: 1606.02368 [astro-ph.SR].

Curto, Juan, M. Blanca, and E. Martínez (Jan. 2008). "Automatic Sunspots Detection on Full-Disk Solar Images using Mathematical Morphology". In: *Solar Physics* 250, pp. 411–429. DOI: 10.1007/s11207-008-9224-6.

Davidson, Jennifer L. and Gerhard X. Ritter (July 1990). "Theory of morphological neural networks". In: *Digital Optical Computing II*. Ed. by Raymond Arrathoon. Vol. 1215. Society of Photo-Optical Instrumentation Engineers (SPIE) Conference Series, pp. 378–388. DOI: 10.1117/12.18085.

De Pontieu, Bart, Robert Erdélyi, and Stewart P. James (July 2004). "Solar chromospheric spicules from the leakage of photospheric oscillations and flows". In: *Nature* 430.6999, pp. 536–539. DOI: 10.1038/nature02749.

Démoulin, P., E. R. Priest, and D. P. Lonie (Apr. 1996). "Three-dimensional magnetic reconnection without null points 2. Application to twisted flux tubes". In: *Journal of Geophysical Research (Space Physics)* 101.A4, pp. 7631–7646. DOI: 10.1029/95JA03558.

Derivaux, Sébastien, Sébastien Lefèvre, Cédric Wemmert, and Jerzy Korczak (Sept. 2007). "On Machine Learning in Watershed Segmentation". In: pp. 187–192. ISBN: 978-1-4244-1566-3. DOI: 10.1109/MLSP.2007.4414304.

Devkota, B., Abeer Alsadoon, P.W.C. Prasad, A.K. Singh, and A. Elchouemi (2018). "Image Segmentation for Early Stage Brain Tumor Detection using Mathematical Morphological Reconstruction". In: *Procedia Computer Science* 125. The 6th International Conference on Smart Computing and

Communications, pp. 115–123. ISSN: 1877-0509. DOI: https://doi.org/10.1016/j.procs.2017.12.017.

Diercke, Andrea, Robert Jarolim, Christoph Kuckein, Sergio J. González Manrique, Marco Ziener, Astrid M. Veronig, Carsten Denker, Werner Pötzi, Tatiana Podladchikova, and Alexei A. Pevtsov (2024). *A Universal Method for Solar Filament Detection from H-alpha Observations using Semi-supervised Deep Learning*. arXiv: 2402.15407 [astro-ph.SR].

Dikpati, Mausumi and Peter A. Gilman (Dec. 2005). "A Shallow-Water Theory for the Sun's Active Longitudes". In: *The Astrophysical Journal* 635.2, p. L193. DOI: 10.1086/499626. URL: https://dx.doi.org/10.1086/499626.

Dikpati, Mausumi and Scott W. McIntosh (2020). "Space Weather Challenge and Forecasting Implications of Rossby Waves". In: *Space Weather* 18.3. e2018SW002109 2018SW002109, e2018SW002109. DOI: https://doi.org/10.1029/2018SW002109. eprint: https://agupubs.onlinelibrary.wiley.com/doi/pdf/10.1029/2018SW002109. URL: https://agupubs.onlinelibrary.wiley.com/doi/abs/10.1029/2018SW002109.

Dikpati, Mausumi, Scott W. McIntosh, Gregory Bothun, Paul S. Cally, Siddhartha S. Ghosh, Peter A. Gilman, and Orkan M. Umurhan (Feb. 2018). "Role of Interaction between Magnetic Rossby Waves and Tachocline Differential Rotation in Producing Solar Seasons". In: *The Astrophysical Journal* 853.2, p. 144. DOI: 10.3847/1538-4357/aaa70d. URL: https://dx.doi.org/10.3847/1538-4357/aaa70d.

Dimitropoulou, M., X. Moussas, and D. Strintzi (Apr. 2008). "Enhanced Rieger-type periodicities' detection in X-ray solar flares and statistical validation of Rossby waves' existence". In: *Monthly Notices of the Royal Astronomical Society* 386.4, pp. 2278–2284. ISSN: 0035-8711. DOI: 10.1111/j.1365-2966.2008.13203.x. eprint: https://academic.oup.com/mnras/article-pdf/386/4/2278/4282785/mnras0386-2278.pdf. URL: https://doi.org/10.1111/j.1365-2966.2008.13203.x.

Dodson, Helen W. and E. Ruth Hedeman (1968). "Some Patterns in the Development of Centers of Solar Activity, 1962–66". In: *Structure and Development of Solar Active Regions*. Dordrecht: Springer Netherlands, pp. 56–63. ISBN: 978-94-011-6815-1. DOI: 10.1007/978-94-011-6815-1_9. URL: https://doi.org/10.1007/978-94-011-6815-1_9.

Dong, Pinliang (1997). "Implementation of mathematical morphological operations for spatial data processing". In: *Computers & Geosciences* 23.1, pp. 103–107. ISSN: 0098-3004. DOI: https://doi.org/10.1016/S0098-3004(96)00065-9. URL: https://www.sciencedirect.com/science/article/pii/S0098300496000659.

Dramdahl, M. Kirbie (2014). "Morphological Operations Applied to Digital Art Restoration". In: *Scholarly Horizons: University of Minnesota, Morris Undergraduate Journal*. DOI: 10.61366/2576-2176.1011.

Dryer, M., Z. Smith, C. D. Fry, W. Sun, C. S. Deehr, and S.-I. Akasofu (2004). "Real-time shock arrival predictions during the "Halloween 2003 epoch"". In: *Space Weather* 2.9. DOI: https://doi.org/10.1029/2004SW000087. eprint: https://agupubs.onlinelibrary.wiley.com/doi/pdf/10.1029/2004SW000087. URL: https://agupubs.onlinelibrary.wiley.com/doi/abs/10.1029/2004SW000087.

Eastwood, J. P., E. Biffis, M. A. Hapgood, L. Green, M. M. Bisi, R. D. Bentley, R. Wicks, L.-A. McKinnell, M. Gibbs, and C. Burnett (2017). "The Economic Impact of Space Weather: Where Do We Stand?" In: *Risk Analysis* 37.2, pp. 206–218. DOI: https://doi.org/10.1111/risa.12765. eprint: https://onlinelibrary.wiley.com/doi/pdf/10.1111/risa.12765. URL: https://onlinelibrary.wiley.com/doi/abs/10.1111/risa.12765.

Elstner, D. and H. Korhonen (Apr. 2005). "Flip-flop phenomenon: observations and theory". In: *Astronomische Nachrichten* 326.3, pp. 278–282. DOI: 10.1002/asna.200410389. arXiv: astro-ph/0501343 [astro-ph].

Erdélyi, Robertus, Marianna B. Korsós, Xin Huang, Yong Yang, Danielle Pizzey, Steven A. Wrathmall, Hughes, Ifan G., Dyer, Martin J., Dhillon, Vikram S., Belucz, Bernadett, Brajsa, Roman, Chatterjee, Piyali, Cheng, Xuewu, Deng, Yuanyong, Domínguez, Santiago Vargas, Joya, Raúl, Gömöry, Peter, Gyenge, Norbert G., Hanslmeier, Arnold, Kucera, Ales, Kuridze, David, Li, Faquan, Liu, Zhong, Xu, Long, Mathioudakis, Mihalis, Matthews, Sarah, McAteer, James R.T., Pevtsov, Alexei A., Pötzi, Werner, Romano, Paolo, Shen, Jinhua, Temesváry, János, Tlatov, Andrey G., Triana, Charles, Utz, Dominik, Veronig, Astrid M., Wang, Yuming, Yan, Yihua, Zaqarashvili, Teimuraz, and Zuccarello, Francesca (2022). "The Solar Activity Monitor Network - SAMNet". In: *J. Space Weather Space Clim.* 12, p. 2. DOI: 10.1051/swsc/2021025. URL: https://doi.org/10.1051/swsc/2021025.

Firoz, Raihan, Md Ali, Md. Nasir Uddin Khan, M. Khalid Hossain, M. Islam, and M. Shahinuzzaman (Feb. 2016). "Medical Image Enhancement Using Morphological Transformation". In: *Journal of Data Analysis and Information Processing* 4, pp. 1–12. DOI: 10.4236/jdaip.2016.41001.

Franchi, Gianni, Amin Fehri, and Angela Yao (June 2020). "Deep morphological networks". In: *Pattern Recognition* 102, p. 107246. DOI: 10.1016/j.patcog.2020.107246. URL: https://hal.archives-ouvertes.fr/hal-02922299.

Fuller, Nicolas, Jean Aboudarham, and R. D. Bentley (Mar. 2005). "Filament Recognition and Image Cleaning on Meudon Hα Spectroheliograms". In: *Solar Physics* 227.1, pp. 61–73. DOI: 10.1007/s11207-005-8364-1.

Gaizauskas, V., K. L. Harvey, J. W. Harvey, and C. Zwaan (Feb. 1983). "Large-scale patterns formed by solar active regions during the ascending phase of cycle 21". In: *The Astrophysical Journal* 265, pp. 1056–1065. DOI: 10.1086/160747.

Gaona, Isidro Ramón, Julio Cesar Mello-Román, José Luis Vázquez Noguera, Horacio Legal-Ayala, Julieta Méndez, Sebastián Grillo, and Silvia Vázquez Noguera (2023). "Enhanced medical images through multi-scale mathematical morphology by reconstruction". In: *2023 18th Iberian Conference on Information Systems and Technologies (CISTI)*, pp. 1–5. DOI: 10.23919/CISTI58278.2023.10211680.

Gavankar, Nitin L. and Sanjay Kumar Ghosh (2018). "Automatic building footprint extraction from high-resolution satellite image using mathematical morphology". In: *European Journal of Remote Sensing* 51.1, pp. 182–193. DOI: 10.1080/22797254.2017.1416676. eprint: https://doi.org/10.1080/22797254.2017.1416676. URL: https://doi.org/10.1080/22797254.2017.1416676.

Georgoulis, Manolis K., Bloomfield, D. Shaun, Piana, Michele, Massone, Anna Maria, Soldati, Marco, Gallagher, Peter T., Pariat, Etienne, Vilmer, Nicole, Buchlin, Eric, Baudin, Frederic, Csillaghy, Andre, Sathiapal, Hanna, Jackson, David R., Alingery, Pablo, Benvenuto, Federico, Campi, Cristina, Florios, Konstantinos, Gontikakis, Constantinos, Guennou, Chloe, Guerra, Jordan A., Kontogiannis, Ioannis, Latorre, Vittorio, Murray, Sophie A., Park, Sung-Hong, von Stachelski, Samuel, Torbica, Aleksandar, Vischi, Dario, and Worsfold, Mark (2021). "The flare likelihood and region eruption forecasting (FLARECAST) project: flare forecasting in the big data &

machine learning era". In: *J. Space Weather Space Clim.* 11, p. 39. DOI: 10.1051/swsc/2021023. URL: https://doi.org/10.1051/swsc/2021023.

Géron, Aurélien (2017). *Hands-on machine learning with Scikit-Learn and TensorFlow : concepts, tools, and techniques to build intelligent systems.* O'Reilly Media. ISBN: 978-1491962299.

González-Avilés, J J, F S Guzmán, V Fedun, G Verth, R Sharma, S Shelyag, and S Regnier (Jan. 2019). "In situ generation of coronal Alfvén waves by jets". In: *Monthly Notices of the Royal Astronomical Society* 484.2, pp. 1936–1945. ISSN: 0035-8711. DOI: 10.1093/mnras/stz087. eprint: https://academic.oup.com/mnras/article-pdf/484/2/1936/27603887/stz087.pdf. URL: https://doi.org/10.1093/mnras/stz087.

Gopalswamy, Nat, Seiji Yashiro, and Sachiko Akiyama (May 2016). "Unusual polar conditions in Solar Cycle 24 and their implications for Solar Cycle 25". In: *The Astrophysical Journal Letters* 823.1, p. L15. DOI: 10.3847/2041-8205/823/1/L15. URL: https://dx.doi.org/10.3847/2041-8205/823/1/L15.

Grant, Samuel D. T., David B. Jess, Teimuraz V. Zaqarashvili, Christian Beck, Hector Socas-Navarro, Markus J. Aschwanden, Peter H. Keys, Damian J. Christian, Scott J. Houston, and Rebecca L. Hewitt (Mar. 2018). "Alfvén wave dissipation in the solar chromosphere". In: *Nature Physics* 14.5, pp. 480–483. ISSN: 1745-2481. DOI: 10.1038/s41567-018-0058-3. URL: http://dx.doi.org/10.1038/s41567-018-0058-3.

Green, L. M., S. A. Matthews, L. van Driel-Gesztelyi, L. K. Harra, and J. L. Culhane (Feb. 2002). "Multi-wavelength observations of an X-class flare without a coronal mass ejection." In: *Solar Physics* 205.2, pp. 325–339. DOI: 10.1023/A:1014211528863.

Green, Lucie M., Tibor Török, Bojan Vršnak, Ward Manchester, and Astrid Veronig (Feb. 2018). "The Origin, Early Evolution and Predictability of Solar Eruptions". In: *Space Science Reviews* 214.1, 46, p. 46. DOI: 10.1007/s11214-017-0462-5. arXiv: 1801.04608 [astro-ph.SR].

Gyenge, N., T. Baranyi, and A. Ludmány (Jan. 2012). "Distribution of activity at the solar active longitudes between 1979 - 2011 in the northern hemisphere". In: *Central European Astrophysical Bulletin* 36, pp. 9–16.

Gyenge, N., A. Ludmány, and T. Baranyi (Feb. 2016). "Active longitude and solar flare occurrences". In: *The Astrophysical Journal* 818.2, p. 127.

ISSN: 1538-4357. DOI: 10.3847/0004-637x/818/2/127. URL: http://dx.doi.org/10.3847/0004-637X/818/2/127.

Gyenge, N., T. Singh, T. S. Kiss, A. K. Srivastava, and R. Erdélyi (Mar. 2017). "Active Longitude and Coronal Mass Ejection Occurrences". In: *The Astrophysical Journal* 838.1, p. 18. DOI: 10.3847/1538-4357/aa62a8. URL: https://dx.doi.org/10.3847/1538-4357/aa62a8.

Győri, L., A. Ludmány, and T. Baranyi (Feb. 2017). "Comparative analysis of Debrecen sunspot catalogues". In: *Monthly Notices of the Royal Astronomical Society* 465.2, pp. 1259–1273. DOI: 10.1093/mnras/stw2667. URL: https://doi.org/10.1093%2Fmnras%2Fstw2667.

Haas, A, G Matheron, and J Serra (1967). "Morphologie mathématique et granulométries en place: Annales Mines, v. 11". In: *1967b, Morphologie mathématique et granulométries en place: Annales Mines* 12, pp. 767–782.

Halberstadt, G. and J. P. Goedbloed (Sept. 1995). "Alfven wave heating of coronal loops: photospheric excitation." In: *Astronomy and Astrophysics* 301, p. 559.

Han, Lili, Yimin Tian, and Qianhui Qi (2020). "Research on edge detection algorithm based on improved sobel operator". In: *MATEC Web Conf.* 309, p. 03031. DOI: 10.1051/matecconf/202030903031. URL: https://doi.org/10.1051/matecconf/202030903031.

Hanaoka, Yoichiro (2022). *Automated Sunspot Detection as an Alternative to Visual Observations*. DOI: 10.48550/ARXIV.2211.13552. URL: https://arxiv.org/abs/2211.13552.

Hao, Q., C. Fang, W. Cao, and P. F. Chen (Dec. 2015). "Statistical analysis of filament features based on the Hα solar images from 1988 to 2013 by computer automated detection method". In: *The Astrophysical Journal Supplement Series* 221.2, p. 33. DOI: 10.1088/0067-0049/221/2/33. URL: https://dx.doi.org/10.1088/0067-0049/221/2/33.

Haralick, R.M. (1988). "Mathematical Morphology And Computer Vision". In: *Twenty-Second Asilomar Conference on Signals, Systems and Computers.* Vol. 1, pp. 468–479. DOI: 10.1109/ACSSC.1988.754039.

Harvey, Paul M., Cassandra Fallscheer, Adam Ginsburg, Susan Terebey, Philippe André, Tyler L. Bourke, James Di Francesco, Vera Könyves, Brenda C. Matthews, and Dawn E. Peterson (Jan. 2013). "A first look at the Auriga-California giant molecular cloud with Hershel* and the CSO: Census of the young stellar objects and the dense gas". In: *The Astrophys-*

ical Journal 764.2, p. 133. DOI: 10.1088/0004-637X/764/2/133. URL: https://dx.doi.org/10.1088/0004-637X/764/2/133.

Hassan, Gehad, Nashwa El-Bendary, Aboul Ella Hassanien, Ali Fahmy, Shoeb Abullah M., and Vaclav Snasel (2015). "Retinal Blood Vessel Segmentation Approach Based on Mathematical Morphology". In: *Procedia Computer Science* 65. International Conference on Communications, management, and Information technology (ICCMIT'2015), pp. 612–622. ISSN: 1877-0509. DOI: https://doi.org/10.1016/j.procs.2015.09.005. URL: https://www.sciencedirect.com/science/article/pii/S1877050915028355.

Hathaway, David H (2010). "The Solar Cycle". In: *Living Reviews in Solar Physics* 7. DOI: 10.12942/lrsp-2010-1. URL: https://doi.org/10.12942/lrsp-2010-1.

Hattori, Kentaro, Hisashi Hayakawa, and Yusuke Ebihara (Aug. 2019). "Occurrence of great magnetic storms on 6-8 March 1582". In: *Monthly Notices of the Royal Astronomical Society* 487.3, pp. 3550–3559. DOI: 10.1093/mnras/stz1401. arXiv: 1905.08017 [astro-ph.SR].

Hayakawa, Hisashi, Edward W. Cliver, Frédéric Clette, Yusuke Ebihara, Shin Toriumi, Ilaria Ermolli, Theodosios Chatzistergos, Kentaro Hattori, Delores J. Knipp, Séan P. Blake, Gianna Cauzzi, Kevin Reardon, Philippe-A. Bourdin, Dorothea Just, Mikhail Vokhmyanin, Keitaro Matsumoto, Yoshizumi Miyoshi, José R. Ribeiro, Ana P. Correia, David M. Willis, Matthew N. Wild, and Sam M. Silverman (Dec. 2023). "The Extreme Space Weather Event of 1872 February: Sunspots, Magnetic Disturbance, and Auroral Displays". In: *The Astrophysical Journal* 959.1, p. 23. DOI: 10.3847/1538-4357/acc6cc. URL: https://dx.doi.org/10.3847/1538-4357/acc6cc.

Hayakawa, Hisashi, Yusuke Ebihara, José M. Vaquero, Kentaro Hattori, Víctor M. S. Carrasco, María de la Cruz Gallego, Satoshi Hayakawa, Yoshikazu Watanabe, Kiyomi Iwahashi, Harufumi Tamazawa, Akito D. Kawamura, and Hiroaki Isobe (2018). "A great space weather event in February 1730". In: *A&A* 616, A177. DOI: 10.1051/0004-6361/201832735. URL: https://doi.org/10.1051/0004-6361/201832735.

Hayakawa, Hisashi, Kentaro Hattori, Alexei A. Pevtsov, Yusuke Ebihara, Margaret A. Shea, Ken G. McCracken, Ioannis A. Daglis, Ankush T. Bhaskar, Paulo Ribeiro, and Delores J. Knipp (Mar. 2021). "The Intensity and Evolution of the Extreme Solar and Geomagnetic Storms in 1938

January". In: *The Astrophysical Journal* 909.2, p. 197. DOI: 10.3847/1538-4357/abc427. URL: https://dx.doi.org/10.3847/1538-4357/abc427.

Hayakawa, Hisashi, Kiyomi Iwahashi, Yusuke Ebihara, Harufumi Tamazawa, Kazunari Shibata, Delores J. Knipp, Akito D. Kawamura, Kentaro Hattori, Kumiko Mase, Ichiro Nakanishi, and Hiroaki Isobe (Nov. 2017). "Long-lasting Extreme Magnetic Storm Activities in 1770 Found in Historical Documents". In: *The Astrophysical Journal Letters* 850.2, p. L31. DOI: 10.3847/2041-8213/aa9661. URL: https://dx.doi.org/10.3847/2041-8213/aa9661.

Hayakawa, Hisashi, Paulo Ribeiro, José M. Vaquero, María Cruz Gallego, Delores J. Knipp, Florian Mekhaldi, Ankush Bhaskar, Denny M. Oliveira, Yuta Notsu, Víctor M. S. Carrasco, Ana Caccavari, Bhaskara Veenadhari, Shyamoli Mukherjee, and Yusuke Ebihara (July 2020). "The Extreme Space Weather Event in 1903 October/November: An Outburst from the Quiet Sun". In: *The Astrophysical Journal Letters* 897.1, L10, p. L10. DOI: 10.3847/2041-8213/ab6a18. arXiv: 2001.04575 [astro-ph.SR].

Heijmans, Henk J. A. M. (1995). "Mathematical Morphology: A Modern Approach in Image Processing Based on Algebra and Geometry". In: *SIAM Review* 37.1, pp. 1–36. DOI: 10.1137/1037001. eprint: https://doi.org/10.1137/1037001. URL: https://doi.org/10.1137/1037001.

Heras, A. M., B. Sanahuja, M. A. Shea, and D. F. Smart (Apr. 1990). "Some comments on the east-west solar flare distribution during the 1976 1985 period". In: *Solar Physics* 126.2, pp. 371–383. DOI: 10.1007/BF00153057.

Hirata, Nina S. T. and George A. Papakostas (2021). "On Machine-Learning Morphological Image Operators". In: *Mathematics* 9.16. ISSN: 2227-7390. DOI: 10.3390/math9161854. URL: https://www.mdpi.com/2227-7390/9/16/1854.

Hodgson, R. (Nov. 1859). "On a curious Appearance seen in the Sun". In: *Monthly Notices of the Royal Astronomical Society* 20, pp. 15–16. DOI: 10.1093/mnras/20.1.15.

Hou, Jia-Wei, Shu-Guang Zeng, Sheng Zheng, Xiao-Yu Luo, Lin-Hua Deng, Yang-Yang Li, Yan-Qing Chen, Gang-Hua Lin, Yong-Li Feng, and Jin-Ping Tao (Aug. 2022). "Chinese Sunspot Drawings and Their Digitization—(VII) Sunspot Penumbra to Umbra Area Ratio Using the Hand-Drawing Records from Yunnan Observatories". In: *Research in Astronomy and Astrophysics*

22.9, p. 095012. DOI: 10.1088/1674-4527/ac7f87. URL: https://dx.doi.org/10.1088/1674-4527/ac7f87.

Hou, Yanli (June 2014). "Automatic Segmentation of Retinal Blood Vessels Based on Improved Multiscale Line Detection". In: *Journal of Computing Science and Engineering* 8, pp. 119–128. DOI: 10.5626/JCSE.2014.8.2.119.

Howard, R. A., D. J. Michels, Jr. Sheeley N. R., and M. J. Koomen (Dec. 1982). "The observation of a coronal transient directed at Earth." In: *The Astrophysical Journal* 263, pp. L101–L104. DOI: 10.1086/183932.

Huang, Xin, Huaning Wang, Long Xu, Jinfu Liu, Rong Li, and Xinghua Dai (Mar. 2018). "Deep Learning Based Solar Flare Forecasting Model. I. Results for Line-of-sight Magnetograms". In: *ApJ* 856.1, 7, p. 7. DOI: 10.3847/1538-4357/aaae00.

Humbe, Vikas, Shivanand Gornale, Ramesh Manza, and Karbhari Kale (Aug. 2007). "Mathematical Morphology Approach for Genuine Fingerprint Feature Extraction". In: *International Journal of Computer Science and Security* 1.

Huttunen, K. Emilia J., Hannu E. J. Koskinen, Tuija I. Pulkkinen, Antti Pulkkinen, Minna Palmroth, E. Geoffrey D. Reeves, and Howard J. Singer (2002). "April 2000 magnetic storm: Solar wind driver and magnetospheric response". In: *Journal of Geophysical Research: Space Physics* 107.A12, SMP 15-1-SMP 15–21. DOI: https://doi.org/10.1029/2001JA009154. eprint: https://agupubs.onlinelibrary.wiley.com/doi/pdf/10.1029/2001JA009154. URL: https://agupubs.onlinelibrary.wiley.com/doi/abs/10.1029/2001JA009154.

Hyder, Charles L. (Jan. 1965). "The "polar Crown" of Filaments and the Sun's Polar Magnetic Fields." In: *The Astrophysical Journal* 141, p. 272. DOI: 10.1086/148108.

Illing, R. M. E. and A. J. Hundhausen (Jan. 1985). "Observation of a coronal transient from 1.2 to 6 solar radii". In: *Journal of Geophysical Research* 90.A1, pp. 275–282. DOI: 10.1029/JA090iA01p00275.

Innes, D. E., R. Bučík, L.-J. Guo, and N. Nitta (Nov. 2016). "Observations of solar X-ray and EUV jets and their related phenomena". In: *Astronomische Nachrichten* 337.10, pp. 1024–1032. ISSN: 1521-3994. DOI: 10.1002/asna.201612428. URL: http://dx.doi.org/10.1002/asna.201612428.

Iucci, N., A. E. Levitin, A. V. Belov, E. A. Eroshenko, N. G. Ptitsyna, G. Villoresi, G. V. Chizhenkov, L. I. Dorman, L. I. Gromova, M. Parisi, M. I. Tyasto, and V. G. Yanke (2005). "Space weather conditions and spacecraft anomalies in different orbits". In: *Space Weather* 3.1. DOI: https://doi.org/10.1029/2003SW000056. eprint: https://agupubs.onlinelibrary.wiley.com/doi/pdf/10.1029/2003SW000056. URL: https://agupubs.onlinelibrary.wiley.com/doi/abs/10.1029/2003SW000056.

Iwanowski, Marcin, Slawomir Skoneczny, and Jaroslaw Szostakowski (1997). "Image features extraction using mathematical morphology". In: *Applications of Digital Image Processing XX*. Ed. by Andrew G. Tescher. Vol. 3164. International Society for Optics and Photonics. SPIE, pp. 565–572. DOI: 10.1117/12.279581. URL: https://doi.org/10.1117/12.279581.

Jacobsen, Knut Stanley and Yngvild Linnea Andalsvik (2016). "Overview of the 2015 St. Patrick's day storm and its consequences for RTK and PPP positioning in Norway". In: *J. Space Weather Space Clim.* 6, A9. DOI: 10.1051/swsc/2016004. URL: https://doi.org/10.1051/swsc/2016004.

Janardhan, P., K. Fujiki, M. Ingale, S. K. Bisoi, and D. Rout (Oct. 2018). "Solar cycle 24: An unusual polar field reversal". In: *Astronomy and Astrophysics* 618, A148, A148. DOI: 10.1051/0004-6361/201832981. arXiv: 1805.06654 [astro-ph.SR].

Jenkins, Jack M. and Rony Keppens (2022). "Resolving the solar prominence/filament paradox using the magnetic Rayleigh–Taylor instability". In: *Nature Astronomy* 6, pp. 942–950. URL: https://api.semanticscholar.org/CorpusID:250463472.

Jetsu, L., J. Pelt, and I. Tuominen (Nov. 1993). "SPOT and flare activity of FK Comae Berenices : long-term photometry." In: *Astronomy and Astrophysics* 278, pp. 449–462.

Jetsu, L., S. Pohjolainen, J. Pelt, and I. Tuominen (Feb. 1997). "Is the longitudinal distribution of solar flares nonuniform?" In: *Astronomy and Astrophysics* 318, pp. 293–307.

Jetsu, Lauri, J. Pelt, Ilkka Tuominen, and Harold Nations (Jan. 1991). "The Spot Activity of FK Comae Berenices". In: *International Astronomical Union Colloquium* 130, pp. 381–383. DOI: 10.1017/S0252921100079963.

Jeulin, D. (1989). "Some aspects of mathematical morphology for physical applications". In: *Physica A: Statistical Mechanics and its Applications*

157.1, pp. 13–20. ISSN: 0378-4371. DOI: https://doi.org/10.1016/0378-4371(89)90271-9.

Jiang, J. and J. X. Wang (Apr. 2007). "A dynamo model for axisymmetric and non-axisymmetric solar magnetic fields". In: *Monthly Notices of the Royal Astronomical Society* 377.2, pp. 711–718. ISSN: 0035-8711. DOI: 10.1111/j.1365-2966.2007.11644.x. eprint: https://academic.oup.com/mnras/article-pdf/377/2/711/3491714/mnras0377-0711.pdf. URL: https://doi.org/10.1111/j.1365-2966.2007.11644.x.

Jones, J.B.L., R.D. Bentley, R. Hunter, R.H.A. Iles, G.C. Taylor, and D.J. Thomas (2005). "Space weather and commercial airlines". In: *Advances in Space Research* 36.12. Space Weather, pp. 2258–2267. ISSN: 0273-1177. DOI: https://doi.org/10.1016/j.asr.2004.04.017. URL: https://www.sciencedirect.com/science/article/pii/S0273117705000062.

Kaiqiong, Sun, Chen Zhen, Jiang Shaofeng, and Wang Yu (2011). "Morphological Multiscale Enhancement, Fuzzy Filter and Watershed for Vascular Tree Extraction in Angiogram". In: *Journal of Medical Systems*. DOI: 10.1007/s10916-010-9466-3.

Karas, Pavel (2011). "Efficient Computation of Morphological Greyscale Reconstruction". In: *Sixth Doctoral Workshop on Mathematical and Engineering Methods in Computer Science (MEMICS'10) – Selected Papers*. Ed. by Ludek Matyska, Michal Kozubek, Tomas Vojnar, Pavel Zemcik, and David Antos. Vol. 16. Open Access Series in Informatics (OASIcs). Dagstuhl, Germany: Schloss Dagstuhl – Leibniz-Zentrum für Informatik, pp. 54–61. ISBN: 978-3-939897-22-4. DOI: 10.4230/OASIcs.MEMICS.2010.54. URL: https://drops.dagstuhl.de/entities/document/10.4230/OASIcs.MEMICS.2010.54.

Kataoka, Ryuho, Daikou Shiota, Hitoshi Fujiwara, Hidekatsu Jin, Chihiro Tao, Hiroyuki Shinagawa, and Yasunobu Miyoshi (2022). "Unexpected space weather causing the reentry of 38 Starlink satellites in February 2022". In: *J. Space Weather Space Clim.* 12, p. 41. DOI: 10.1051/swsc/2022034. URL: https://doi.org/10.1051/swsc/2022034.

Keys, P. H., A. Reid, M. Mathioudakis, S. Shelyag, V. M. J. Henriques, R. L. Hewitt, D. Del Moro, S. Jafarzadeh, D. B. Jess, and M. Stangalini (2020). "High-resolution spectropolarimetric observations of the temporal evolution of magnetic fields in photospheric bright points". In: *Astronomy*

and Astrophysics 633, A60. DOI: 10.1051/0004-6361/201936545. URL: https://doi.org/10.1051/0004-6361/201936545.

Kilpua, E. K. J., N. Lugaz, M. L. Mays, and M. Temmer (Apr. 2019). "Forecasting the Structure and Orientation of Earthbound Coronal Mass Ejections". In: *Space Weather* 17.4, pp. 498–526. DOI: 10.1029/2018SW001944.

Kimori, Yoshitaka (Dec. 2011). "Mathematical morphology-based approach to the enhancement of morphological features in medical images". In: *Journal of clinical bioinformatics* 1, p. 33. DOI: 10.1186/2043-9113-1-33.

Kitchatinov, L. L. and S. V. Olemskoi (Apr. 2005). "Active longitudes of the sun: The rotation period and statistical significances". In: *Astronomy Letters* 31.4. DOI: 10.1134/1.1896072.

Kitchatinov, Leonid and Anna Khlystova (Sept. 2021). "Dynamo Model for North–South Asymmetry of Solar Activity". In: *The Astrophysical Journal* 919.1, p. 36. DOI: 10.3847/1538-4357/ac1113. URL: https://dx.doi.org/10.3847/1538-4357/ac1113.

Knipp, D. J., A. C. Ramsay, E. D. Beard, A. L. Boright, W. B. Cade, I. M. Hewins, R. H. McFadden, W. F. Denig, L. M. Kilcommons, M. A. Shea, and D. F. Smart (2016). "The May 1967 great storm and radio disruption event: Extreme space weather and extraordinary responses". In: *Space Weather* 14.9, pp. 614–633. DOI: https://doi.org/10.1002/2016SW001423. eprint: https://agupubs.onlinelibrary.wiley.com/doi/pdf/10.1002/2016SW001423. URL: https://agupubs.onlinelibrary.wiley.com/doi/abs/10.1002/2016SW001423.

Knipp, Delores J., Brian J. Fraser, M. A. Shea, and D. F. Smart (2018). "On the Little-Known Consequences of the 4 August 1972 Ultra-Fast Coronal Mass Ejecta: Facts, Commentary, and Call to Action". In: *Space Weather* 16.11, pp. 1635–1643. DOI: https://doi.org/10.1029/2018SW002024. eprint: https://agupubs.onlinelibrary.wiley.com/doi/pdf/10.1029/2018SW002024. URL: https://agupubs.onlinelibrary.wiley.com/doi/abs/10.1029/2018SW002024.

Koch, Eric W. and Erik W. Rosolowsky (Aug. 2015). "Filament identification through mathematical morphology". In: *Monthly Notices of the Royal Astronomical Society* 452.4, pp. 3435–3450. ISSN: 0035-8711. DOI: 10.1093/mnras/stv1521. eprint: https://academic.oup.com/mnras/article-pdf/452/4/3435/18238514/stv1521.pdf. URL: https://doi.org/10.1093/mnras/stv1521.

Korsós, M. B., T. Baranyi, and A. Ludmány (July 2014). "Pre-flare dynamics of sunspot groups". In: *The Astrophysical Journal* 789.2, 107, p. 107. DOI: 10.1088/0004-637X/789/2/107. arXiv: 1405.7485 [astro-ph.SR].

Korsós, M. B., P. Chatterjee, and R. Erdélyi (Apr. 2018). "Applying the Weighted Horizontal Magnetic Gradient Method to a Simulated Flaring Active Region". In: *The Astrophysical Journal* 857.2, p. 103. DOI: 10.3847/1538-4357/aab891. URL: https://doi.org/10.3847/1538-4357/aab891.

Korsós, M. B., M. K. Georgoulis, N. Gyenge, S. K. Bisoi, S. Yu, S. Poedts, C. J. Nelson, J. Liu, Y. Yan, and R. Erdélyi (June 2020). "Solar Flare Prediction Using Magnetic Field Diagnostics above the Photosphere". In: *The Astrophysical Journal* 896.2, p. 119. DOI: 10.3847/1538-4357/ab8fa2. URL: https://dx.doi.org/10.3847/1538-4357/ab8fa2.

Korsós, M. B., N. Gyenge, T. Baranyi, and A. Ludmány (Mar. 2015a). "Dynamic Precursors of Flares in Active Region NOAA 10486". In: *Journal of Astrophysics and Astronomy* 36.1, pp. 111–121. DOI: 10.1007/s12036-015-9329-x. arXiv: 1501.07257 [astro-ph.SR].

Korsós, M. B., A. Ludmány, R. Erdélyi, and T. Baranyi (Apr. 2015b). "On flare predictability based on sunspot group evolution". In: *The Astrophysical Journal* 802.2, L21, p. L21. DOI: 10.1088/2041-8205/802/2/L21. arXiv: 1503.04634 [astro-ph.SR].

Korsós, M. B., Shuhong Yang, and Robertus Erdélyi (2019). "Investigation of pre-flare dynamics using the weighted horizontal magnetic gradient method: From small to major flare classes". In: *J. Space Weather Space Clim.* 9, A6. DOI: 10.1051/swsc/2019002. URL: https://doi.org/10.1051/swsc/2019002.

Kostyuchenko, I. G. and E. S. Vernova (Jan. 2024). "The Rotation Rate of the Active Longitude and Sunspot Groups on It and Other Characteristics of Sunspot Groups at the End of the Descending Branch of Solar Cycle 24". In: *Geomagnetism and Aeronomy* 63.8, pp. 1210–1217. DOI: 10.1134/S001679322308011X.

Koutchmy, Serge (Mar. 1988). "Space-borne coronagraphy". In: *Space Science Reviews* 47.1-2, pp. 95–143. DOI: 10.1007/BF00223238.

Lanza, A. F., I. Pagano, G. Leto, S. Messina, S. Aigrain, R. Alonso, M. Auvergne, A. Baglin, P. Barge, A. S. Bonomo, P. Boumier, A. Collier Cameron, M. Comparato, G. Cutispoto, J. R. De Medeiros, B. Foing,

A. Kaiser, C. Moutou, P. S. Parihar, A. Silva-Valio, and W. W. Weiss (2009). "Magnetic activity in the photosphere of CoRoT-Exo-2a* - Active longitudes and short-term spot cycle in a young Sun-like star". In: *A&A* 493.1, pp. 193–200. DOI: 10.1051/0004-6361:200810591. URL: https://doi.org/10.1051/0004-6361:200810591.

Lea, Suzanne M and Matthew Lybanon (1993). "Finding mesoscale ocean structures with mathematical morphology". In: *Remote Sensing of Environment* 44.1, pp. 25–33. ISSN: 0034-4257. DOI: https://doi.org/10.1016/0034-4257(93)90100-C. URL: https://www.sciencedirect.com/science/article/pii/003442579390100C.

Lea, Suzanne M., Matthew Lybanon, and Sarah H. Peckinpaugh (1996). "Water Depth Determination Using Mathematical Morphology". In: *Mathematical Morphology and its Applications to Image and Signal Processing*. Ed. by Petros Maragos, Ronald W. Schafer, and Muhammad Akmal Butt. Boston, MA: Springer US, pp. 451–458. ISBN: 978-1-4613-0469-2. DOI: 10.1007/978-1-4613-0469-2_53. URL: https://doi.org/10.1007/978-1-4613-0469-2_53.

Lemen, James R., Alan M. Title, David J. Akin, Paul F. Boerner, Catherine Chou, Jerry F. Drake, Dexter W. Duncan, Christopher G. Edwards, Frank M. Friedlaender, Gary F. Heyman, Neal E. Hurlburt, Noah L. Katz, Gary D. Kushner, Michael Levay, Russell W. Lindgren, Dnyanesh P. Mathur, Edward L. McFeaters, Sarah Mitchell, Roger A. Rehse, Carolus J. Schrijver, Larry A. Springer, Robert A. Stern, Theodore D. Tarbell, Jean-Pierre Wuelser, C. Jacob Wolfson, Carl Yanari, Jay A. Bookbinder, Peter N. Cheimets, David Caldwell, Edward E. Deluca, Richard Gates, Leon Golub, Sang Park, William A. Podgorski, Rock I. Bush, Philip H. Scherrer, Mark A. Gummin, Peter Smith, Gary Auker, Paul Jerram, Peter Pool, Regina Soufli, David L. Windt, Sarah Beardsley, Matthew Clapp, James Lang, and Nicholas Waltham (Jan. 2012). "The Atmospheric Imaging Assembly (AIA) on the Solar Dynamics Observatory (SDO)". In: *Solar Physics* 275.1-2, pp. 17–40. DOI: 10.1007/s11207-011-9776-8.

Li, Dong and David M. Long (Feb. 2023). "A Statistical Study of Short-period Decayless Oscillations of Coronal Loops in an Active Region". In: *The Astrophysical Journal* 944.1, p. 8. DOI: 10.3847/1538-4357/acacf4. URL: https://dx.doi.org/10.3847/1538-4357/acacf4.

Li, Jing (June 2011). "Active longitudes revealed by large-scale and long-lived coronal streamers". In: *The Astrophysical Journal* 735.2, p. 130. DOI: 10.1088/0004-637X/735/2/130. URL: https://dx.doi.org/10.1088/0004-637X/735/2/130.

Li, Kejun, Peng-Xin Gao, and L. Zhan (Jan. 2009). "The Long-term Behavior of the North – South Asymmetry of Sunspot Activity". In: *Solar Physics* 254, pp. 145–154. DOI: 10.1007/s11207-008-9284-7.

Ling, LI, CUI Yanmei, LIU Siqing, and LEI Lei (2020). "Automatic Detection of Sunspots and Extraction of Sunspot Characteristic Parameters". In: *Chinese Journal of Space Science* 40.20200310, p. 315. ISSN: 0254-6124. DOI: 10.11728/cjss2020.03.315. URL: https://www.cjss.ac.cn/en/article/doi/10.11728/cjss2020.03.315.

Lirui, Yang and Ding Runtao (1991). "Morphological filters with multiple structuring elements". In: *China., 1991 International Conference on Circuits and Systems*, 812–815 vol.2. DOI: 10.1109/CICCAS.1991.184485.

Liu, Jiajia, Chunyu Ji, Yimin Wang, Szabolcs Soós, Ye Jiang, Robertus Erdélyi, M. B. Korsós, and Yuming Wang (Sept. 2024). "Improving the Automated Coronal Jet Identification with U-NET". In: *The Astrophysical Journal* 972.2, p. 187. DOI: 10.3847/1538-4357/ad66be. URL: https://dx.doi.org/10.3847/1538-4357/ad66be.

Liu, Jiajia, Chris J. Nelson, Ben Snow, Yuming Wang, and Robert Erdélyi (Aug. 2019). "Evidence of ubiquitous Alfvén pulses transporting energy from the photosphere to the upper chromosphere". In: *Nature Communications* 10, 3504, p. 3504. DOI: 10.1038/s41467-019-11495-0.

Liu, Jiajia, Anchuan Song, David B. Jess, Jie Zhang, Mihalis Mathioudakis, Szabolcs Soós, Francis P. Keenan, Yuming Wang, and Robertus Erdélyi (May 2023). "Power-law Distribution of Solar Cycle–modulated Coronal Jets". In: *The Astrophysical Journal Supplement Series* 266.1, p. 17. DOI: 10.3847/1538-4365/acc85a. URL: https://dx.doi.org/10.3847/1538-4365/acc85a.

Liu, Qingsheng, Jinfa Dong, Gaohuan Liu, Chong Huang, and Chuanjie Xie (June 2011). "Using the Canny edge detector and mathematical morphology operators to detect vegetation patches". In: *Third International Conference on Digital Image Processing (ICDIP 2011)*. Ed. by Ting Zhang. Vol. 8009. Society of Photo-Optical Instrumentation Engineers (SPIE) Conference Series, 80091H, 80091H. DOI: 10.1117/12.896163.

Liu, Rui, Bernhard Kliem, Viacheslav S. Titov, Jun Chen, Yuming Wang, Haimin Wang, Chang Liu, Yan Xu, and Thomas Wiegelmann (Feb. 2016). "Structure, Stability, and Evolution of Magnetic Flux Ropes from the Perspective of Magnetic Twist". In: *The Astrophysical Journal* 818.2, 148, p. 148. DOI: 10.3847/0004-637X/818/2/148. arXiv: 1512.02338 [astro-ph.SR].

Liu, Ying D., Janet G. Luhmann, Primož Kajdič, Emilia K.J. Kilpua, Noé Lugaz, Nariaki V. Nitta, Christian Möstl, Benoit Lavraud, Stuart D. Bale, Charles J. Farrugia, and Antoinette B. Galvin (Mar. 2014). "Observations of an extreme storm in interplanetary space caused by successive coronal mass ejections". In: *Nature Communications* 5.1. ISSN: 2041-1723. DOI: 10.1038/ncomms4481. URL: http://dx.doi.org/10.1038/ncomms4481.

Lockyer, W. J. S. (May 1931). "On the relationship between solar prominences and the forms of the corona". In: *Monthly Notices of the Royal Astronomical Society* 91, p. 797. DOI: 10.1093/mnras/91.7.797.

Love, Jeffrey and Pierdavide Coïsson (Sept. 2016). "The Geomagnetic Blitz of September 1941". In: *Eos. Transactions, American Geophysical Union* 97. DOI: 10.1029/2016EO059319.

Love, Jeffrey J. (2018). "The Electric Storm of November 1882". In: *Space Weather* 16.1, pp. 37–46. DOI: https://doi.org/10.1002/2017SW001795. eprint: https://agupubs.onlinelibrary.wiley.com/doi/pdf/10.1002/2017SW001795. URL: https://agupubs.onlinelibrary.wiley.com/doi/abs/10.1002/2017SW001795.

Love, Jeffrey J., Hisashi Hayakawa, and Edward W. Cliver (2019). "Intensity and Impact of the New York Railroad Superstorm of May 1921". In: *Space Weather* 17.8, pp. 1281–1292. DOI: https://doi.org/10.1029/2019SW002250. eprint: https://agupubs.onlinelibrary.wiley.com/doi/pdf/10.1029/2019SW002250.

Lowder, Chris and Anthony Yeates (Sept. 2017). "Magnetic Flux Rope Identification and Characterization from Observationally Driven Solar Coronal Models". In: *The Astrophysical Journal* 846.2, 106, p. 106. DOI: 10.3847/1538-4357/aa86b1. arXiv: 1708.04522 [astro-ph.SR].

Lumme, E., J. Pomoell, and E. K. J. Kilpua (Dec. 2017). "Optimization of Photospheric Electric Field Estimates for Accurate Retrieval of Total Magnetic Energy Injection". In: *Solar Physics* 292.12, 191, p. 191. DOI: 10.1007/s11207-017-1214-0. arXiv: 1712.05757 [astro-ph.SR].

Luo, W., J. Huang, and J. Yu (Dec. 2007). "Short time fourier analysis based on mathematical morphology". In: 31, pp. 38–41.

Lyot, Bernard (June 1939). "The study of the solar corona and prominences without eclipses (George Darwin Lecture, 1939)". In: *Monthly Notices of the Royal Astronomical Society* 99, p. 580. DOI: 10.1093/mnras/99.8.580.

Ma, Yide, Ro-lan Dai, Li Lian, and Zai-fen Zhang (Jan. 2002). "An Counting and Segmentation method of Blood Cell Image with Logical and morphological Feature of Cell". In: *Chinese Journal of Electronics* 11.

Mackay, Duncan H., L. M. Green, and Aad van Ballegooijen (Feb. 2011). "Modeling the dispersal of an active region: quantifying energy input into the corona". In: *The Astrophysical Journal* 729.2, p. 97. DOI: 10.1088/0004-637X/729/2/97. URL: https://dx.doi.org/10.1088/0004-637X/729/2/97.

Mackenzie Dover, Fionnlagh, Rahul Sharma, and Robertus Erdélyi (May 2021). "Magnetohydrodynamic Simulations of Spicular Jet Propagation Applied to Lower Solar Atmosphere Model". In: *The Astrophysical Journal* 913.1, 19, p. 19. DOI: 10.3847/1538-4357/abefd1.

Maehara, Hiroyuki, Yuta Notsu, Shota Notsu, Kosuke Namekata, Satoshi Honda, Takako T. Ishii, Daisaku Nogami, and Kazunari miyake (Apr. 2017). "Starspot activity and superflares on solar-type stars". In: *Publications of the Astronomical Society of Japan* 69.3. DOI: 10.1093/pasj/psx013. URL: https://doi.org/10.1093%5C%2Fpasj%5C%2Fpsx013.

Maehara, Hiroyuki, Takuya Shibayama, Shota Notsu, Yuta Notsu, Takashi Nagao, Satoshi Kusaba, Satoshi Honda, Daisaku Nogami, and Kazunari Shibata (May 2012). "Superflares on solar-type stars". In: *Nature* 485.7399, pp. 478–481. DOI: 10.1038/nature11063.

Maji, Pradipta, Ankita Mandal, Madhura Ganguly, and Sanjoy Saha (2015). "An automated method for counting and characterizing red blood cells using mathematical morphology". In: *2015 Eighth International Conference on Advances in Pattern Recognition (ICAPR)*, pp. 1–6. DOI: 10.1109/ICAPR.2015.7050674.

Mandal, Sudip, Natalie Krivova, Sami Solanki, Nimesh Sinha, and Dipankar Banerjee (May 2020). "Sunspot area catalog revisited: Daily cross-calibrated areas since 1874". In: *Astronomy & Astrophysics* 640. DOI: 10.1051/0004-6361/202037547.

Maragos, Petros (2009). "Morphological Signal and Image Processing". In: URL: https://api.semanticscholar.org/CorpusID:7037287.

Martínez-Sykora, J., B. De Pontieu, V. H. Hansteen, L. Rouppe van der Voort, M. Carlsson, and T. M. D. Pereira (2017). "On the generation of solar spicules and Alfvénic waves". In: *Science* 356.6344, pp. 1269–1272. DOI: 10.1126/science.aah5412. eprint: https://www.science.org/doi/pdf/10.1126/science.aah5412. URL: https://www.science.org/doi/abs/10.1126/science.aah5412.

Martínez-Sykora, Juan, Bart De Pontieu, Ineke De Moortel, Viggo H. Hansteen, and Mats Carlsson (June 2018). "Impact of Type II Spicules in the Corona: Simulations and Synthetic Observables". In: *The Astrophysical Journal* 860.2, p. 116. DOI: 10.3847/1538-4357/aac2ca. URL: https://dx.doi.org/10.3847/1538-4357/aac2ca.

Matheron, G and Jean Serra (Nov. 2001). "The birth of mathematical morphology". In: *International Symposium on Mathematical Morphology*.

Matheron, Georges (1967). *Eléments pour une théorie des milieux poreux*. Paris: Masson.

Matsumoto, Hitoshi, Masato Ohtani, and Izumi Washitani (2017). "Tree Crown Size Estimated Using Image Processing: A Biodiversity Index for Sloping Subtropical Broad-Leaved Forests". In: *Tropical Conservation Science* 10, p. 1940082917721787. DOI: 10.1177/1940082917721787. eprint: https://doi.org/10.1177/1940082917721787. URL: https://doi.org/10.1177/1940082917721787.

Maunder, E. Walter (June 1904). "Note on the Distribution of Sun-spots in Heliographic Latitude, 1874 to 1902". In: *Monthly Notices of the Royal Astronomical Society* 64.8, pp. 747–761. ISSN: 0035-8711. DOI: 10.1093/mnras/64.8.747. URL: https://doi.org/10.1093/mnras/64.8.747.

Meyer, F. (1979). "Cytologic quantitative et morphologic mathematique". PhD thesis. E .N .S .M .P.

Mira Jr, Joaquim de, Hugo Vieira Neto, Eduardo Neves, and Fábio Schneider (Aug. 2013). "Biometric-oriented Iris Identification Based on Mathematical Morphology". In: *Journal of Signal Processing Systems* 80. DOI: 10.1007/s11265-013-0861-0.

Miri, Mohammad Saleh and Ali Mahloojifar (2011). "Retinal image analysis using curvelet transform and multistructure elements morphology by

reconstruction". In: *IEEE transactions on bio-medical engineering*. DOI: 10.1109/TBME.2010.2097599.

Mishin, E. V., F. A. Marcos, W. J. Burke, D. L. Cooke, C. Roth, and V. P. Petrov (2007). "Prompt thermospheric response to the 6 November 2001 magnetic storm". In: *Journal of Geophysical Research: Space Physics* 112.A5. DOI: https://doi.org/10.1029/2006JA011783. eprint: https://agupubs.onlinelibrary.wiley.com/doi/pdf/10.1029/2006JA011783. URL: https://agupubs.onlinelibrary.wiley.com/doi/abs/10.1029/2006JA011783.

Mondal, Ranjan, Moni Shankar Dey, and Bhabatosh Chanda (2020). "Image Restoration by Learning Morphological Opening-Closing Network". In: *Mathematical Morphology - Theory and Applications* 4.1, pp. 87–107. DOI: doi:10.1515/mathm-2020-0103. URL: https://doi.org/10.1515/mathm-2020-0103.

Moon, Yong-Jae, Jin-Sug Kim, Yeon-Han Kim, and K . -S. Cho (2006). "A Statistical Study of Streamer-Associated Coronal Mass Ejections". In: *Journal of The Korean Astronomical Society*.

Moore, Jason, Kevin Pimbblet, and M. Drinkwater (Dec. 2006). "Mathematical Morphology: Star/Galaxy Differentiation & Galaxy Morphology Classification". In: *PASA* 23. DOI: 10.1071/AS06010.

Mordvinov, A., I.I. Salakhutdinova, L. Plyusnina, Nikolay Makarenko, and L.M. Karimova (Dec. 2002). "The Topology of Background Magnetic Fields and Solar Flare Activity". In: *Solar Physics* 211, pp. 241–253. DOI: 10.1023/A:1022492003881.

Mordvinov, A. V. and L. L. Kitchatinov (Mar. 2004). "Active Longitudes and North–South Asymmetry of the Activity the Sun as Manifestations of Its Relic Magnetic Field". In: *Astronomy Reports* 48.3, pp. 254–260. DOI: 10.1134/1.1687019.

Muslim, M., Dwi Sulistyaningrum, and Budi Setiyono (June 2020). "Detection and counting potholes using morphological method from road video". In: *AIP Conference Proceedings*. Vol. 2242, p. 030011. DOI: 10.1063/5.0008282.

Neugebauer, M., E. J. Smith, A. Ruzmaikin, J. Feynman, and A. H. Vaughan (2000). "The solar magnetic field and the solar wind: Existence of preferred longitudes". In: *Journal of Geophysical Research: Space Physics* 105.A2, pp. 2315–2324. DOI: https://doi.org/10.1029/1999JA000298. eprint:

https://agupubs.onlinelibrary.wiley.com/doi/pdf/10.1029/1999JA000298. URL: https://agupubs.onlinelibrary.wiley.com/doi/abs/10.1029/1999JA000298.

Nikbakhsh, Shabnam, Eija Tanskanen, Maarit Korpi-Lagg, and Thomas Hackman (Aug. 2019). *Differences in the solar cycle variability of simple and complex active regions during 1996-2018*. DOI: 10.48550/arXiv.1908.02226.

Nogueira, Keiller, Jocelyn Chanussot, Mauro Dalla Mura, and Jefersson A. dos Santos (2019). *An Introduction to Deep Morphological Networks*. DOI: 10.48550/ARXIV.1906.01751. URL: https://arxiv.org/abs/1906.01751.

Odenwald, Sten (2007). "Newspaper reporting of space weather: End of a golden age". In: *Space Weather* 5.11. DOI: https://doi.org/10.1029/2007SW000344. eprint: https://agupubs.onlinelibrary.wiley.com/doi/pdf/10.1029/2007SW000344. URL: https://agupubs.onlinelibrary.wiley.com/doi/abs/10.1029/2007SW000344.

Olemskoy, S. V. and L. L. Kitchatinov (Dec. 2009). "Active longitudes of sunspots". In: *Geomagnetism and Aeronomy* 49.7, pp. 866–870. DOI: 10.1134/S001679320907007X.

Al-Omari, M., R. Qahwaji, T. Colak, and S. Ipson (2007). "Morphological-Based Filtering of Noise: Practical Study on Solar Images". In: *IEEE International Conference on Signal Processing and Communication*.

Oxley, William, Joseph Scalisi, Michael S. Ruderman, and Róbert Erdélyi (Dec. 2020). "Formation of Chromospheric Spicules in Magnetic Bright Points: An Analytical Approach Using Cartesian Slab Geometry". In: *The Astrophysical Journal* 905.2, 168, p. 168. DOI: 10.3847/1538-4357/abcafe.

Parenti, Susanna (Dec. 2014). "Solar Prominences: Observations". In: *Living Reviews in Solar Physics* 11.1, 1, p. 1. DOI: 10.12942/lrsp-2014-1.

Parker, E. N. (Nov. 1958). "Dynamics of the Interplanetary Gas and Magnetic Fields." In: *The Astrophysical Journal* 128, p. 664. DOI: 10.1086/146579.

Patty, S.R. and M. J. Hagyard (1986). "Delta-configurations: Flare activity and magnetic-field structure". In: *Solar Physics*. DOI: 10.1007/BF00154862. URL: https://doi.org/10.1007/BF00154862.

Pelt, J., I. Tuominen, and J. Brooke (Jan. 2005). "Century-scale persistence in longitude distribution in the Sun and in silico". In: *Astronomy and Astrophysics* 429, pp. 1093–1096. DOI: 10.1051/0004-6361:20041357. arXiv: astro-ph/0410649 [astro-ph].

Peng, Pingting, Kaifan Ji, and Feng Wang (Nov. 2013). "A Survey of Solar Filament Detection Methods". In: pp. 320–323. ISBN: 978-1-4799-2809-5. DOI: 10.1109/ICINIS.2013.89.

Pesnell, W. Dean, B. J. Thompson, and P. C. Chamberlin (Jan. 2012). "The Solar Dynamics Observatory (SDO)". In: *Solar Physics* 275.1-2, pp. 3–15. DOI: 10.1007/s11207-011-9841-3.

Pevtsov, Alexei a and Richard C Canfield (1999). "Helicity of the Photospheric Magnetic Field". In: *Magnetic Helicity in Space and Laboratory Plasmas*. American Geophysical Union (AGU), pp. 103–110. ISBN: 9781118664476. DOI: https://doi.org/10.1029/GM111p0103. eprint: https://agupubs.onlinelibrary.wiley.com/doi/pdf/10.1029/GM111p0103. URL: https://agupubs.onlinelibrary.wiley.com/doi/abs/10.1029/GM111p0103.

Pevtsov, Alexei A., K. S. Balasubramaniam, and Joey W. Rogers (Sept. 2003). "Chirality of Chromospheric Filaments". In: *The Astrophysical Journal* 595.1, pp. 500–505. DOI: 10.1086/377339.

Pina, Pedro, Teresa Barata, and Lourenco Bandeira (2006). "Morphological recognition of the spatial patterns of olive trees". In: *Proceedings of the 18th International Conference on Pattern Recognition - Volume 04*. ICPR '06. USA: IEEE Computer Society, pp. 845–848. ISBN: 0769525210. DOI: 10.1109/ICPR.2006.811. URL: https://doi.org/10.1109/ICPR.2006.811.

Pina, Pedro, Luís Ribeiro, and Fernando Muge (2001). "A mathematical morphology contribution to study some aspects of hydrogeological systems". In: *Computers & Geosciences* 27.9. Geological Applications of Digital Imaging, pp. 1061–1069. ISSN: 0098-3004. DOI: https://doi.org/10.1016/S0098-3004(00)00155-2. URL: https://www.sciencedirect.com/science/article/pii/S0098300400001552.

Plyusnina, L. A. (Feb. 2010). "Determination of the Rotation Periods of Solar Active Longitudes". In: *Solar Physics* 261.2, pp. 223–232. DOI: 10.1007/s11207-009-9501-z.

Pomoell, Jens, Erkka Lumme, and Emilia Kilpua (Apr. 2019). "Time-dependent Data-driven Modeling of Active Region Evolution Using Energy-optimized Photospheric Electric Fields". In: *Solar Physics* 294.4, 41, p. 41. DOI: 10.1007/s11207-019-1430-x.

Prêteux, F. (1992). "Mathematical Morphology and Medical Imaging". In: *Medical Images: Formation, Handling and Evaluation*. Ed. by Andrew E.

Todd-Pokropek and Max A. Viergever. Berlin, Heidelberg: Springer Berlin Heidelberg, pp. 87–117. ISBN: 978-3-642-77888-9.

Price, D. J., J. Pomoell, E. Lumme, and E. K. J. Kilpua (Aug. 2019). "Time-dependent data-driven coronal simulations of AR 12673 from emergence to eruption". In: *Astronomy and Astrophysics* 628, A114, A114. DOI: 10.1051/0004-6361/201935535.

Priest, Eric and Terry Forbes (2000). *Magnetic Reconnection: MHD Theory and Applications*. DOI: 10.1017/CBO9780511525087.

Puissant, Anne, Sébastien Lefèvre, and Jonathan Weber (July 2008). "Coastline extraction in VHR imagery using mathematical morphology with spatial and spectral knowledge". In: *International Society for Photogrammetry and Remote Sensing Congress (ISPRS)*.

Qahwaji, Rami and T Colak (Jan. 2005). "Automatic detection and verification of solar features". In: *International Journal of Imaging Systems and Technology* 15. DOI: 10.1002/ima.20053.

Yu-Qian, Zhao, Gui Wei-Hua, Chen Zhen-Cheng, Tang Jing-Tian, and Li Ling-Yun (2005). "Medical images edge detection based on mathematical morphology". In: *Annual International Conference of the IEEE Engineering in Medicine and Biology Society*. DOI: 10.1109/IEMBS.2005.1615986.

Qu, Ming, Frank Shih, Ju Jing, and Haimin Wang (May 2005). "Automatic Solar Filament Detection Using Image Processing Techniques". In: *Solar Physics* 228, pp. 119–135. DOI: 10.1007/s11207-005-5780-1.

Quan, Lin, Long Xu, Ling Li, Huaning Wang, and Xin Huang (2021). "Solar Active Region Detection Using Deep Learning". In: *Electronics* 10.18. ISSN: 2079-9292. DOI: 10.3390/electronics10182284. URL: https://www.mdpi.com/2079-9292/10/18/2284.

Raouafi, N. E., S. Patsourakos, E. Pariat, P. R. Young, A. C. Sterling, A. Savcheva, M. Shimojo, F. Moreno-Insertis, C. R. DeVore, V. Archontis, T. Török, H. Mason, W. Curdt, K. Meyer, K. Dalmasse, and Y. Matsui (Nov. 2016). "Solar Coronal Jets: Observations, Theory, and Modeling". In: *Space Science Reviews* 201.1-4, pp. 1–53. DOI: 10.1007/s11214-016-0260-5. arXiv: 1607.02108 [astro-ph.SR].

Raphaldini, Breno, Mausumi Dikpati, and Scott W. McIntosh (Aug. 2023). "Information-theoretic Analysis of Longitude Distribution of Photospheric Magnetic Fields from MDI/HMI Synoptic Maps: Evidence for Rossby

Waves". In: *The Astrophysical Journal* 953.2, p. 156. DOI: 10.3847/1538-4357/ace320. URL: https://dx.doi.org/10.3847/1538-4357/ace320.

Reale, Fabio (Dec. 2010). "Coronal Loops: Observations and Modeling of Confined Plasma". In: *Living Reviews in Solar Physics* 7.1, 5, p. 5. DOI: 10.12942/lrsp-2010-5. arXiv: 1010.5927 [astro-ph.SR].

Reames, D.V (2004). "Solar energetic particle variations". In: *Advances in Space Research* 34.2. Solar Variability and Climate Change, pp. 381–390. ISSN: 0273-1177. DOI: https://doi.org/10.1016/j.asr.2003.02.046. URL: https://www.sciencedirect.com/science/article/pii/S0273117704002406.

Reames, Donald V. (Jan. 2013). "The Two Sources of Solar Energetic Particles". In: *Space Science Reviews* 175.1–4, pp. 53–92. ISSN: 1572-9672. DOI: 10.1007/s11214-013-9958-9. URL: http://dx.doi.org/10.1007/s11214-013-9958-9.

— (2021). "Gradual SEP Events". In: *Solar Energetic Particles: A Modern Primer on Understanding Sources, Acceleration and Propagation*. Cham: Springer International Publishing, pp. 97–133. ISBN: 978-3-030-66402-2. DOI: 10.1007/978-3-030-66402-2_5. URL: https://doi.org/10.1007/978-3-030-66402-2_5.

Redmon, R. J., D. B. Seaton, R. Steenburgh, J. He, and J. V. Rodriguez (2018). "September 2017's Geoeffective Space Weather and Impacts to Caribbean Radio Communications During Hurricane Response". In: *Space Weather* 16.9, pp. 1190–1201. DOI: https://doi.org/10.1029/2018SW001897. eprint: https://agupubs.onlinelibrary.wiley.com/doi/pdf/10.1029/2018SW001897. URL: https://agupubs.onlinelibrary.wiley.com/doi/abs/10.1029/2018SW001897.

Rempel, M., M. Schüssler, R. H. Cameron, and M. Knölker (2009). "Penumbral Structure and Outflows in Simulated Sunspots". In: *Science* 325.5937, pp. 171–174. DOI: 10.1126/science.1173798. eprint: https://www.science.org/doi/pdf/10.1126/science.1173798. URL: https://www.science.org/doi/abs/10.1126/science.1173798.

Rieger, E., G. H. Share, D. J. Forrest, G. Kanbach, C. Reppin, and E. L. Chupp (Dec. 1984). "A 154-day periodicity in the occurrence of hard solar flares?" In: *Nature* 312.5995, pp. 623–625. DOI: 10.1038/312623a0.

Riley, Pete, Roberto Lionello, Zoran Mikić, and Jon Linker (Jan. 2008). "Using Global Simulations to Relate the Three-Part Structure of Coronal Mass

Ejections to In Situ Signatures". In: *The Astrophysical Journal* 672.2, pp. 1221–1227. DOI: 10.1086/523893.

Rishikeshan, C A and Ramesh Gowda (Nov. 2017). "A novel mathematical morphology based algorithm for shoreline extraction from satellite images". In: *Geo-spatial Information Science* 20, pp. 1–8. DOI: 10.1080/10095020.2017.1403089.

Ritter, G.X. and Peter Sussner (Sept. 1996). "An introduction to morphological neural networks". In: vol. 4, 709–717 vol.4. ISBN: 0-8186-7282-X. DOI: 10.1109/ICPR.1996.547657.

Rivest, J.F. (Sept. 2011). *Mathematical morphology and short-term Fourier transforms*. Tech. rep.

Roberts, B. (Feb. 1979). "Spicules: The resonant response to granular buffeting?" In: *Solar Physics* 61.1, pp. 23–34. DOI: 10.1007/BF00155443.

Roberts, Walter Orr (Mar. 1945). "A Preliminary Report on Chromospheric Spicules of Extremely Short Lifetime." In: *The Astrophysical Journal* 101, p. 136. DOI: 10.1086/144699.

Roerdink, J.B.T.M. (1996). "Computer Vision and Mathematical Morphology". English. In: *Theoretical foundations of computer vision*. Ed. by W. Kropratsch, R. Klette, and R. Albrecht. Computing. Supplementum. Relation: http://www.rug.nl/informatica/organisatie/overorganisatie/iwi Rights: University of Groningen. Research Institute for Mathematics and Computing Science (IWI). Springer. ISBN: 3211827307.

Romero-García, Gonzalo (Nov. 2023). "Mathematical Morphology for the Analysis and Generation of Time-Frequency Representations of Music". Theses. Sorbonne Université. URL: https://theses.hal.science/tel-04470770.

Roy, Swalpa, Ranjan Mondal, Mercedes Paoletti, Juan Haut, and Antonio Plaza (June 2021). "Morphological Convolutional Neural Networks for Hyperspectral Image Classification". In: *IEEE Journal of Selected Topics in Applied Earth Observations and Remote Sensing* PP, pp. 8689–8702. DOI: 10.1109/JSTARS.2021.3088228.

Samir, L'Haddad, Akila Kemmouche, and A. Nuscia TAÏBI (Mar. 2024). "Computing Multivalued Mathematical Morphology on Multiband Images Using Algorithms for Multicriteria Analysis". In: *Image Analysis and Stereology* 43, pp. 23–40. DOI: 10.5566/ias.3042.

Santos, José, Nuno Peixinho, Teresa Barata, Carlos Pereira, A. Paulo Coimbra, Manuel M. Crisóstomo, and Mateus Mendes (2023). "Sunspot Detection Using YOLOv5 in Spectroheliograph H-Alpha Images". In: *Applied Sciences* 13.10. ISSN: 2076-3417. DOI: 10.3390/app13105833. URL: https://www.mdpi.com/2076-3417/13/10/5833.

Satya Narayanan, A. and K. Somasundaram (Feb. 1985). "Alfvén Surface Waves along coronal streamers". In: *Astrophysics and Space Science* 109.2, pp. 357–364. DOI: 10.1007/BF00651281.

Scalisi, Joseph, William Oxley, Michael S. Ruderman, and Robertus Erdélyi (Apr. 2021). "Propagation of Torsional Alfvén Pulses in Zero-beta Flux Tubes". In: *The Astrophysical Journal* 911.1, 39, p. 39. DOI: 10.3847/1538-4357/abe8db.

Schaefer, Bradley E. (May 2012). "Astrophysics: Startling superflares". In: *Nature* 485.7399, pp. 456–457. DOI: 10.1038/nature11194.

Scherrer, P. H., R. S. Bogart, R. I. Bush, J. T. Hoeksema, A. G. Kosovichev, J. Schou, W. Rosenberg, L. Springer, T. D. Tarbell, A. Title, C. J. Wolfson, I. Zayer, and MDI Engineering Team (Dec. 1995). "The Solar Oscillations Investigation - Michelson Doppler Imager". In: *Solar Physics* 162.1-2, pp. 129–188. DOI: 10.1007/BF00733429.

Scholl, Isabelle F. and Shadia Rifai Habbal (Apr. 2008). "Automatic Detection and Classification of Coronal Holes and Filaments Based on EUV and Magnetogram Observations of the Solar Disk". In: *Solar Physics* 248.2, pp. 425–439. DOI: 10.1007/s11207-007-9075-6.

Schou, J., P. H. Scherrer, R. I. Bush, R. Wachter, S. Couvidat, M. C. Rabello-Soares, R. S. Bogart, J. T. Hoeksema, Y. Liu, T. L. Duvall, D. J. Akin, B. A. Allard, J. W. Miles, R. Rairden, R. A. Shine, T. D. Tarbell, A. M. Title, C. J. Wolfson, D. F. Elmore, A. A. Norton, and S. Tomczyk (Jan. 2012). "Design and ground calibration of the Helioseismic and Magnetic Imager (HMI) instrument on the Solar Dynamics Observatory (SDO)". In: *Solar Physics* 275.1-2, pp. 229–259. DOI: 10.1007/s11207-011-9842-2.

Schwabe, Heinrich and Hofrath Schwabe Herrn (1844). "Sonnen — Beobachtungen im Jahre 1843". In: *Astronomische Nachrichten* 21.15, pp. 234–235. DOI: https://doi.org/10.1002/asna.18440211505. eprint: https://onlinelibrary.wiley.com/doi/pdf/10.1002/asna.18440211505. URL: https://onlinelibrary.wiley.com/doi/abs/10.1002/asna.18440211505.

Secchi, A. (1878). *Die Sterne: Grundzüge der Astronomie der Fixsterne*. Internationale wissenschaftliche Bibliothek. Brockhaus. URL: https://books.google.pt/books?id=yLSBiVUZwKwC.

Serra, J. and École nationale supérieure des mines de Paris (1969). *Introduction à la morphologie mathématique*. Cahiers du Centre de morphologie mathématique de Fontainebleau. Fontainebleau: Centre de morphologie mathématique de Fontainebleau. URL: https://books.google.fr/books?id=5dNcPgAACAAJ.

Serra, Jean (1982). *Image analysis and mathematical morphology*. Vol. 1. London: Academic Press.

— (2020). "Mathematical morphology". In: *Encyclopedia of Mathematical Geosciences*. Ed. by B. S. Daya Sagar, Qiuming Cheng, Jennifer McKinley, and Frits Agterberg. Cham: Springer International Publishing, pp. 1–16. ISBN: 978-3-030-26050-7. DOI: 10.1007/978-3-030-26050-7_22-2.

Shea, M. A. and D. F. Smart (June 1990). "A Summary of Major Solar Proton Events". In: *Solar Physics* 127.2, pp. 297–320. DOI: 10.1007/BF00152170.

Shen, Yucong, Xin Zhong, and Frank Y. Shih (2019). *Deep Morphological Neural Networks*. DOI: 10.48550/ARXIV.1909.01532. URL: https://arxiv.org/abs/1909.01532.

Shi, Zhongxian and Jingxiu Wang (1993). "Delta-Sunspots and X-Class Flares in Solar Cycle 22". In: *International Astronomical Union Colloquium* 141, pp. 71–74. DOI: 10.1017/S0252921100028815.

— (July 1994). "Delta-sunspots and X-class flares". In: *Solar Physics* 149, pp. 105–118. DOI: 10.1007/BF00645181.

Shibata, Kazunari, Yoshinori Ishido, Loren W. Acton, Keith T. Strong, Tadashi Hirayama, Yutaka Uchida, Alan H. McAllister, Ryoji Matsumoto, Saku Tsuneta, Toshifumi Shimizu, Hirohisa Hara, Takashi Sakurai, Kiyoshi Ichimoto, Yohei Nishino, and Yoshiaki Ogawara (Oct. 1992). "Observations of X-Ray Jets with the YOHKOH Soft X-Ray Telescope". In: *Publications of the Astronomical Society of Japan* 44, pp. L173–L179.

Shibata, Kazunari, Hiroaki Isobe, Andrew Hillier, Arnab Rai Choudhuri, Hiroyuki Maehara, Takako T. Ishii, Takuya Shibayama, Shota Notsu, Yuta Notsu, Takashi Nagao, Satoshi Honda, and Daisaku Nogami (June 2013). "Can Superflares Occur on Our Sun?" In: *Publications of the Astronomical Society of Japan* 65.3, p. 49. ISSN: 0004-6264. DOI: 10.1093/pasj/65.3.49.

eprint: https://academic.oup.com/pasj/article-pdf/65/3/49/60460001/pasj_65_3_49.pdf.

Shih, Frank Y. and Artur J. Kowalski (Dec. 2003). "Automatic Extraction of Filaments in Hα Solar Images". In: *Solar Physics* 218.1, pp. 99–122. DOI: 10.1023/B:SOLA.0000013052.34180.58.

Shrivastav, Arpit Kumar, Vaibhav Pant, David Berghmans, Andrei N. Zhukov, Tom Van Doorsselaere, Elena Petrova, Dipankar Banerjee, Daye Lim, and Cis Verbeeck (2024). "Statistical investigation of decayless oscillations in small-scale coronal loops observed by Solar Orbiter/EUI". In: *Astronomy & Astrophysics* 685, A36. DOI: 10.1051/0004-6361/202346670. URL: https://doi.org/10.1051/0004-6361/202346670.

Skirgiello, M. (2005). "The east-west asymmetry in Coronal Mass Ejections: evidence for active longitudes". In: *Annales Geophysicae* 23.9, pp. 3139–3147. DOI: 10.5194/angeo-23-3139-2005. URL: https://angeo.copernicus.org/articles/23/3139/2005/.

Skirvin, Samuel, Gary Verth, José Juan González-Avilés, Sergiy Shelyag, Rahul Sharma, Francisco S. Guzmán, Istvan Ballai, Eamon Scullion, Suzana S.A. Silva, and Viktor Fedun (2023). "Small-scale solar jet formation and their associated waves and instabilities". In: *Advances in Space Research* 71.4. Recent progress in the physics of the Sun and heliosphere, pp. 1866–1892. ISSN: 0273-1177. DOI: https://doi.org/10.1016/j.asr.2022.05.033. URL: https://www.sciencedirect.com/science/article/pii/S0273117722004124.

Sohini, Roychowdhury, Koozekanani Dara D., and Parhi Keshab K. (2015). "Blood Vessel Segmentation of Fundus Images by Major Vessel Extraction and Subimage Classification". In: *IEEE Journal of Biomedical and Health Informatics* 19.3, pp. 1118–1128. DOI: 10.1109/JBHI.2014.2335617.

Soille, Pierre (1999). *Morphological Image Analysis*. Springer Berlin, Heidelberg. DOI: https://doi.org/10.1007/978-3-662-03939.

Soler, R., J. Terradas, R. Oliver, and J.L. Ballester (2016). "The role of Alfvén wave heating in solar prominences". In: *A&A* 592, A28. DOI: 10.1051/0004-6361/201628722. URL: https://doi.org/10.1051/0004-6361/201628722.

Solov'ev, A A and E A Kirichek (Nov. 2018). "Structure of solar faculae". In: *Monthly Notices of the Royal Astronomical Society* 482.4, pp. 5290–5301.

ISSN: 0035-8711. DOI: 10.1093/mnras/sty3050. eprint: https://academic.oup.com/mnras/article-pdf/482/4/5290/26899007/sty3050.pdf.

Soós, Sz., J. Liu, M. B. Korsós, and R. Erdélyi (Apr. 2024). "Evolution of Coronal Jets during Solar Cycle 24". In: *The Astrophysical Journal* 965.1, p. 43. DOI: 10.3847/1538-4357/ad29f8. URL: https://dx.doi.org/10.3847/1538-4357/ad29f8.

Srivastava, A. K., S. K. Mishra, P. Jelínek, Tanmoy Samanta, Hui Tian, Vaibhav Pant, P. Kayshap, Dipankar Banerjee, J. G. Doyle, and B. N. Dwivedi (Dec. 2019). "On the Observations of Rapid Forced Reconnection in the Solar Corona". In: *The Astrophysical Journal* 887.2, p. 137. DOI: 10.3847/1538-4357/ab4a0c. URL: https://dx.doi.org/10.3847/1538-4357/ab4a0c.

Stangalini, Marco, Robertus Erdélyi, Callum Boocock, David Tsiklauri, Christopher J. Nelson, Dario Del Moro, Francesco Berrilli, and Marianna B. Korsós (Jan. 2021). "Torsional oscillations within a magnetic pore in the solar photosphere". In: *Nature Astronomy* 5, pp. 691–696. DOI: 10.1038/s41550-021-01354-8.

Stenning, David, Vanshita Kashyap, Thomas Lee, David Dyk, C. Young, David Stenning, Vinay Kashyap, Thomas Lee, David van Dyk, and C Young (Jan. 2013). "Morphological Image Analysis and Its Application to Sunspot Classification". In: 209. DOI: 10.1007/978-1-4614-3520-4-31.

Subramanian, Prasad and K. P. Dere (Nov. 2001). "Source Regions of Coronal Mass Ejections". In: *The Astrophysical Journal* 561.1, p. 372. DOI: 10.1086/323213. URL: https://dx.doi.org/10.1086/323213.

Sun, W., M. Dryer, C. D. Fry, C. S. Deehr, Z. Smith, S. -I. Akasofu, M. D. Kartalev, and K. G. Grigorov (July 2002). "Real-time forecasting of ICME shock arrivals at L1 during the "April FoolÂ's Day" epoch: 28 March Â 21 April 2001". In: *Annales Geophysicae* 20.7, pp. 937–945. DOI: 10.5194/angeo-20-937-2002.

Svalgaard, Leif and Yohsuke Kamide (Jan. 2013). "Asymmetric Solar Polar Field Reversals". In: *The Astrophysical Journal* 763.1, 23, p. 23. DOI: 10.1088/0004-637X/763/1/23. arXiv: 1207.2077 [astro-ph.SR].

Talib, Mohammad and Tiroyamodimo Mmapadi Mogotlhwane (Dec. 2011). "Global Failure of ICT due to Solar Storm: A Worst Case Scenario Ahead". In: *Procedia Environmental Sciences* 8, pp. 371–374. DOI: 10.1016/j.proenv.2011.10.058.

Titov, Vyacheslav S., Gunnar Hornig, and Pascal Démoulin (Aug. 2002). "Theory of magnetic connectivity in the solar corona". In: *Journal of Geophysical Research (Space Physics)* 107.A8, 1164, p. 1164. DOI: 10.1029/2001JA000278.

Toma, Giuliana de, Oran R. White, and Karen L. Harvey (Feb. 2000). "A Picture of Solar Minimum and the Onset of Solar Cycle 23. I. Global Magnetic Field Evolution". In: *The Astrophysical Journal* 529.2, p. 1101. DOI: 10.1086/308299. URL: https://dx.doi.org/10.1086/308299.

Uberoi, Chanchal (2011). "Geomagnetic Storms Over India: A Close Look at Historic Space Weather at Mumbai". In: *Space Weather* 9.8. DOI: https://doi.org/10.1029/2011SW000686. eprint: https://agupubs.onlinelibrary.wiley.com/doi/pdf/10.1029/2011SW000686. URL: https://agupubs.onlinelibrary.wiley.com/doi/abs/10.1029/2011SW000686.

Upraity, Harendra and K V Arya (2014). "Efficient face recognition using morphological operations". In: *2014 9th International Conference on Industrial and Information Systems (ICIIS)*, pp. 1–6. DOI: 10.1109/ICIINFS.2014.7036567.

Usmanov, A.V., B.P. Besser, J.M. Fritzer, and M.L. Goldstein (2000). "Simulation of a coronal streamer: Alfvén wave acceleration". In: *Advances in Space Research* 25.9. Coronal Structure and Dynamics Near Solar Activity Minimum, pp. 1897–1900. ISSN: 0273-1177. DOI: https://doi.org/10.1016/S0273-1177(99)00613-4. URL: https://www.sciencedirect.com/science/article/pii/S0273117799006134.

Usoskin, I.G., S.V. Berdyugina, D. Moss, and D.D. Sokoloff (2007). "Long-term persistence of solar active longitudes and its implications for the solar dynamo theory". In: *Advances in Space Research* 40.7, pp. 951–958. ISSN: 0273-1177. DOI: https://doi.org/10.1016/j.asr.2006.12.050. URL: https://www.sciencedirect.com/science/article/pii/S0273117707007223.

Üstüner, Mustafa, Fusun Balik Sanli, and Saygin Abdikan (July 2019). "FOREST TYPE CLASSIFICATION USING MORPHOLOGICAL OPERATORS AND FOREST PA METHOD". In.

Vaisberg, O. L. and G. N. Zastenker (Nov. 1976). "Solar Wind and Magnetosheath Observations at Earth During August 1972". In: *Space Science Reviews* 19.4-5, pp. 687–702. DOI: 10.1007/BF00210646.

Van Doorsselaere, Tom, Abhishek K. Srivastava, Patrick Antolin, Norbert Magyar, Soheil Vasheghani Farahani, Hui Tian, Dmitrii Kolotkov, Leon Ofman, Mingzhe Guo, Iñigo Arregui, Ineke De Moortel, and David Pascoe (Dec. 2020). "Coronal Heating by MHD Waves". In: *Space Science Reviews* 216.8. ISSN: 1572-9672. DOI: 10.1007/s11214-020-00770-y. URL: http://dx.doi.org/10.1007/s11214-020-00770-y.

Vernova, E. S., K. Mursula, M. I. Tyasto, and D. G. Baranov (Jan. 2004). "Longitudinal asymmetry in sunspot activity during the ascending and descending phase of the solar cycle". In: *Multi-Wavelength Investigations of Solar Activity*. Ed. by Alexander V. Stepanov, Elena E. Benevolenskaya, and Alexander G. Kosovichev. Vol. 223. IAU Symposium, pp. 155–156. DOI: 10.1017/S1743921304005514.

Vourlidas, A., B. J. Lynch, R. A. Howard, and Y. Li (May 2013). "How Many CMEs Have Flux Ropes? Deciphering the Signatures of Shocks, Flux Ropes, and Prominences in Coronagraph Observations of CMEs". In: *Solar Physics* 284.1, pp. 179–201. DOI: 10.1007/s11207-012-0084-8. arXiv: 1207.1599 [astro-ph.SR].

Wagner, A., E. K. J. Kilpua, R. Sarkar, D. J. Price, A. Kumari, F. Daei, J. Pomoell, and S. Poedts (Sept. 2023a). "The automatic identification and tracking of coronal flux ropes: I. Footpoints and fluxes". In: *Astronomy & Astrophysics* 677, A81. ISSN: 1432-0746. DOI: 10.1051/0004-6361/202346260. URL: http://dx.doi.org/10.1051/0004-6361/202346260.

Wagner, A., D. J. Price, S. Bourgeois, F. Daei, J. Pomoell, S. Poedts, A. Kumari, T. Barata, R. Erdélyi, and E. K. J. Kilpua (Dec. 2024a). "The effect of data-driving and relaxation models on magnetic flux rope evolution and stability". In: *Astronomy and Astrophysics* 692, A74, A74. DOI: 10.1051/0004-6361/202450577. arXiv: 2410.18672 [astro-ph.SR].

Wagner, Andreas, Slava Bourgeois, Emilia K. J. Kilpua, Ranadeep Sarkar, Daniel J. Price, Anshu Kumari, Jens Pomoell, Stefaan Poedts, Teresa Barata, Robertus Erdélyi, Orlando Oliveira, and Ricardo Gafeira (2023b). *The Automatic Identification and Tracking of Coronal Flux Ropes – Part II: New Mathematical Morphology-based Flux Rope Extraction Method and Deflection Analysis*. arXiv: 2312.00673 [astro-ph.SR].

Wagner, Andreas, Daniel J. Price, Slava Bourgeois, Jens Pomoell, Stefaan Poedts, and Emilia K. J. Kilpua (2024b). "Solar magnetic flux rope identification with GUITAR: GUI for Tracking and Analysing flux Ropes".

In: *Frontiers in Astronomy and Space Sciences* 11. ISSN: 2296-987X. DOI: 10.3389/fspas.2024.1383072. URL: https://www.frontiersin.org/articles/10.3389/fspas.2024.1383072.

Wang, G., Y. Wang, H. Li, X. Chen, H. Lu, Y. Ma, C. Peng, Y. Wang, and L. Tang (2014). "Morphological background detection and illumination normalization of text image with poor lighting". In: *PLoS One*. DOI: 10.1371/journal.pone.0110991.

Webb, David F. and Timothy A. Howard (June 2012). "Coronal Mass Ejections: Observations". In: *Living Reviews in Solar Physics* 9.1, 3, p. 3. DOI: 10.12942/lrsp-2012-3.

Wedemeyer-Böhm, Sven, Eamon Scullion, Oskar Steiner, Luc Rouppe van der Voort, Jaime de La Cruz Rodriguez, Viktor Fedun, and Robert Erdélyi (June 2012). "Magnetic tornadoes as energy channels into the solar corona". In: *Nature* 486.7404, pp. 505–508. DOI: 10.1038/nature11202.

Wenqi, Zhang, Bai Wanmin, Yu Jun, and Gao Shouyi (2018). "The New Method of Sea-sky Line Detection Based on Mathematical Morphology". In: *International Journal of Advanced Network, Monitoring and Controls* 3.3, pp. 85–92. DOI: doi:10.21307/ijanmc-2019-010. URL: https://doi.org/10.21307/ijanmc-2019-010.

Whitman, Kathryn, Ricky Egeland, Ian G. Richardson, Clayton Allison, Philip Quinn, Janet Barzilla, Irina Kitiashvili, Viacheslav Sadykov, Hazel M. Bain, Mark Dierckxsens, M. Leila Mays, Tilaye Tadesse, Kerry T. Lee, Edward Semones, Janet G. Luhmann, Marlon Núñez, Stephen M. White, Stephen W. Kahler, Alan G. Ling, Don F. Smart, Margaret A. Shea, Valeriy Tenishev, Soukaina F. Boubrahimi, Berkay Aydin, Petrus Martens, Rafal Angryk, Michael S. Marsh, Silvia Dalla, Norma Crosby, Nathan A. Schwadron, Kamen Kozarev, Matthew Gorby, Matthew A. Young, Monica Laurenza, Edward W. Cliver, Tommaso Alberti, Mirko Stumpo, Simone Benella, Athanasios Papaioannou, Anastasios Anastasiadis, Ingmar Sandberg, Manolis K. Georgoulis, Anli Ji, Dustin Kempton, Chetraj Pandey, Gang Li, Junxiang Hu, Gary P. Zank, Eleni Lavasa, Giorgos Giannopoulos, David Falconer, Yash Kadadi, Ian Fernandes, Maher A. Dayeh, Andrés Muñoz-Jaramillo, Subhamoy Chatterjee, Kimberly D. Moreland, Igor V. Sokolov, Ilia I. Roussev, Aleksandre Taktakishvili, Frederic Effenberger, Tamas Gombosi, Zhenguang Huang, Lulu Zhao, Nicolas Wijsen, Angels Aran, Stefaan Poedts, Athanasios Kouloumvakos, Miikka Paassilta, Rami

Vainio, Anatoly Belov, Eugenia A. Eroshenko, Maria A. Abunina, Artem A. Abunin, Christopher C. Balch, Olga Malandraki, Michalis Karavolos, Bernd Heber, Johannes Labrenz, Patrick Kühl, Alexander G. Kosovichev, Vincent Oria, Gelu M. Nita, Egor Illarionov, Patrick M. O'Keefe, Yucheng Jiang, Sheldon H. Fereira, Aatiya Ali, Evangelos Paouris, Sigiava Aminalragia-Giamini, Piers Jiggens, Meng Jin, Christina O. Lee, Erika Palmerio, Alessandro Bruno, Spiridon Kasapis, Xiantong Wang, Yang Chen, Blai Sanahuja, David Lario, Carla Jacobs, Du Toit Strauss, Ruhann Steyn, Jabus van den Berg, Bill Swalwell, Charlotte Waterfall, Mohamed Nedal, Rositsa Miteva, Momchil Dechev, Pietro Zucca, Alec Engell, Brianna Maze, Harold Farmer, Thuha Kerber, Ben Barnett, Jeremy Loomis, Nathan Grey, Barbara J. Thompson, Jon A. Linker, Ronald M. Caplan, Cooper Downs, Tibor Török, Roberto Lionello, Viacheslav Titov, Ming Zhang, and Pouya Hosseinzadeh (2023). "Review of Solar Energetic Particle Prediction Models". In: *Advances in Space Research* 72.12. COSPAR Space Weather Roadmap 2022-2024: Scientific Research and Applications, pp. 5161–5242. ISSN: 0273-1177. DOI: https://doi.org/10.1016/j.asr.2022.08.006. URL: https://www.sciencedirect.com/science/article/pii/S0273117722007244.

Willis, D. M., F. R. Stephenson, and J. R. Singh (Dec. 1996). "Auroral Observations on AD 1770 September 16: the Earliest Known Conjugate Sightings". In: *Quarterly Journal of the Royal Astronomical Society* 37, p. 733.

Wu, Chin-Chun, Kan Liou, Ronald P. Lepping, Lynn Hutting, Simon Plunkett, Russ A. Howard, and Dennis Socker (Dec. 2016). "The first super geomagnetic storm of solar cycle 24: "The St. Patrick's day event (17 March 2015)"". In: *Earth, Planets and Space* 68.1, 151, p. 151. DOI: 10.1186/s40623-016-0525-y.

Wu, D. J. and C. Fang (Oct. 2003). "Coronal Plume Heating and Kinetic Dissipation of Kinetic Alfvén Waves". In: *The Astrophysical Journal* 596.1, p. 656. DOI: 10.1086/377599. URL: https://dx.doi.org/10.1086/377599.

Xu, Hongyun, Xiaoli Xu, and Yunbo Zuo (2019). "Applying morphology to improve Canny operator's image segmentation method". In: *The Journal of Engineering* 2019.23, pp. 8816–8819. DOI: https://doi.org/10.1049/joe.2018.9113. eprint: https://ietresearch.onlinelibrary.wiley.com/doi/pdf/10.1049/joe.2018.9113. URL: https://ietresearch.onlinelibrary.wiley.com/doi/abs/10.1049/joe.2018.9113.

Yan-mei, CUI, LIU Si-qing, and SHI Li-qin (2021). "Automatic Recognition of Solar Active Regions Based on Real-time SDO/HMI Full-disk Magnetograms". In: *Chinese Astronomy and Astrophysics* 45.4, pp. 458–469. ISSN: 0275-1062. DOI: https://doi.org/10.1016/j.chinastron.2021.11.002. URL: https://www.sciencedirect.com/science/article/pii/S0275106221000898.

Yang, W. H., P. A. Sturrock, and S. K. Antiochos (Oct. 1986). "Force-free Magnetic Fields: The Magneto-frictional Method". In: *The Astrophysical Journal* 309, p. 383. DOI: 10.1086/164610.

Yang, Yunfei, Hongjuan Yang, Xianyong Bai, Huituan Zhou, Song Feng, and Bo Liang (Sept. 2018). "Automatic Detection of Sunspots on Full-disk Solar Images Using the Simulated Annealing Genetic Method". In: *Publications of the Astronomical Society of the Pacific* 130.992, p. 104503. DOI: 10.1088/1538-3873/aadbfa. URL: https://dx.doi.org/10.1088/1538-3873/aadbfa.

Yeates, A. R. (Apr. 2013). "Coronal Magnetic Field Evolution from 1996 to 2012: Continuous Non-potential Simulations". In: *Solar Physics* 289.2, pp. 631–648. ISSN: 1573-093X. DOI: 10.1007/s11207-013-0301-0. URL: http://dx.doi.org/10.1007/s11207-013-0301-0.

Youssef, M. (2012). "On the relation between the CMEs and the solar flares". In: *NRIAG Journal of Astronomy and Geophysics* 1.2, pp. 172–178. ISSN: 2090-9977. DOI: https://doi.org/10.1016/j.nrjag.2012.12.014. URL: https://www.sciencedirect.com/science/article/pii/S2090997712000235.

Zana, Frederic and Jean-Claude Klein (July 2001). "Segmentation of vessel-like patterns using mathematical morphology and curvature evaluation". In: *Image Processing, IEEE Transactions on* 10, pp. 1010–1019. DOI: 10.1109/83.931095.

Zhang, L., K. Mursula, I. Usoskin, and H. Wang (Feb. 2011). "Global analysis of active longitudes of solar X-ray flares". English (US). In: *Journal of Atmospheric and Solar-Terrestrial Physics* 73.2-3. Funding Information: The research leading to these results has received funding from the European Commission's Seventh Framework Programme (FP7/2007-2013) under the Grant agreement no. 218816 (SOTERIA Project, http://www.soteria-space.eu). We also acknowledge the financial support by the Academy of Finland to the HISSI research project no. 128189. This work is jointly

supported by the National Basic Research Program of China (Program 973) through Grant 2006CB806307, the National Natural Science Foundation of China (NSFC) through Grants 10673017, 10733020, 10803011 and 40890161, and Projects KJCX2-YW-T04 and KGCX3-SYW-403C10 of the Chinese Academy of Sciences (CAS)., pp. 258–263. ISSN: 1364-6826. DOI: 10.1016/j.jastp.2009.12.003.

Zhang, L. Y., H. N. Wang, and Z. L. Du (2008). "Prediction of solar active longitudes". In: *A&A* 484.2, pp. 523–527. DOI: 10.1051/0004-6361:200809464. URL: https://doi.org/10.1051/0004-6361:200809464.

Zhang, Liyun, Huaning Wang, Zhanle Du, Yanmei Cui, and Han He (Aug. 2007). "Long-term behavior of active longitudes for solar X-ray flares". In: *Astronomy and Astrophysics* 471, pp. 711–716. DOI: 10.1051/0004-6361:20077311.

Zhang, T., Q. Hao, and P. F. Chen (2024). In: *Statistical Analyses of Solar Prominences and Active Region Features in 304 Å Filtergrams detected via Deep Learning*. URL: https://api.semanticscholar.org/CorpusID:267770259.

Zhang, Xiao-qin, Kuo Yang, and Bao-qing Hao (2010). "Cell-edge detection method based on canny algorithm and mathematical morphology". In: *2010 3rd International Congress on Image and Signal Processing*. Vol. 2, pp. 894–897. DOI: 10.1109/CISP.2010.5646890.

Zhang, Xiaokang and Runping Han (2015). "The Application of Mathematical Morphology and Sobel Operator in Infrared Image Edge Detection". In: *Proceedings of the 2015 International Industrial Informatics and Computer Engineering Conference*. Atlantis Press, pp. 916–921. ISBN: 978-94-62520-54-7. DOI: 10.2991/iiicec-15.2015.205. URL: https://doi.org/10.2991/iiicec-15.2015.205.

Zhao, Cui, GangHua Lin, YuanYong Deng, and Xiao Yang (2016). "Automatic Recognition of Sunspots in HSOS Full-Disk Solar Images". In: *Publications of the Astronomical Society of Australia* 33. ISSN: 1448-6083. DOI: 10.1017/pasa.2016.17. URL: http://dx.doi.org/10.1017/pasa.2016.17.

Zhao, Fang, Junpeng Zhang, and Yulei Ma (2012). "Medical Image Processing Based on Mathematical Morphology". In: *Proceedings of the 2012 International Conference on Computer Application and System Modeling (ICCASM 2012)*.

Zharkov, S., Valentina Zharkova, Stanley Ipson, and Ali Benkhalil (Aug. 2005). "Technique for Automated Recognition of Sunspots on Full-Disk Solar Images". In: *EURASIP J. Adv. Sig. Proc.* 2005, pp. 2573–2584. DOI: 10.1155/ASP.2005.2573.

Zheng, Sheng, Xiangyun Zeng, Ganghua Lin, Cui Zhao, Yongli Feng, Jinping Tao, Daoyuan Zhu, and Li Xiong (2016). "Sunspot drawings handwritten character recognition method based on deep learning". In: *New Astronomy* 45, pp. 54–59. ISSN: 1384-1076. DOI: 10.1016/j.newast.2015.11.001. URL: https://www.sciencedirect.com/science/article/pii/S1384107615001402.

Zimovets, I. V. and V. M. Nakariakov (May 2015). "Excitation of kink oscillations of coronal loops: statistical study". In: *Astronomy & Astrophysics* 577, A4, A4. DOI: 10.1051/0004-6361/201424960.

Zwaard, Rens, Matthias Bergmann, Joe Zender, R. Kariyappa, Gabriel Giono, and Luc Damé (Sept. 2021). "Segmentation of Coronal Features to Understand the Solar EUV and UV Irradiance Variability III. Inclusion and Analysis of Bright Points". In: *Solar Physics* 296. DOI: 10.1007/s11207-021-01863-9.